FABRICATION OF LOW LOSS SILICON WAVEGUIDES BY ION IRRADIATION AND ELECTROCHEMICAL ETCHING

XIONG BOQIAN

(B. SC. Wuhan University)

A THESIS SUBMITTED

FOR THE DEGREE OF DOCTOR OF PHILOSOPHY

DEPARTMENT OF PHYSICS

NATIONAL UNIVERSITY OF SINGAPORE

2014

Declaration

I hereby declare that this thesis is my original work and it has been written by me in its entirety. I have duly acknowledged all the sources of information which have been used in the thesis.

This thesis has also not been submitted for any degree in any university previously.

Xiong Boqian

22 January 2014

Acknowledgement

First and foremost, I would like to express my deepest gratitude to my supervisor Dr. Mark Breese for his support, help and guidance over the past years. Despite his busy schedule as the deputy head of Physics department and then Head of Singapore Synchrotron Light Source, NUS, he always offers me precious and selfless help. Because his patience and encouragement, I have overcome the difficulties in research. Without him, I would never have finished my work and thesis.

I am also indebted to my co-supervisor Dr. Teo Ee Jin, who led me into the fantastic world of silicon photonics with her expertise and great patience. She is the key person who built up the optical detection station where my thesis work was done. We spent almost every day together over three years, and I benefitted a lot from her excellent personality.

I am also grateful to Min, Isaac, Yuanjun, Sudheer, and all the colleagues helped me during my studies.

Life out of lab was also memorable. The friendships I made in Singapore, I will cherish for a lifetime. I want to thank Dr. Li Dongying, Dr. Zhang Xian, Ms. Ke Yan, Dr. Wang Yanyan and so many other friends. We have shared so many wonderful weekends during the past years.

The financial support from Professor Breese's grant is gratefully acknowledged.

Last but not least, I thank my parents for all their support and love throughout my academic endeavors. Their love and support are the motivation that drives me to stick to my goals and not give up. Thanks my little cute cat Man, every time when I work, she lays beside me and accompanies me. Finally, I offer my earnest thanks to my fiancé Wang Rui. Thanks a lot for his love and accompany, I can accomplish this thesis.

Contents

Acknowledgement i

Summary vi

List of Publications viii

List of Figures x

List of Tables xvi

List of Symbols xvii

Chapter 1 Introduction 1

1.1 Motivation 1

1.2 Objective 2

1.3 Thesis outline 2

Chapter 2 Literature Review and Background 4

2.1 Silicon photonics 4

2.2 Porous silicon 9

2.2.1 Fabrication procedures 11

2.2.2 Dissolution mechanisms 12

2.3 Proton beam irradiation 14

2.3.1 Influence of proton beam irradiation 17

2.3.2. Ion irradiation facility at CIBA 19

Chapter 3 Theory of waveguides and propagation loss characterization 26

3.1 Fundamentals of silicon waveguides 26

3.1.1 Wave function 26

3.1.2 The planar waveguide 30

3.2 Propagation loss characterization 34

3.2.1 Experimental techniques for optical characterization 34

3.2.2 Propagation loss and method for optical characterization 39

Chapter 4 Fabrication for Silicon on oxidized-porous-silicon waveguides and sample preparation 44

4.1 PBW fabrication for silicon on oxidized-porous –silicon waveguides.......... 45

4.2 Large area irradiation for silicon on oxidized-porous –silicon waveguides .. 47

4.3. Anodization setup and characterization 50

4.3.1 Anodization setup 50

4.3.2 Porous silicon formation rate 52

4.3.3 Refractive index of porous silicon 54

4.4 Oxidation... 55

4.5 Sample preparation 56

Chapter 5 Silicon on oxidized-porous-silicon: linear waveguides 60

5.1 A line focus of a quadrupole multiplet for irradiating millimeter length waveguides.. 60

5.2 Strip silicon-on-oxidized porous silicon waveguides 65

5.2.1 Propagation loss for strip waveguides by direct proton beam irradiation 65

5.2.2 Low loss strip waveguides by large area irradiation.......................... 70

5.2.3 Strip waveguide with various dimensions 76

5.2.4 Strip straight waveguide fabricated with varied proton fluence 85

5.3 Summary 89

Chapter 6 Silicon on oxidized-porous-silicon: three-dimensional and curved waveguides 91

6.1 Three dimensional integration of waveguides in bulk silicon 91

6.1.1 The first test for a fluence of protons.. 93

6.1.2 Two layers of waveguide in a single silicon chip 94

6.2 Waveguide bends 97

6.2.1 C-bend waveguides 99

6.2.2 90 degree bending waveguides 104

5.3 Summary 110

Chapter 7 Bragg cladding waveguides 112

7.1 Background of Bragg reflectors 112

7.3 Fabrication of Bragg waveguides 116

7.3 Characterization of Bragg waveguides 118

7.4 Summary 124

Chapter 8 Conclusion 126

8.1 Summary of Results 126

8.2 Recommendations for further work 130

Bibliography 131

Summary

The aim of this thesis is to report novel methods that have been developed to fabricate different kinds of low loss silicon, or porous silicon-based waveguides, including straight waveguides, curved waveguides, three-dimensional integration of silicon on oxidized porous-silicon (SOPS) waveguides and all-silicon single-mode Bragg cladding rib waveguides. The two major process steps used for fabrication of such structures are ion irradiation and electrical anodization.

High-energy ion beam irradiation with MeV protons or helium ions creates localized defects and increases the resistivity of a *p*-type silicon substrate in both the lateral and vertical directions. In this thesis, ion irradiation is employed using two different methods. One method is Proton Beam Writing (PBW) which is carried out using direct, focused ion beam irradiation. The other method employs a uniform, large ion beam to irradiate silicon wafers which are coated with pre-patterned photo-resist masks. Using this technique; we have developed and explored silicon micromachining for fabricating different kinds of silicon waveguides with a straightforward and efficient control. Subsequent electrochemical anodization in hydrofluoric acid solution is used to form various porous silicon structures after ion irradiation. Further oxidation is required for SOPS waveguides to improve their performance by reducing their propagation loss. Another silicon waveguide known as Bragg cladding rib

waveguide was also fabricated using proton beam irradiation. Avoiding the traditional multiple deposition process steps, we propose a monolithic integration of Bragg waveguides in silicon. For each kind of waveguide, optical characterization and further studies of the loss mechanisms are presented and discussed.

List of Publications

[1] **Xiong, Boqian.** ; Breese, M.B.H.; Azimi, S.; Ow, Y.S.; Teo, E.J.," Use of a line focus of a quadrupole multiplet for irradiating millimeter length lines", **Source:***Nuclear Instruments and Methods in Physics Research, Section B: Beam Interactions with Materials and Atoms*, v 269, n 8, p 729-732, April 15, 2011

[2] Teo, E.J. ; **Xiong, B.Q**.; Ow, Y.S.; Breese, M.B.H.; Bettiol, A.A.," Effects of oxide formation around core circumference of silicon-on-oxidized-porous-silicon strip waveguides", Source: *Optics Letters*, v 34, n 20, p 3142-3144, October 15, 2009

[3] Teo, E.J. ; **Xiong, B.Q**.;" Three dimensional integration of waveguides in bulk silicon", Source: *Microelectronic Engineering*, v 102, p 29-32, Feb. 2013

[4] Teo, E.J. ; **Xiong, B.Q**.; Breese, M.B.H.; Bettiol, A.A.;" A silicon-based technology for the fabrication of smooth optical devices", Source: *2010 Photonics Global Conference (PGC 2010)*, p 4 pp., 2010

[5] Ee Jin Teo ; Bettiol, A.A.; **Boqian Xiong**; Breese, M.B.H.; Shuvan, P.T. "An all-silicon, single-mode Bragg cladding rib waveguide", Source: *Optics Express*, v 18, n 9, p 8816-23, 2010

[6] Teo, E.J. ; Yang, P.; **Xiong, B.Q.**; Breese, M.B.H.; Mashanovich, G.Z.; Ow, Y.S.; Reed, G.T.; Bettiol, A.A.; "Novel types of silicon waveguides fabricated using proton beam irradiation", Source:*Proceedings of the SPIE - The International Society for Optical Engineering*, v 7606, p 76060M (7 pp.), 2010

[7] Teo, E.J. ; Bettiol, A.A.; Yang, P.; Breese, M.B.H.; **Xiong, B.Q**.; Mashanovich, G.Z.; Headley, W.R.; Reed, G.T.; "Fabrication of low-loss silicon-on-oxidized-porous-silicon strip waveguide using focused proton-beam irradiation", Source:*Optics Letters*, v 34, n 5, p 659-61, 1 March 2009

[8] Teo, E.J. ; Bettiol, A.A.; Yang, P.; Breese, M.B.H.; **Xiong, B.Q.**; Mashanovich, G.Z.; Headley, W.R.; Reed, G.T.; "Fabrication of low-loss

silicon-on-oxidized-porous-silicon strip waveguide using focused proton-beam irradiation", Source:*Optics Letters*, v 34, n 5, p 659-61, 1 March 2009

[9] Bettiol, A.A.; Ee Jin Teo; Prashant, S.; **Xiong Boqian**; Breese, M.B.H.; "Fabrication of porous silicon channel waveguides with multilayer Bragg cladding", Source: *Proceedings of the SPIE - The International Society for Optical Engineering*, v 7606, p 76060K (6 pp.), 2010

[10] Mashanovich, Goran Z. ; Milosevic, Milan M.; Nedeljkovic, Milos; Owens, Nathan; Headley, William R.; Teo, Ee Jin; **Xiong, Boqian**; Yang, Pengyuan; Hu, Youfang; "MID-infrared silicon photonic devices", Source: *Proceedings of SPIE - The International Society for Optical Engineering*, v 7943, 2011, *Silicon Photonics VI*

[11] Mashanovich, Goran Z. ; Miloševic, Milan M.; Nedeljkovic, Milos; Owens, Nathan; **Xiong, Boqian**; Teo, Ee Jin; Hu, Youfang; "Low loss silicon waveguides for the mid-infrared", Source: Optics Express, v 19, n 8, p 7112-7119, April 11, 2011

List of Figures

Figure 2.1. Propagation loss as a function of the buried oxide thickness of 7.4 µm planar silicon waveguide. From [10] 6

Figure 2.2. Schematic of cross-section of a single mode rib waveguide. 9

Figure 2.3. (a) Schematic of *p*-type electrochemical anodization setup (b) schematic of *n*-type electrochemical anodization setup. 12

Figure 2.4. Chemical processes for silicon dissolution. From [31] 13

Figure 2.5. Comparison between (a) PBW, (b) FIB, and (c) electron beam writing. This figure shows schematically the difference between these three techniques. The p-beam trajectories were simulated using SRIM[41] while the e-beam trajectories simulated by CASINO[40] software. The advantage of PBW is its ability to penetrate deeper with minimal lateral broadening.[32] 17

Figure 2.6. Damage profile created by 250 keV protons, showing the low and high defect regions. 18

Figure 2.7. (a)-(c) Electric field distributions with increasing ion fluence simulated by MEDICI. (d)-(f) schematically show the silicon core size increases at higher fluences. 19

Figure 2.8. (Left) Top down schematic diagram of the micro beam setup in CIBA. (Right) Image of the CIBA micro beam facilities. (1): the accelerator, (2) 90 degree magnet, (3) switching magnet, (4) endstations 20

Figure 2.9. Cross sectional schematic of a quadrupole lens. Positively charged ions are travelling out of the page. Green arrows indicates the direction of current flow in the coils to lead in the desired magnetic polarity at the ends. 22

Figure 2.10. Schematic for large area irradiation. 23

Figure 2.11. (a) large area irradiation facility. (b) The ladder and sample holder used to mount and lower samples into the ion beam path (c) Fluorescent screen placed at the end of the extension pipe (d) Nuclear microprobe chamber for direct proton beam irradiation 24

Figure 3.1. The definition of the TE light for a slab waveguide................................28

Figure 3.2. The demonstration of Snell's Law for a light ray passing from a material of higher refractive index to a lower one..30

Figure.3.3. TEM wave propagates in a planar waveguide...32

Figure 3.4. (a) Photograph for the setup (b) Schematic of the experimental set up used for optical characterization. 37

Figure.3.5. Typical results from the cut-back method...41

Figure 3.6. (a) Image for scattered light taken from an InGaAs camera of a silicon waveguide fabricated by large area irradiation. (b) Intensity of the scattered light. The slope of the fit is the propagation loss. 42

Figure 4.1. Schematic for (a) 3 different proton fluences (1×10^{15}, 1×10^{14}, 7×10^{13} ions/cm^2) irradiating a silicon substrate; (b) first anodization (c) removal of the porous silicon by KOH (d) second anodization...45

Figure 4.2. Schematic for mask printing..48

Figure 4.3 Schematics of the fabrication process showing (a) proton beam irradiation, (b) PS formation till the end of range of the ions and (c) PS removal (d) a second etching step to undercut the irradiated structures. 49

Figure 4.4. Photos showing the preparation of a silicon sample prior to anodization. (a) back of a silicon sample. (b) Gallium-Indium eutectic painted on the back surface for an Ohmic contact with a wire. (c) Epoxy covering the back surface to protect the wire from HF. (d) Side view of the prepared sample...50

Figure 4.5. PSi formation rates versus the anodization current densities. Trial 1 (black): 10 mA/cm^2, 30mA/cm2, 50mA/cm^2, 70mA/cm^2 and 83 mA/cm^2. Trial 2 (red): 10 mA/cm^2, 30mA/cm^2, 50mA/cm^2, 70mA/cm^2 and 83 mA/cm^2. Trial 3 (green): 30mA/cm^2 , 60mA/cm2, 90mA/cm^2.All layers were etched for 30 seconds. In (b) a linear is fitted by averaging three trials. From [57] 53

Figure 4.6. Refractive indices arising from different etch current densities plotted against wavelengths[57]..54

Figure.4.7. sidewall roughness of testing waveguide fabricated by PBW (a) before oxidation, roughness is 7.1 nm (b) after oxidation of 3 hours in 1100°, roughness is 3.0 nm. 55

Figure 4.8. (a) Photograph of the polishing facility. (b) The pressure arm pushes down on the sample holder (c) The sample mounted on one side. 57

Figure. 5 1. PRAM simulations of a single trajectory of a 250 keV proton from the object aperture of the microprobe, passing through a quadrupole triplet with increasing excitation from (1) to (4). The beam remains almost focused in the vertical plane while becoming an ever-longer line in the horizontal plane. The excitations of the lenses are as follows: (1) Point focus with L1, L2 = ±0.17554, L3 = +0.16207 which remains constant. (2) L1, L2 = ±0.3. (3) L1, L2 = ±0.4. (4) L1, L2 = ±0.5......61

Figure 5.2. AFM line profiles across a long focused line which was irradiated in a silicon wafer. Aberrations in the line focus are manifested as an asymmetry in the final irradiated structure. These occur owing to difficulties in focusing to a line, resulting in the beam slightly (a) over- or (b) under-focused. 62

Figure 5.3. Array of lines produced with the beam focused to a long line and used to sequentially irradiate lines in a silicon wafer. (a) optical micrograph (b) AFM image (c) cross-section SEM. 63

Figure 5.4. Low magnification optical micrograph of an array of 8 mm long lines produced in a silicon wafer. 64

Figure 5.5. Long line produced in PMMA polymer resist, with a width of 1.5 µm. (a) optical micrograph, (b) AFM image. 64

Figure 5.6. SEM of the waveguides irradiated with fluences of (a) 7×10^{13}, (b) 1×10^{14}, and (c) 1×10^{15}/cm^2. 66

Figure 5.7. r.m.s. roughness (σ) and autocorrelation length *Lc* of the three waveguides as a function of height. 67

Figure 5.8. Propagation losses for 7×10^{13}/cm2 (□, ■), 1×10^{14}/cm^2 (△, ▲), and 1×10^{15}/cm^2 (○, ●) after oxidation. The empty shapes represent the TE polarization, and the filled shapes represent TM polarization. The straight line shows a linear fit of the output power (dB) as a function of length. 69

Figure 5.9. SEM image of the (a) top and (b) cross-sectional view of the waveguides. A close up of a waveguide (c) before and (d) after oxidation. The insets show the output modes imaged from the end facets of each respective waveguide. 70

Figure 5.10. Cutback measurements of a waveguide before and after oxidation. The loss curves are determined from fitting based on slopes. 71

Figure 5.11. (a) SEM image of the underside of the waveguide. (b) AFM image across the bottom and sidewalls of the waveguides. Calculated scattering loss due to (c) both the bottom and the sidewalls and (d) solely due to the sidewall roughness. The measured losses for waveguides (■) before and (●) after oxidation are overlaid on both plots...74

Figure 5.12. SEM images of a waveguide with a design width of 5 μm (a) taken 3 hours in 1100°oxidation (b) taken 9 hours in 1100°oxidation. The oxidation layer is enlarged with longer oxidation time. 77

Figure 5.13.The mechanism of the Effective Index Method 80

Figure 5.14. Function f with respect to N_{eff} within the range of 3 to 3.5. N_{eff} should be closed to n_1(3.5). The blue line and the black line are within the fixed value of 2πLc/λ. From the AFM results, the maximum and minimum values of Lc is 193 and 139, hence the range of 2πLc/λis from 0.56 to 0.77 with λ = 1550nm...............................82

Figure 5.15. the propagation loss is plotted versus actual width measured by SEM..84

Figure 5.16 Propagation loss versus surface roughness. Propagation losses for design width of 3 μm (black symbols), design width of 4 μm (red symbols), and design width of 5 μm (blue symbols). The ▲ presents the TE polarization and ■ presents the TM polarization. 86

Figure 5.17. Power lines utilized for fitting the scatter charts. The function used is $y=a+b\cdot x^c$. (a) for design width of 3 μm (b) for design width of 4 μm (c) for design width of 5 μm...89

Figure 6.1. (a and b) Shows cross sectional view of a silicon core irradiated with (a) $1 \times 10^{15}/cm^2$ and (b) $5 \times 10^{13}/cm^2$. (c) Close-up of a single core before oxidation (d) and after oxidation. 93

Figure 6.2. 2-level system formed by single energy irradiation through a mask (d). Corresponding output image by simultaneously coupling light into all the waveguides. 95

Figure 6.3. 3-Level system formed by double energy irradiation through a mask (d). Shows the corresponding output image by simultaneously coupling light into all the waveguides......96

Figure 6.4 Cross-sectional image of a modeled waveguide bend demonstrating the polarization dependence on slab leakage due to the bend radius (R=50□ μm). The (a) TM mode demonstrates little slab leakage whilst the (b) TE mode demonstrates a large amount of leakage. From [82]......97

Figure 6.5 Simulation is done by Beam Prop^{TM} for waveguide with the TE polarization (a) and the TM polarization (b) in a waveguide bend (R=50 μm). Waveguides have the same cross-sectional dimensions as 4.5 μm width and 2 μm height......97

Figure 6.6. Modeled Loss of a 90° waveguide bend as a function of bend radius (modeled by A. Liu of the Intel Corporation). From [82]......98

Figure 6.7. Schematic for modeled cut-back method for measuring the bend loss for C-bend waveguides......100

Figure 6.8. Top view of varied C-bend waveguide by SEM......102

Figure 6.9. Scattered image of a C-bend waveguide with radius of 60 um. The white arrows indicate the C-bends......103

Figure 6.10. Bend loss versus radius of bend......103

Figure 6.11 The CAD layout for designing the 90 degree bends. The same radius bending waveguides are organized in one block. After fabrication process, one block is produced in one silicon sample......105

Figure 6.12. (a) Low magnification optical micrograph of an array of 45 μm-radius 90 degree bends (b) High magnification optical micrograph for 45 μm-radius 90 degree bends (c) Scattered light of 45 μm-radius 90 degree bends taken by the infrared camera......106

Figure 6.13. The measured bend loss. The slop of the linear lines is the loss per bend, which are 1.35dB/bend and 1.36 dB/bend for the TE and TM polarizations......107

Figure 6.14. Bend loss versus radius of 90°bends......109

Figure 6.15. simulation for the bend loss versus radius. The function used was $\alpha = K \cdot \exp(-cR) + a$ [84]. 110

Figure 7.1. Schematic diagram of the fabrication process 116

Figure 7.2. Surface plots of the simulated reflectance of the Bragg reflectors as a function of wavelength and angles, in the TE and TM polarizations. 117

Figure 7.3. (a) and (b) shows the resultant cross sectional SEM image of Bragg cladding waveguide irradiated with a fluence of 2×10^{15}/cm2 and $4 \times 10^{15}/cm^2$. 118

Figure 7.4. close-up SEM images of the top and bottom claddings of the waveguide sidewalls for a fluence of $2 \times 10^{15}/cm^2$ and $4 \times 10^{15}/cm^2$ respectively 119

Figure 7.5. (a) Plot of 1/*e* electric field width as a function of width in TE and TM polarizations. (b) Theoretical single-mode boundary as the width and height of the core is varied. 122

Figure .7.6. (a) and (b) simulated structure and their corresponding fundamental TE and TM modes for 2×10^{15} and $4 \times 10^{15}/cm^2$. 123

Figure 7.7. shows the scattered light intensity as a function of length for (a) $2 \times 10^{15}/cm^2$ and (b) $4 \times 10^{15/}cm^2$ determined from the scattered light images in the inset. 124

List of Tables

Table 2.1. Effect of anodization parameters on PSi formation. From [29] 11

Table 2.2. Classification of porous materials..14

Table 2.3. End of range depth simulated from SRIM for different energies of helium and protons in bulk silicon respectively...16

Table 5.1. Waveguide dimensions, σ, and *Lc* for each waveguide fluence after oxidation 66

Table 5.2. Effect of oxidation on the bottom and sidewalls of the waveguides. 71

Table 5.3. Summary of propagation losses with varied dimensions...........................76

Table 5.4. Waveguide surface roughness, and L_c measured by AFM.......................84

Table 5.5. Sidewall and bottom roughness for different proton fluences. The average roughness is calculated as root mean square of the sidewall and bottom roughness...85

Table 5.6. Summary of propagation loss and dimensions for waveguides fabricated by 3 different fluences 86

List of Symbols

AFM Atomic Force Microscope

BESOI Bond and Etch-back SOI

BOX Buried Oxide

BPM Beam Profile Monitoring

CAD Computer Aided Design

CIBA Center for Ion Beam Applications

CMOS Complementary Metal Oxide Semiconductor

DLF Diamond Lapping Film

FC/PC Ferrule Connector/Physical Contact

FIB Focused Ion Beam

FIPOS Full Isolation by Oxidized Porous Silicon

FWHM Full Width at Half Maximum

Ga-In Gallium-indium

GPIB General Purpose Interface Bus

HF Hydrofluoric Acid

HMDS Hexamethyldisilazane

IMRE Institute of Materials Research and Engineering

KOH Potassium hydroxide

NA Numerical Aperture

PBW Proton Beam Writing

PMMA polymethylmethacrylate

PR photo-resists

PSi Porous Silicon

SEM Scanning Electron Microscope

Si Silicon

SIMOX Separation by IMplanted Oxygen

SiO_2 Silicon Dioxide

SOI Silicon-On-Insulator

SOPS Silicon-on-Oxidized-Porous-Silicon

TE Transverse Electric

TEM Transverse Electromagnetic

TIR Total Internal Reflection

TM Transverse Magnetic

UV Ultra Violet

Chapter 1

Introduction

1.1 Motivation

Recently, integrated circuits based on silicon photonics have been developed and improved, primarily because of the growing demand for faster interconnection with higher data bandwidth. It is widely accepted that silicon is the best candidate amongst different materials for optoelectronics and photonic integrated circuits due to its high transparency at the technologically important wavelengths of 1.3 and 1.55 μm. Moreover, existing infrastructure in the microelectronics industry allows for integration of photonics and electronics onto a single silicon chip.

Conventional silicon waveguide fabrication involves UV or e-beam patterning followed by etching on a silicon-on-insulator (SOI) substrate. These techniques often require many complicated steps which are time consuming and an expensive SOI substrate is needed. The main motivation of our work is to investigate different schemes to fabricate different kinds of low loss silicon waveguides and c-bend waveguides using ion irradiation and porous silicon formation.

1.2 Objective

In this thesis, the main objective is to develop a new process to fabricate low loss silicon-on-oxidized porous silicon waveguides via masked proton irradiation and porous silicon formation. This approach enables us to control the shape of waveguides in a simple and cost effective way which is compatible with mass production. We also aim to fabricate Bragg waveguides using ion irradiation and multilayers of porous silicon without the need for multiple depositions of alternating materials.

1.3 Thesis outline

This thesis contains three main parts. Chapter 1 and 2 form the first part of this thesis. Chapter 1 describes the motivation and objectives of this thesis. Chapter 2 introduces porous silicon as a material as well as the formation of porous silicon. It also describes the principles and theory of silicon photonics, especially silicon waveguides. Chapter 3 firstly introduces and discusses the theory used to design strip waveguides and bending waveguides and the method of optical characterization. Chapter 4 focuses on the procedure of fabrication of silicon-on-oxidized porous silicon waveguides. Fabrication of silicon-on-oxidized porous silicon waveguides using our ion irradiation and anodization process was carried out. In addition, oxidation steps were used to reduce their roughness. The preparation steps for waveguide samples before characterization are introduced.

The results of the measurements made by the author are demonstrated in Chapters 5 and 6. The propagation loss and the relationship between loss, waveguide dimensions and roughness for strip waveguides were studied in Chapter 5. The bending loss for different bending radii of waveguides was investigated in Chapter 6. Another type of silicon waveguide, called an all-silicon single-mode Bragg cladding rib waveguide, is presented in chapter 7. The principle, fabrication and characterization of such waveguides are discussed in detail. The conclusions drawn from the results are discussed in chapter 8. The work of this thesis is concluded by offering some insight into future work.

Chapter 2

Literature Review and Background

This chapter covers the background for the work undertaken in this thesis. The waveguides that we fabricate in this work are all in silicon materials. Hence, the chapter starts with a review of some of the key accomplishments in silicon photonics. It provides relevant background information to understand the experimental work presented in this thesis, including the formation of porous silicon and proton beam irradiation.

2.1 Silicon photonics

The first investigation of silicon as a photonic material was reported by Soref and Petermann in the late 1980s and early 1990s [1-3]. With his pioneering research, Soref made use of the optical properties of silicon which becomes transparent at optical telecommunications wavelengths from 1.3 to 1.6 μm. This range is technologically importance because fiber optic lasers mainly use these infrared wavelengths for communication. Silicon photonics witnessed a rapid development in the late 1990s. Integrated optics in silicon has been receiving a lot of interest for a combination of technological and cost reasons. Strong optical confinement can be achieved, utilizing the high contrast of refractive index between that of silicon and SiO_2, thus achieving a

very compact structure. In addition, silicon is an ideal material with properties including high thermal conductivity (~10 times higher than GaAs), high optical damage threshold (~10 times higher than GaAs), and high third-order optical nonlinearities.

One of the most important and fundamental devices in silicon photonics is the waveguide, which allows the routing of confined light from one part of a chip to other parts. Early work on silicon waveguides focused on planar waveguides in which the light is confined only in the vertical direction. The first single-crystal silicon planar waveguide was demonstrated by Soref *et. al.* [1]. Channel waveguides and planar waveguides at λ = 1.3 μm (with end-fire coupling) have been demonstrated in single-crystal silicon layers grown epitaxially on heavily-doped Si substrates. As a “first effort”, the propagation losses were quite high, ranging from 5 to13 dB/cm in slab waveguides and from 15 to20 dB/cm in rib waveguides. In the late 1980’s and early 1990’s, two methods, including Separation by IMplantated OXygen (SIMOX) and Bond and Etch-back SOI (BESOI), were widely adopted to fabricate waveguides on SOI wafers [4]. The SIMOX method, which was most popular method for the fabrication of SOI wafers, uses a high fluence of oxygen ions which are implanted into a silicon wafer to form a buried silicon dioxide layer. After implantation, the silicon wafer is annealed at 1300 ºC to create silicon dioxide [5]. The BESOI method comprises 3 main steps: (1) creating a top layer of silicon dioxide on two silicon wafers; (2) bonding these two oxide layers into a single layer by heating; and (3)

etching on the unified wafer until the desired thickness is obtained [5].

In 1988, Kurdi *et. al.* theoretically studied the propagation loss of the SOI waveguide and calculated a loss of 1 dB/cm for a planar waveguide of 0.2 μm thickness with a 0.5 μm buried oxide layer [6]. In 1989, the first waveguide on SOI materials was fabricated by Cortesi *et. al.* [7]. Also, in 1989, Davies *et. al.* measured a loss of 4 dB/cm for optical waveguides fabricated in a SIMOX wafer [8]. Afterwards, further efforts were made to reduce the high propagation loss. In 1991, Schmidtchen *et. al.* [9] reported a loss of 0.4 dB/cm with rib heights of 7.4 μm, etch depths of 2.2 μm and a waveguide width greater than 3 μm, and with free-space wavelengths of λ=1.3 μm and 1.55 μm using horizontally polarized light (where the electric field of the light is aligned parallel to the buried oxide layer).

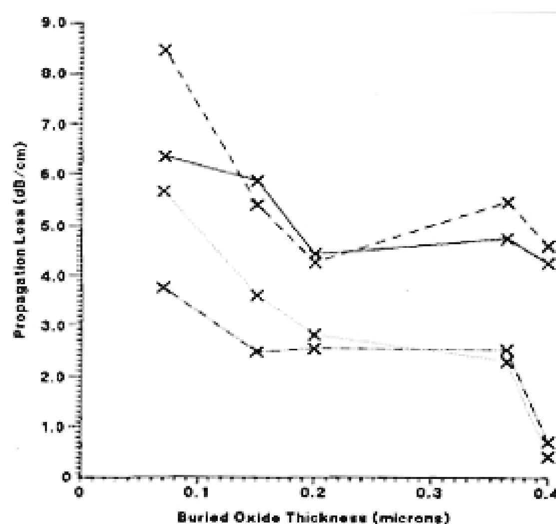

Figure 2.1. Propagation loss as a function of the buried oxide thickness of 7.4 μm planar silicon waveguide. From [10]

From theoretical analysis by Kurdi *et. al.* [6], the thickness of the oxide layer affects the propagation loss of a SOI waveguide. If the oxide layer is too thin, the optical field can couple to the substrate, thereby increasing the propagation loss of the

waveguide. In another work using SIMOX technology, Rickman *et. al.* fabricated planar waveguides with 6 μm thickness and various buried oxide thicknesses [10]. The relationship between the propagation loss and the buried oxide thickness is shown in Figure 2.1. The lowest loss of 0.14±0.5 dB/cm can be observed for an oxide thickness of 0.4 μm. This particular result strongly demonstrated the applicability of SIMOX-based waveguides for practical device applications.

By 1994, the propagation loss of SOI waveguides was further reduced to a level indistinguishable from pure silicon, as reported by Rickman *et. al*. [11] for 1.5 μm wavelength TE polarized light. This measurement demonstrated that silicon was not only a viable guiding material, but also that it was possible to alleviate the propagation loss. The loss in the waveguides was greatly influenced by the interface roughness, possibly arising from the SIMOX process and/or the reactive ion etching step. For a rib waveguide with a height of 4.3 μm, a width of 3.7 μm, and an etch depth of 1.7μm, a loss value of 0.0±0.5 dB/cm for horizontally polarized light and 0.4±0.5dB/cm for vertically polarized light at λ=1.532 μm were achieved. These results implied that the waveguides had almost no propagation loss within the stated uncertainty of the measurement. These are to date the best recorded propagation losses for a rib waveguide in SIMOX.

From late 1980s to 1990s, however; it was noteworthy that these low loss waveguides had large sizes of the order of several microns in cross-sectional dimensions [10, 11]. Due to insufficient optical confinement and surface roughness, the propagation loss of

small waveguides was quite high. Weiss *et. al*. reported the loss as high as 8 dB/cm for 2 μm-thick planar silicon waveguides in 1991 [12]. Current research actively targets the miniaturization of micro- and nanophotonic circuits. The coupling of light to these small waveguides remains an issue today, especially for very small, sub-micron, waveguides.

On the other hand, theoretical modeling was also carried out in parallel with experimental work. Single mode waveguides are important to many practical devices. The concept of the rib waveguide was developed to achieve single mode propagation as it is unnecessary to shrink the size of rib waveguides to the order of several hundred nanometers. One of the earliest studies to determine the dimensions of a rib waveguide was done by Petermann *et. al* [13] in the late seventies. This work was improved by Soref *et. al*. [3] using mode matching and beam propagation method. They found the following condition:

$$\frac{a}{b} \leq \alpha + \frac{r}{\sqrt{1-r^2}} \qquad (2.1.1)$$

$$0.5 \leq r < 1.0, \alpha = 0.3$$

where α is a constant determined by the modeling, *a* and *b* are the waveguide cross-sectional dimensions, and *r* is the slab height scaling factor, all of which are defined in Figure 2.2. The variables n_0, n_1, n_2 are the indices of refraction for air, silicon, and silicon dioxide, respectively, and λ is the free-space wavelength of light.

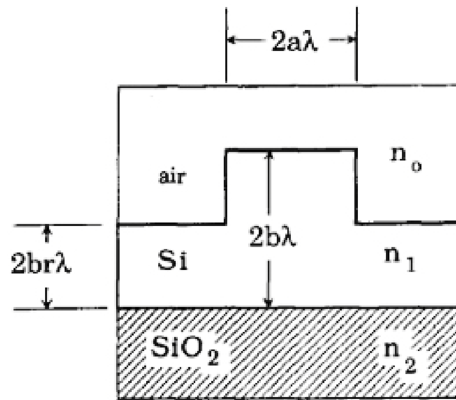

Figure 2.2. Schematic of cross-section of a single mode rib waveguide.

For high speed communication, large bandwidths of 40 Gbps have already been achieved by Intel in 2004.[14]

2.2 Porous silicon

Porous silicon (PSi) was discovered by accident in 1956 by Arthur Uhlir Jr. and Ingeborg Uhlir at the Bell Labs in U.S. when they were in the process of electropolishing silicon with an electrolyte containing hydrofluoric acid (HF), at low applied bias on a thick black, red or brown layer, which contained nanoporous holes formed on the surface of the silicon sample. At the time, the finding did not attract attention from other researchers and was merely mentioned in Bell Lab's technical notes [15].

In the late 1980s, Leigh Canham at the Defense Research Agency in England reasoned that the diaphanous silicon filaments generated when the pores become large and numerous enough to overlap might display quantum confinement effects [16]. Oxidized porous silicon was also utilized to create insulating layers for

Silicon-on-Insulator technology [17]. Silicon on oxidized-porous silicon (SOPS) has the same properties as the conventional SOI but with a reduced number of fabrication steps.

Since Canham's report in 1990 that porous silicon with high porosity can emit visible photoluminescence at room temperature, it became a popular material to study for silicon photonics [18]. The author further explained the mechanism by proposing a quantum model for photoemission of PSi [19, 20]. In this model, highly porous silicon can be considered as one-dimensional or zero-dimensional system where the excitons are confined. According to the simple particle-in-a-box example, the excitonic transition energy is larger than the Si energy gap. Around the same time, electroluminescence of PSi was reported [21]. These discoveries promoted PSi as an interesting material for commercial photonic devices.

The potential application areas of PSi are much wider than light emission. Its applications has extended in many areas such as photonics [22], field emitters, and silicon micromachining via sacrificial PSi [23, 24]. PSi is also a promising material for biotechnology [25-27]. The refractive index of PSi can be controlled quite well by varying the current during the etching. Thus PSi can act either as a cladding or core material in a waveguide [28]. The work in this thesis revolves around machining PSi structures for various applications as well as using PSi as a sacrificial material for machining silicon waveguide structures. However, the boundaries between the silicon core and porous silicon are rough because of the porosity of porous silicon.

2.2.1 Fabrication procedures

PSi is fabricated by electrochemical anodization of bulk silicon wafers in hydrofluoric acid (HF). The HF is usually diluted with ethanol and deionized and distilled water. Ethanol is added to enhance the wettability of the silicon surface and it also helps the evacuation of H_2 bubbles during this process.

A typical anodization setup for *p*-type Si wafers is shown in Figure 2.3. Platinum and Teflon are usually used because of their chemical resistance to HF. When an electrical bias is applied, an electric field causes electrical holes to travel to the surface of the silicon sample, generating the pores. For *n*-type Si, in order to achieve a significant electrical hole current, external illumination of the sample is required (Fig 2.3(b)). In this thesis, the various experiments presented use only *p*-type silicon samples. The critical parameters of the anodization procedure are shown in Table 2.1 [29]. Modulation of the anodization can be most easily achieved by varying the applied current density. For example, PSi multilayers can be fabricated simply by periodically changing the current density with time.

An increase of	Porosity	etching rate	Electropolishing threshold
HF concentration	decrease	decrease	increase
Current density	increase	increase	N.A.
Anodization time	increase	almost constant	N.A.
Temperature	N.A.	N.A.	increase

Table 2.1. Effect of anodization parameters on PSi formation. From [29]

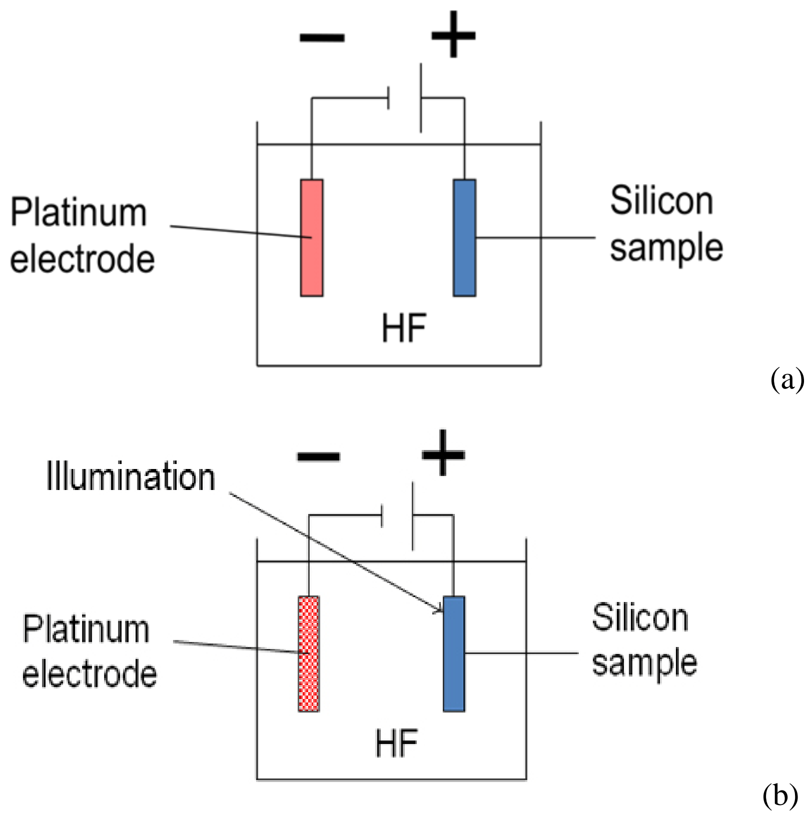

Figure 2.3. (a) Schematic of *p*-type electrochemical anodization setup (b) schematic of *n*-type electrochemical anodization setup.

2.2.2 Dissolution mechanisms

In 1991, Lehmann *et. al.* proposed a dissolution mechanism of porous silicon, which is commonly accepted [30]. The reaction schematic is shown in Fig. 2.4. When a bias is applied to the electrolyte solution, an electrical hole travels from the bulk and approaches the silicon-electrolyte interface. Correspondingly, a nucleophilic attack on Si-H bonds occurs by fluoride ions and a Si-F bond forms. Due to the polarizing influence of the first Si-F bond, another F^- ion can attack and bond subsequently until 4 Si-F bonds form. Gaseous SiF_4 is the product of the reaction, which is released in

the HF solution. The remaining silicon surface atoms are again hydrogenated. A total chemical reaction could describe the anodization:

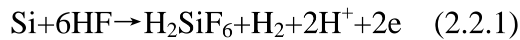

$$Si+6HF \rightarrow H_2SiF_6+H_2+2H^{+}+2e \quad (2.2.1)$$

The last term - a negative charge at the interface, is neutralized by the current flow, which explains the requirement of hole injection from the substrate towards the silicon/HF solution. A silicon/HF solution depletion zone is generated at the Si/HF solution interface. The schematic of the dissolution mechanism is indicated in Fig 2.4.

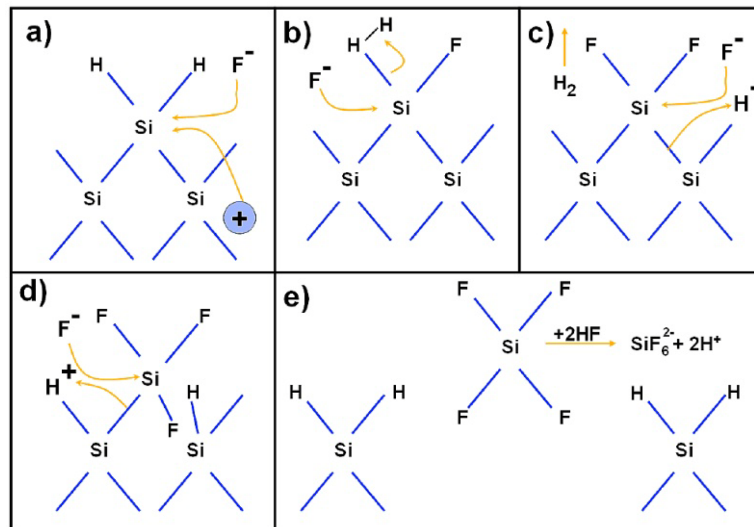

Figure 2.4. Chemical processes for silicon dissolution. From [31]

Pore formation is proposed to be the result of the development of a passivation of PSi. The potential barrier is generated in the space charge region. The width of the depletion zone depends on the doping and may explain the different pore sizes found in differently doped silicon wafers. In addition, the depletion layer width depends on the surface curvature: anodization preferentially occurs at the pore tips where the curvature is smallest. Moreover, when the depletion zones of adjacent pores meet each other, the current flow is suddenly pinched off. Further Si etching is blocked, and

pore collapse is prevented. For this reason, the reaction is self-limited and leads to a porous structure rather than electropolishing.

The average pore size of PSi structures covers four orders of magnitude from nanometer to tens of micrometers. According to the pore diameters (d), PSi can be divided into three classes: microporous (d < 2 nm), mesoporous (2 nm < d < 50 nm), and macroporous (d > 50 nm). The resistivity of silicon wafers affects the type of pores formed; low resistivity silicon wafers (< 0.1 Ω.cm) form mesopores, moderate resistivity wafers (0.1-50 Ω.cm) form micropores, while high resistivity wafers (>50 Ω.cm) form macropores (table 2.2).

pore width (nm)	Type of material	resistivity of silicon waver (Ω.cm)
≤2	microporous	0.1-50
2-50	mesoporous	< 0.1
> 50	macroporous	> 50

Table 2.2. Classification of porous materials

2.3 Proton beam irradiation

Proton beam writing (PBW) is a direct-writing process which has been developed and improved at Centre of Ion Beam Application (CIBA). This process is similar to direct writing using electrons. However, the proton beam writing process has some interesting and unique advantages; ions are more massive and so penetrate deeper with a straight trajectory [32-39]. Therefore, proton beam writing has been utilized for fabricating three-dimensional, high aspect ratio structures with vertical and smooth sidewalls, and with low line-edge roughness. Electron trajectories can be simulated

using Monte Carlo techniques such as Casino [40] and PBW also can be simulated with the same method.

The interaction of protons and resist materials can be summarized as follows:

The proton beam penetrates mostly in a straight trajectory with only a small amount of lateral broadening where nuclear collisions occur. This is a considerable advantage compared with the electron beam writing or ultraviolet (UV) lithography, especially for fabricating high aspect ratio and three-dimensional structures. This is because, unlike a proton beam, a focused electron beam scatters rapidly once it enters the resist material (Fig 2.5).

The effect of exposure including energy deposition and defect creation along the path of protons is relatively constant except at the end of range (where an approximately ten-fold increase in defect creation occurs). This offers another advantage over UV lithography or X-ray lithography which has an exponential reduction in energy deposition with depth.

The penetration depth and the end of range of proton beams in different materials are determined by the proton beam energy. The end of range of protons and the profile of the penetration path in different materials can be simulated by Monte Carlo calculations using software such Stopping and Range of Ions in Matter (SRIM) [41]. Hence, this allows exact control of the penetration depth and makes the fabrication of multilevel structures possible. This property is used to machine vertically stacked silicon waveguides in Chapter 5.3.

As a new technology with great potential, proton beam writing has been well studied and understood. The primary application of PBW is fabricating structures in photo-resists where protons cause bond breaking or scissioning for positive resists, or cross-linking in negative resists. SU-8 is used as a negative resist and polymethylmethacrylate (PMMA) can be used both as a positive resist at low fluence and as a negative resist at high fluence. In positive resists the irradiated regions are removed by chemical development to produce structures, while in negative resists the development procedures remove the unirradiated regions, leaving the cross-linked structures behind. The mechanism of silicon micromachining by PBW is more complicated. The effects and modifications to silicon by ion irradiation will be discussed in greater detail in next section.

Energy (keV)	Helium ion end of range (μm)	Proton end of range (μm)
500	1.98	5.99
800	2.88	11.74
1000	3.51	16.33
1200	4.18	21.48
1500	5.26	30.29
1800	7.72	40.69

Table 2.3. End of range depth simulated from SRIM for different energies of helium and protons in bulk silicon respectively

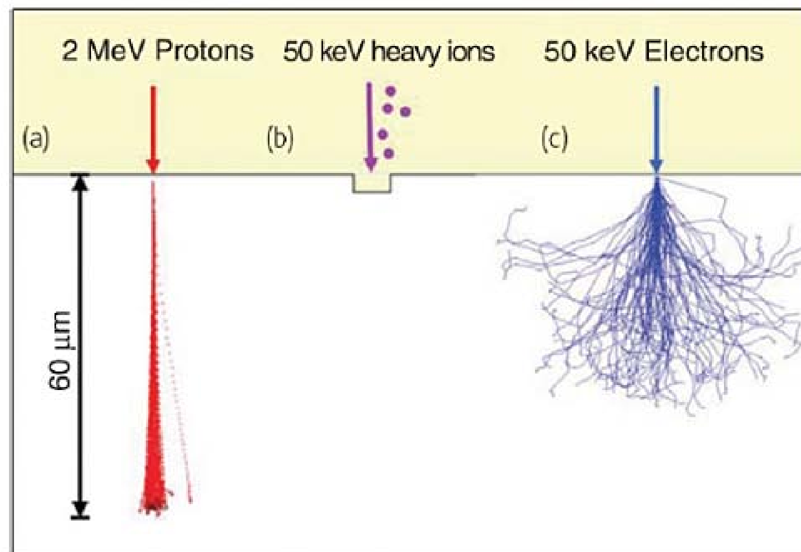

Figure 2.5. Comparison between (a) PBW, (b) FIB, and (c) electron beam writing. This figure shows schematically the difference between these three techniques. The p-beam trajectories were simulated using SRIM[41] while the e-beam trajectories simulated by CASINO[40] software. The advantage of PBW is its ability to penetrate deeper with minimal lateral broadening.[32]

2.3.1 Influence of proton beam irradiation

Proton and helium irradiation can create defects in silicon by collisions with atomic nuclei. The difference between these two ions for the same energy is the end of range, which is shown in Table 2.3.

The procedure of creating a silicon core by PBW can be summarized by the following:

a) A finely focused beam of MeV protons is scanned over the silicon wafer surface. The ion beam continually loses energy and creates many vacancies in the semiconductor at the end of range.

b) The irradiated sample is then anodized in a HF solution (the details will be presented in Chapter 4.3). The buried region of high vacancy concentration and high

resistivity stops the hole current from flowing so that the etch rate is reduced and the formation of PSi is slowed down. When the beam fluence is high enough, the etch rate is reduced to zero and the irradiated areas remain intact, surrounded by PSi.

c) The layer of porous silicon can be removed by a potassium hydroxide (KOH) solution, leaving the patterned structure on the wafer surface.

The influence of ion fluence and hole current was further studied by MEDICI, which simulates two-dimensional distributions of potential and carrier distributions in semiconductors by solving Poisson's equation. Simulation for a number of vacancy-interstitial pairs (Frenkel defects) along the ion trajectory is modeled in MEDICI simulations, shown in Fig. 2.6. The damage profile is created by 250 keV protons in silicon (blue line). The number of defects remains almost constant for the first 2.2 μm, whereas it increases by more than 10 times at the end of range.

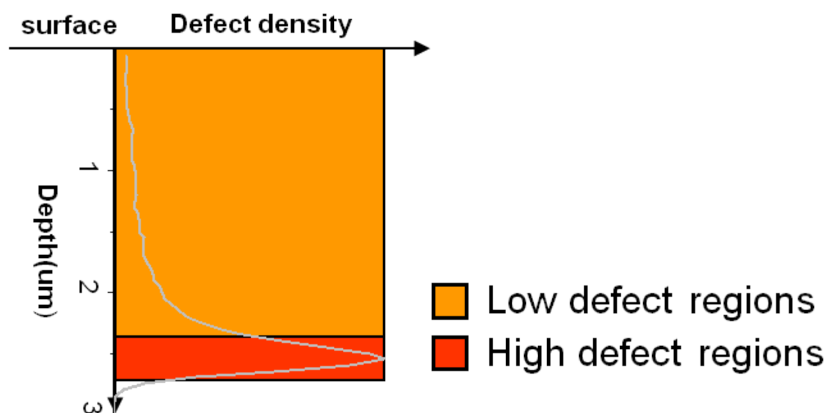

Figure 2.6. Damage profile created by 250 keV protons, showing the low and high defect regions.

Figures 2.7 (a-c) show MEDICI plots of the E-field vectors within the silicon wafer for three different proton fluences. Away from the irradiated line, the E-field vectors are induced by positive bias applied to the wafer during etching. The net charge

within the irradiated line is different from that of the unirradiated region since the hole capture coefficients are larger than the electron capture coefficients, which produces a net positive charge in the irradiated area. The quantity of charge is proportional to the defect density.

A lateral E field is caused by the net positive charge produced from the damaged region and causes the holes to be deflected away. The deflection is strongest at the high defect density region. As the fluence is reduced, the holes bend around the high defect region and flow through the lower defect region. At low fluence, only the highest density region is left unetched, creating a small silicon core (see Fig. 2.7 (d)).

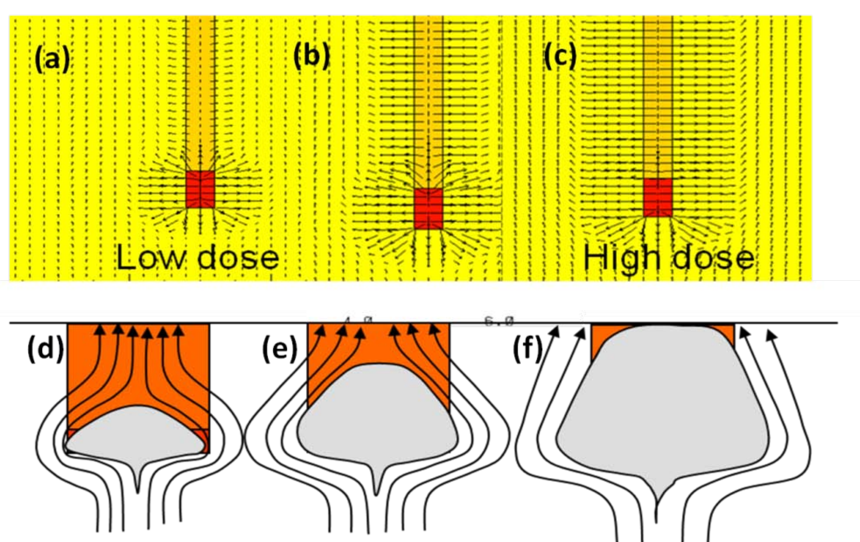

Figure 2.7. (a)-(c) Electric field distributions with increasing ion fluence simulated by MEDICI. (d)-(f) schematically show the silicon core size increases at higher fluences.

2.3.2. Ion irradiation facility at CIBA

In CIBA, a 3.5 MV high brightness High Voltage Engineering Europe Singletron^{TM} ion accelerator is utilized in a wide range of disciplines, including biophysics and advanced materials characterization. The main usage of the accelerator in this thesis is

for high performance silicon micromachining. Various types of ions can be extracted from this accelerator, but in this thesis protons (H^+) and singly-charged helium (He^+) are primarily used. The complete facility is shown in Fig 2.8. The ionized gas (hydrogen or helium) is accelerated to the desired energy by an electric field in part (1). Ions with different velocity then pass through the 90 degree magnet. The trajectory of ions is bent through 90° and the desired energy of the ions is selected depending on the ratio between the charge and mass of the ions as well as their energy.

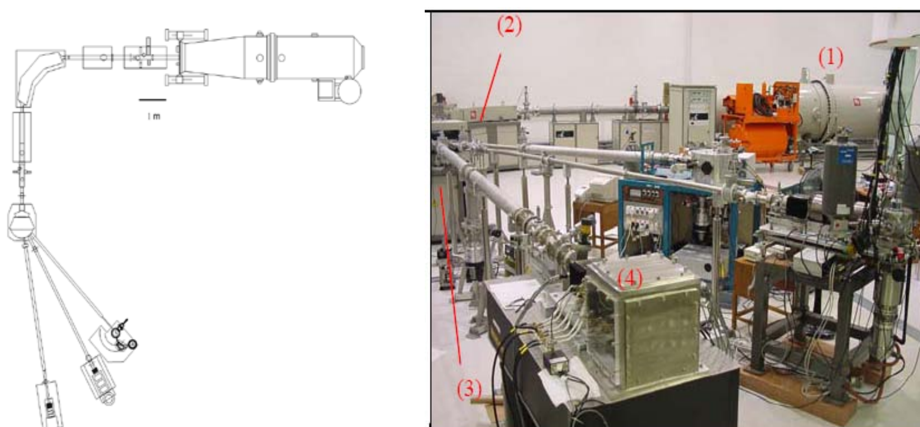

Figure 2.8. (Left) Top down schematic diagram of the micro beam setup in CIBA. (Right) Image of the CIBA micro beam facilities. (1): the accelerator, (2) 90 degree magnet, (3) switching magnet, (4) endstations

Once the strength of the magnetic field is fixed, the energy of ions which are bent through 90° is fixed. After the 90° magnet, Faraday cups are set to gather charged ions and to measure the current of the beam to optimize the beam path. A switching magnet guides the ion beam to different terminals for different purposes. There are four terminals located at 10°, 20°, 30° and 45°. Only the 10° and 45° terminals are used in this thesis for PBW and large area irradiation respectively. The beam profile

monitoring system (BPM) is situated after the accelerator and before the 90° magnet, which provides data on the intensity, profile and position of the beam.

2.3.3.1 Setup for focused proton beam irradiation

The high demagnification OM52 magnetic quadrupole triplet lenses from Oxford Microbeams are situated after the switching magnet and just before the sample chamber. The first and third quadrupoles focus the beam vertically and defocus it horizontally. Each quadrupole consists of four magnetic poles arranged in an N-S-N-S configuration perpendicular to the ion beam (see Fig.2.9). A single lens can focus the ion beam into a line, and three lenses are able to focus beam into a spot. A point focus is achieved by varying the lens currents. The lens system at the 10-degree beam line at CIBA has an object distance of 7 m and an image distance of 50 mm which provides a demagnification of 228 in the horizontal direction and 60 in the vertical direction. A resolution of 50×50 nm^2 can be achieved by shutting down the object and collimator apertures. Presently, this is the best proton beam focusing system for 2MeV protons in the world.

For PBW, precise beam scanning and control is necessary for the fabrication and design of microstructures. A software package called Ionscan has been developed for pre-defining the irradiated structures by CIBA [42, 43]. The Ionscan code works with a scan amplifier that controls the scan size of the ion beam along with the X and Y axis ratio of the scanned area. This software enhances the function of the Scan

Amplifier, and enables the writing of complicated structures. The main function of Ionscan is to move the focused ion beam in a vector style pattern with controlled blanking system and timing defined either by a normalization detector or at a uniform rate. The blanking system is situated before the switching magnet, controlled by Ionscan. It deflects the ion beam away from the original path and out of the chamber when it is switched on. This is used for blanking the beam while there is no irradiation needed. Critical parameters for the irradiation process such as irradiation fluence (numbers of ions/cm^2) of ions can also be controlled by Ionscan, since the software defines the dwell time of each location for the ion beam. With this function, varying amounts of fluence at different sections in a single silicon sample can be achieved.

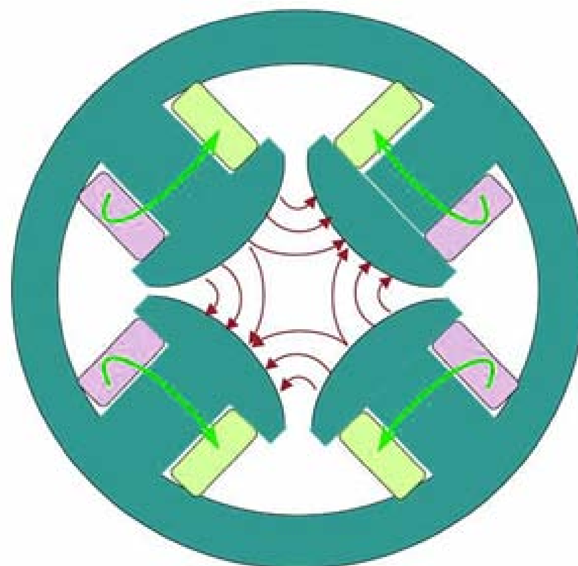

Figure 2.9. Cross sectional schematic of a quadrupole lens. Positively charged ions are travelling out of the page. Green arrows indicates the direction of current flow in the coils to lead in the desired magnetic polarity at the ends.

2.3.3.2 Setup for large area irradiation

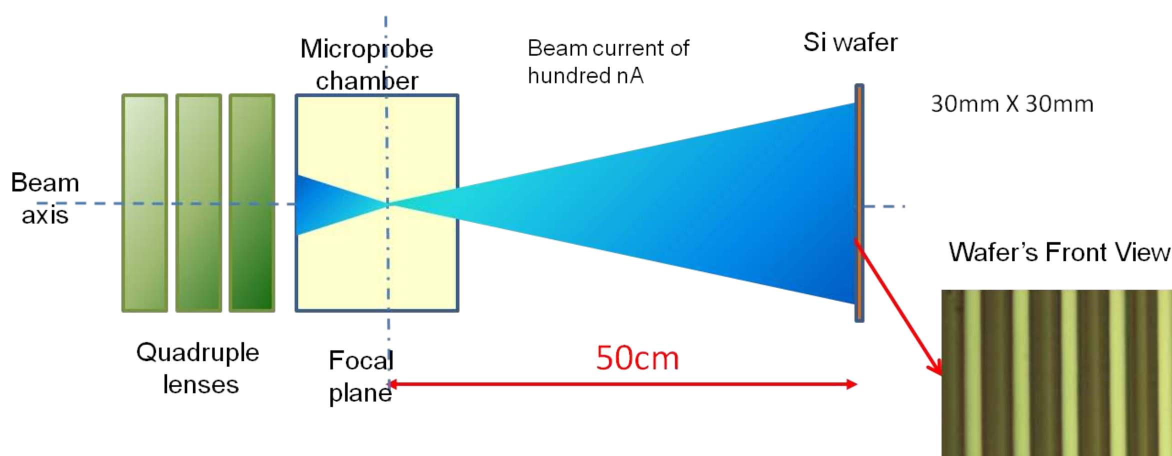

Figure 2.10. Schematic for large area irradiation.

Large area irradiation has been developed by CIBA and first applied for fabricating three dimensional porous silicon distributed Bragg reflectors [44]. This approach was an improvement from the focused proton beam writing. Instead of irradiating samples dot by dot, large area irradiation enables one to pattern a sample through a photo-resist mask. This method offers a more uniform profile of the ion beam by well aligning the quadruple lenses. It also averages the fluctuations in the focused beam current, which would lead to variations of the fluence at different locations of the beam. That is because the beam is spread out so that all pixels have small point-to-point variations in fluence instead of a large pixel-to-pixel variation in fluence. Another advantage is that the maximum irradiation size is enlarged compared to PBW. The former scan size is about 30 × 30 mm^2 using the 45° beamline while the latter is about 500 × 500 μm^2. Conventionally, a large region with a patterned

irradiation can only be produced by stitching together many smaller scanned areas. Large area irradiation removes that limitation and allows mass production.

A schematic of the 45° endstation is displayed in Fig.2.10. The ion beam is focused by three quadrupole lenses and diverges after the focal plane. The projected large area ion beam irradiates a silicon sample with a pre-patterned photo-resist mask. The sample is situated 50 cm after the focal plane, where the highly divergent beam is distributed uniformly over an area larger than 30×30 mm^2 through an extension pipe. The ion beam current can be hundreds of nanoamperes because the collimator and object apertures are wide open. The current is measured at focal plane in the chamber using a dummy-silicon sample by ORTEC 439 Digital Current Integrator.

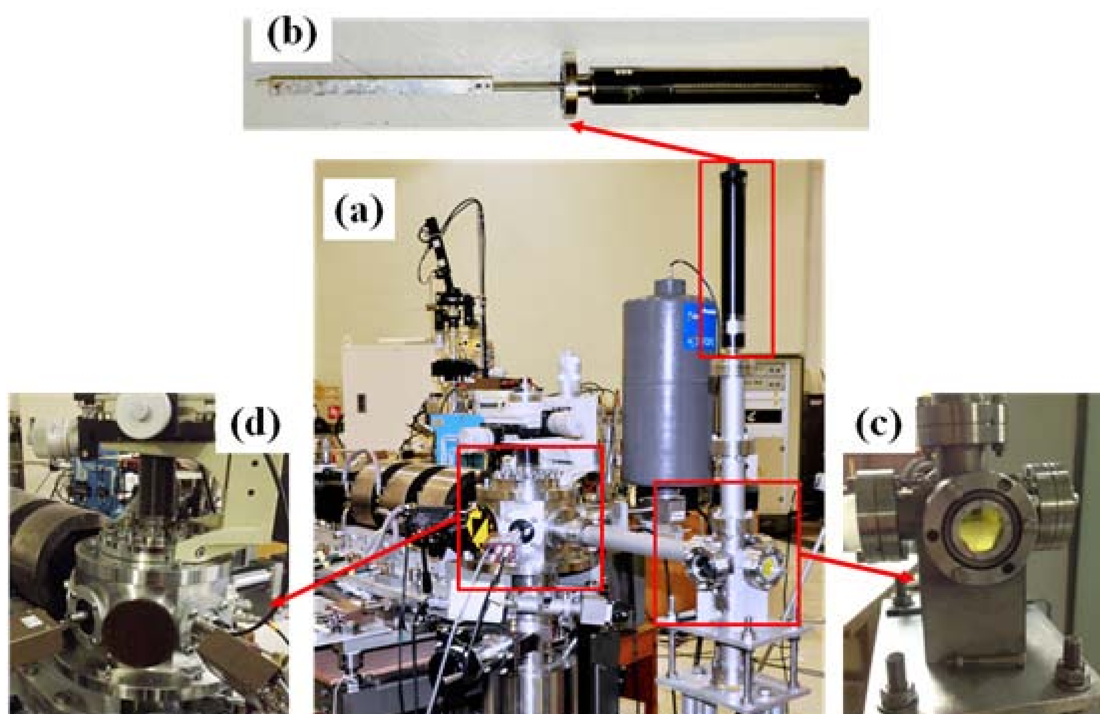

Figure 2.11. (a) large area irradiation facility. (b) The ladder and sample holder used to mount and lower samples into the ion beam path (c) Fluorescent screen placed at the end of the extension pipe (d) Nuclear microprobe chamber for direct proton beam irradiation

Figure 2.11 (c) shows the modified end of the extension pipe which allows us to change the position of the sample and roughly observe the profile of the beam. A fluorescent screen is mounted as a window in the chamber facing the ions' path, enabling us to view the uniformity and location of the large area beam. Samples are placed on a movable ladder and irradiation is conducted by lowering the sample into the irradiation position. Shadowing of the sample on the fluorescent screen is usually used to align the sample so that the entire sample is located within the ion beam area and receives complete irradiation.

The typical beam current used is about 300 nA which easily offers an even irradiation area of 25×25 mm^2 by using this modified setup. It is estimated that the fluence can be varied from 10^{13}/cm^2 to 10^{15}/cm^2.

Chapter 3

Theory of waveguides and propagation loss characterization

The basics of guided waves are presented in detail in this chapter. Opening with a brief introduction of the wave equations, some typical types of waveguides are explained. In our project, the majority of waveguides we fabricated are rectangular-shaped, and the associated wave functions can be derived from planar waveguides. The significant property of waveguides is the propagation loss. The definition and characterization methods are described in this chapter.

3.1 Fundamentals of silicon waveguides

Since they are the backbone of photonic components, the design and fabrication of waveguides with low propagation loss are the main focus of the thesis. This chapter starts with the study of the wave function and the polarization of the light, in order to understand the basic principles of optical propagation and communication.

3.1.1 Wave function

Light is an electromagnetic wave which obeys Maxwell's equations [45], which are written in the following form:

$$
\begin{aligned}
&\nabla \cdot \overline{D} = \rho \\
&\nabla \cdot \overline{B} = 0 \\
&\nabla \times \overline{E} = -\partial \overline{B} / \partial t \\
&\nabla \times \overline{H} = \overline{J} + \partial \overline{D} / \partial t
\end{aligned} \qquad (3.1.0)
$$

Where E is electric field (V/m), H is magnetic field, ρ is charge density (C/m^3) and J is current density (A/cm^2). The electric field and magnetic field are related to the electric flux density D and magnetic flux density B.

In vacuum, the wave equations appear in the following form:

$$\nabla^2 \overline{E} = \varepsilon\mu \frac{\partial^2 \overline{E}}{\partial t^2}, \qquad (3.1.1)$$

$$\nabla^2 \overline{B} = \varepsilon\mu \frac{\partial^2 \overline{B}}{\partial t^2}. \qquad (3.1.2)$$

These are the wave equations for an unattenuated electromagnetic field at an arbitrary frequency and direction. Here ε and μ are the electric permittivity and magnetic permeability of free space, $\overline{E}$ and $\overline{B}$ are the electric and magnetic field vectors that comprise the wave, respectively, and the Laplacian (∇^2) in rectangular coordinates is given by:

$$\nabla^2 = \frac{\partial^2}{\partial x^2} + \frac{\partial^2}{\partial y^2} + \frac{\partial^2}{\partial z^2} .$$

(3.1.3)

The vector field $\overline{E}$ has components

$$\overline{E} = \hat{x}E_x + yE_y + \hat{z}E_z \qquad (3.1.4)$$

where $\hat{x}, y, \hat{z}$ are unit vectors in the *x, y, z* directions. The left-hand of equation 3.1.1 can be expanded as:

$$\nabla^2 \vec{E} = (\frac{\partial^2 E_x}{\partial x^2} + \frac{\partial^2 E_x}{\partial y^2} + \frac{\partial^2 E_x}{\partial z^2})\hat{\hat{x}} + (\frac{\partial^2 E_y}{\partial x^2} + \frac{\partial^2 E_y}{\partial y^2} + \frac{\partial^2 E_y}{\partial z^2}) y + (\frac{\partial^2 E_z}{\partial x^2} + \frac{\partial^2 E_z}{\partial y^2} + \frac{\partial^2 E_z}{\partial z^2})\hat{z} \quad .$$

(3.1.5)

For a plane wave propagate in the *z*-direction in free space:

$$\frac{\partial^2 E_x}{\partial z^2} = \frac{1}{c^2}\frac{\partial^2 E_x}{\partial t^2} \qquad (3.1.6)$$

the solution of E_x is given by

$$E_x = f(z - ct) + g(z + ct) . \quad (3.1.7)$$

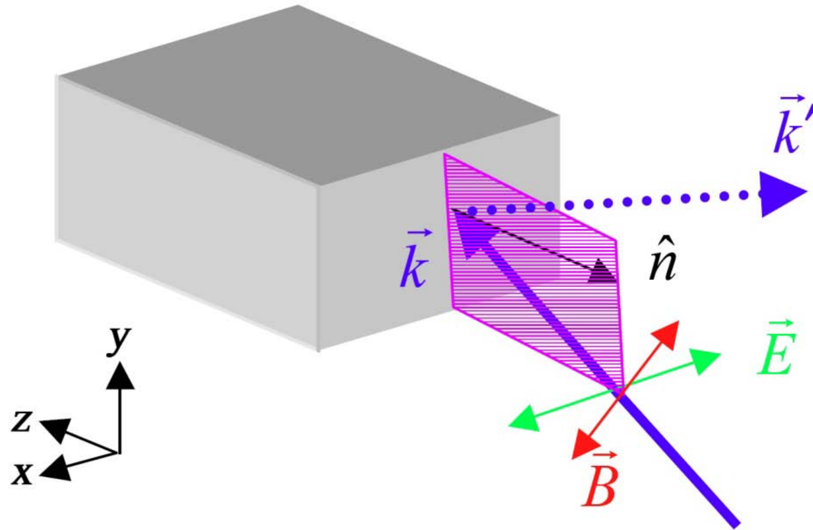

Figure 3.1. The definition of the TE light for a slab waveguide

The magnetic field $\overline{B}$ is orthogonal to the $\overline{E}$ field. Assuming that $\overline{E}$ is along the *x*-direction as in equation (3.1.6), due to Maxwell's equation $\vec{E} = -\partial\vec{B} / \partial t$, the only non-zero component of $\partial\vec{B} / \partial t$ is along the *y*-direction. Hence, both $\overline{B}$ and $\overline{E}$ are transverse to the direction of propagation, constituting a transverse electromagnetic (TEM) wave. The polarization of the wave is considered to be in the direction of the electric field associated with the wave. The propagation vector $\vec{k}$ and the interface normal vector $\hat{n}$ define a plane illustrated in Fig. 3.1 as a purple parallelogram. The

transverse electric (TE) polarization is defined as the direction of $\vec{E}$ of the wave (green arrow), which is perpendicular to the plane of $\vec{k}$ and $\hat{n}$ (Fig 3.1). Correspondingly, in the transverse magnetic (TM) polarization the $\vec{B}$ component of the wave is perpendicular to the plane of incidence (not plotted).

The $\vec{E}$ field and $\vec{B}$ field satisfies the equation

$$\vec{B} = \frac{1}{v}\vec{k} \times \vec{E} \qquad (3.1.8)$$

where $v = \frac{c}{\sqrt{\varepsilon_m \mu_m}} = \frac{c}{n}$ (3.1.9)

When a wave encounters a boundary between interfaces with different refractive indices n_1 and n_2, a Fresnel reflection occurs. Based on Maxwell's equations, the resultant Fresnel reflection coefficients of the TE and TM polarization are written as follow:

$$r_{TE} = \frac{n_1 \cos\theta_1 - n_2 \cos\theta_2}{n_1 \cos\theta_1 + n_2 \cos\theta_2} \qquad (3.1.10a)$$

$$r_{TM} = \frac{n_2 \cos\theta_1 - n_1 \cos\theta_2}{n_2 \cos\theta_1 + n_1 \cos\theta_2} \qquad (3.1.10b)$$

where n_1 is the refractive index of refraction in the medium the incident light originates, n_2 is the refractive index of the material in which the light is refracted. θ_1 is the angle of incidence, and θ_2 is the angle of refraction (shown in Fig.3.2).

According to Snell's law, $n_1 \sin\theta_1 = n_2 \sin\theta_2$, equation 3.1.10a and 3.1.10b can be rewritten as:

$$r_{TE} = \frac{n_1 \cos\theta_1 - \sqrt{n_2^2 - n_1^2 \sin^2\theta_1}}{n_1 \cos\theta_1 + \sqrt{n_2^2 - n_1^2 \sin^2\theta_1}} \qquad (3.1.11a)$$

$$r_{TM} = \frac{n_2^2 \cos\theta_1 - n_1\sqrt{n_2^2 - n_1^2 \sin^2\theta_1}}{n_2^2 \cos\theta_1 + n_1\sqrt{n_2^2 - n_1^2 \sin^2\theta_1}} \qquad (3.1.11b)$$

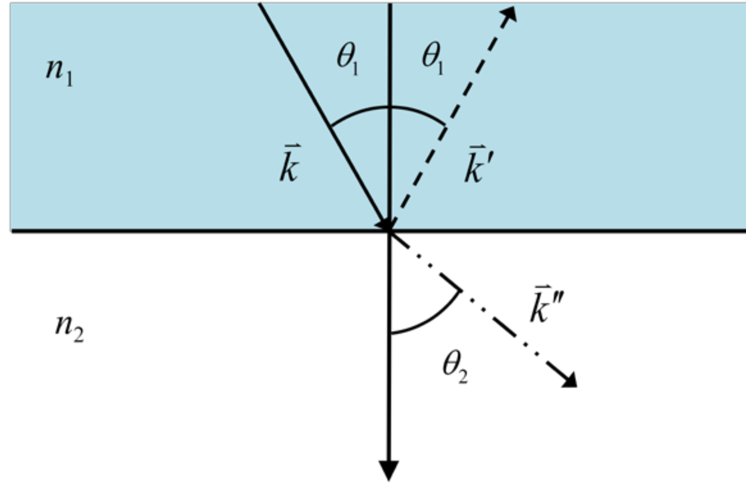

Figure 3.2. The demonstration of Snell's Law for a light ray passing from a material of higher refractive index to a lower one

3.1.2 The planar waveguide

In a planar waveguide, the relationship between the refractive indices n_1 and n_2, and the angles of incidence and refraction is given by Snells law[5]:

$$n_1 \sin\theta_1 = n_2 \sin\theta_2 \qquad (3.1.12)$$

For $\theta_2 = 90^\circ$ and $n_1 > n^2$, the incident light will encounter Total Internal Reflection (TIR) with $r_{TE} = r_{TM} = 1$. When θ_1 corresponds to the critical angle θ_c:

$$Sin\theta_c = \frac{n_2}{n_1} \qquad (3.1.13)$$

Considering a silicon-on-insulator planar waveguide, the critical angle for Si/air (n_{si} = 3.47, n_{air} = 1.00) is 16.7° and for a Si/SiO_2 (n_{SiO2} = 1.44) interface, the critical angle is

24.5°. Strong optical confinement can be achieved when the silicon waveguide is surrounded by a material with a much lower index of refraction such as silicon dioxide or air.

For $\theta_1 > \theta_c$, light is totally internally reflected in the planar waveguide. The result is a phase shift in the reflected wave:

$$\phi_{TE} = 2\tan^{-1}\frac{\sqrt{\sin^2\theta_1 - \left(\frac{n_2}{n_1}\right)}}{\cos\theta_1} \qquad (3.1.14)$$

$$\phi_{TM} = 2\tan^{-1}\frac{\sqrt{\sin^2\theta_1\left(\frac{n_1}{n_2}\right)^2 - 1}}{\cos\theta_1 \frac{n_2}{n_1}} \qquad (3.1.15)$$

The spatial rate of change of ϕ in the z-direction is the propagation constant k that is given by:

$$\frac{d\phi}{dz} = k \qquad (3.1.16)$$

As defined earlier, k_0 is the propagation constant in vacuum:

$$k_0 = \sqrt{\varepsilon_0\mu_0}\,\omega = \frac{\omega}{c} = \frac{2\pi}{\lambda_0} \qquad (3.1.17)$$

where c is the velocity of light in vacuum and λ_0 is the wavelength of light in vacuum. A propagation constant k for arbitrary material with an electric permittivity ε_m and magnetic permeability μ_m also can be determined using a similar method. The refractive index of a material can be defined as:

$$n = \frac{c}{v_p} \qquad (v_p = 1/\sqrt{\varepsilon_m\mu_m}\;) \qquad (3.1.18)$$

Thus, the propagation constant k_m can be determined:

$$k_m = \sqrt{\varepsilon_m \mu_m}\omega = \frac{\omega}{v_p} = \frac{2\pi}{\lambda_0} n = k_0 n \qquad (3.1.19)$$

When the wave propagates in the *x* direction, k can be decomposed in the y and z direction. Thus, the propagation constant is defined as [46]:

$$k_z = n_{si} k_m \sin\theta_1 \qquad (3.1.20)$$

$$k_y = n_{si} k_m \cos\theta_1 \qquad (3.1.21)$$

where k_y, k_z and θ_1 are shown in 3.3. .

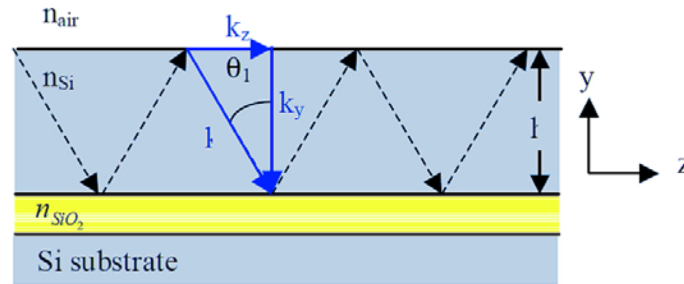

Figure.3.3. TEM wave propagates in a planar waveguide.

The propagation constant in the *y*-direction means that a wave reflects back and forth from the top and bottom material interfaces. For a wave travelling in the *y*-direction, the total phase shift ϕ_t is written as:

$$\phi_t = 2hk_y - \phi_l - \phi_u \qquad (3.1.22)$$

where ϕ_l is the phase shift introduced by the Si/SiO_2 interface and ϕ_u is the phase shift introduced by the silicon/air interface, and *h* is the height of silicon waveguide. The condition for the existence of a standing wave between the two interfaces is:

$$2hk_y - \phi_l - \phi_u = 2m\pi, \quad \text{for } m=0,\pm1,\pm2,\pm3,\ldots \qquad (3.1.23)$$

It is shown that only specific wave vectors with discrete reflection angles can be supported by the planar waveguide. The value *m* is called the mode number. When *m*

= 0, the wave with the corresponding propagation constant is defined as the fundamental mode of the waveguide. We can also define a parameter N_{eff} as the effective index of the mode:

$$N_{eff} = n_1 \sin\theta_1 \qquad (3.1.24)$$

Equation 3.1.19 becomes:

$$k_z = \beta = N_{eff} k_0 \qquad (3.1.25)$$

where an alternative parameter β is often used to represent the propagation constant. It is important to note that β is slightly different from the propagation constant defined above since it is a complex value which also accounts for the loss. It can also be written as:

$$\beta = \beta_r - j\frac{\alpha}{2} \qquad (3.1.26)$$

where $\beta = k_z$ and α is the loss coefficient. Here, for simplification, α is neglected since it is quite low in planar waveguides.

The reflection angle θ_1 can be calculated by substituting either equation 3.1.14 or 3.1.15 into Eq. 3.1.23, depending on the polarization of the wave. As an example, with a phase shift for TE polarization in the structure of Fig.3.3, equation 3.1.23 takes the form as:

$$hn_{si}\cos\theta_1 - m\pi = \tan^{-1}\left[\frac{\sqrt{\sin^2\theta_1 - \left(\frac{n_{SiO_2}}{n_{Si}}\right)}}{\cos\theta_1}\right] + \tan^{-1}\left[\frac{\sqrt{\sin^2\theta_1 - \left(\frac{n_{air}}{n_{Si}}\right)}}{\cos\theta_1}\right] \qquad (3.1.24)$$

To study the guided wave, we use a planar waveguide as a simple model [47]. However, the planar waveguide confines a wave in only one dimension, and it is not widely employed for photonic circuits. Therefore, devices with two-dimensional confinement were developed such as rib and strip waveguides. The purpose in this thesis is to fabricate SOPS strip waveguides with rectangular cross-sections. Based on the study of planar waveguides, the transverse field components of rectangular waveguides, which are the $\vec{E}$ field and the $\vec{B}$ field, are expressed by the effective index method [48]. The discussion of the effective index method for rectangular waveguides is provided in detail in Chapter 5.2.3.

3.2 Propagation loss characterization

The propagation loss is associated with wave propagation in waveguides or devices. It is noteworthy that propagation loss excludes coupling loss which is associated with coupling into waveguides and devices. As a critical parameter to define the quality of waveguides, it draws most of the interest during optimization of the performance of optical devices.

3.2.1 Experimental techniques for optical characterization

In order to study the propagation loss of SOPS waveguides, an experimental setup for optical characterization is needed. This section mainly focuses on the equipment and configuration of this setup. In this case, a laser source with a specific polarization is

important for the setup. Therefore, a free-space experimental setup has been developed to provide flexibility in data acquisition and also to offer the ability to switch between the TE and the TM polarization of the laser.

The experimental setup for optical characterization is introduced in Fig. 3.4. To facilitate the discussion of the setup, the bold numbers in the text correspond to the boxed numbers in Fig.3.4. The first piece of equipment represented in the setup is the Lightwave Measurement System (model # 8164A) manufactured by Agilent Technologies Inc. [49]. This system consists of a main part that controls and possesses a tunable laser (model # 81640A) and optical power detector interface module (model # 81618A). They are connected to the interface module in the optical detector head **(8)** (model # 81624B). This head is sensitive to wavelengths from 800 to 2400 nm. The measurement system is controlled via a General Purpose Interface Bus (GPIB) cable and card which is attached to a computer (not included in Fig.3.4). The laser source is coupled by a polarization maintaining fiber. A 3-axis stage **(1)** (Thorlab MAX311D [50]) is used to fine tune the x-y-z spacing between the FC/PC connector and the free-space collimating objective lens, which is held by an objective lens holder attached to the 3-axis stage. The diameter of the optical fiber bundle should be less than half that of the objective lens used to launch the laser light into the waveguide. Thus, a 40× objective lens with a NA of 0.65 was chosen. The output of the fiber is held by a FC fiber optic cable holder (Thorlabs [50] HFB004) that is designed to hold a patchchord with a Ferrule Connector/Physical Contact (FC/PC) connector, and it

can be clamped to the top plate of the stage. The objective lens is attached to a flexure compatible Ø1" optic holder (Thorlabs [50], HCS030). The fiber is attached to the side of the stage so that it remains stable even if the stage platform moves. Hence, the objective lens can be adjusted with respect to the fiber which stays fixed.

Laser light of wavelength 1550 nm passes through a collimating objective lens and comes in through a polarizing cube beamsplitter **(2)**, which is mounted inside a beamsplitter holder. The beamsplitter has two functions. First, it defines the polarization state of the free-space beam. The cube is placed such that only the TE polarization of the light can transmitted from it. Second, it can remove any TM polarization components within the beam. These TM polarization components are reflected perpendicular to the transmitting direction, where they are then absorbed by the beam block. A half-wave plate **(3)** is mounted after the beamsplitter, which is used to convert the TE to TM polarization or vice versa.

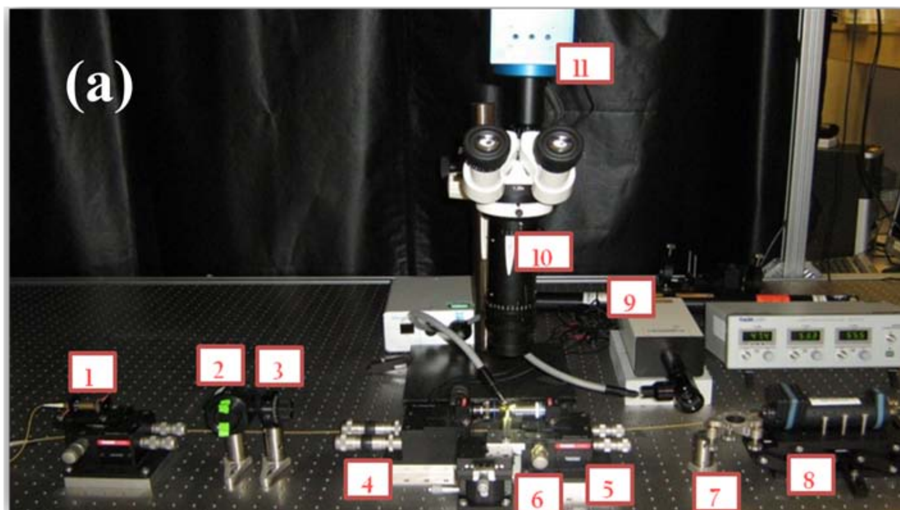

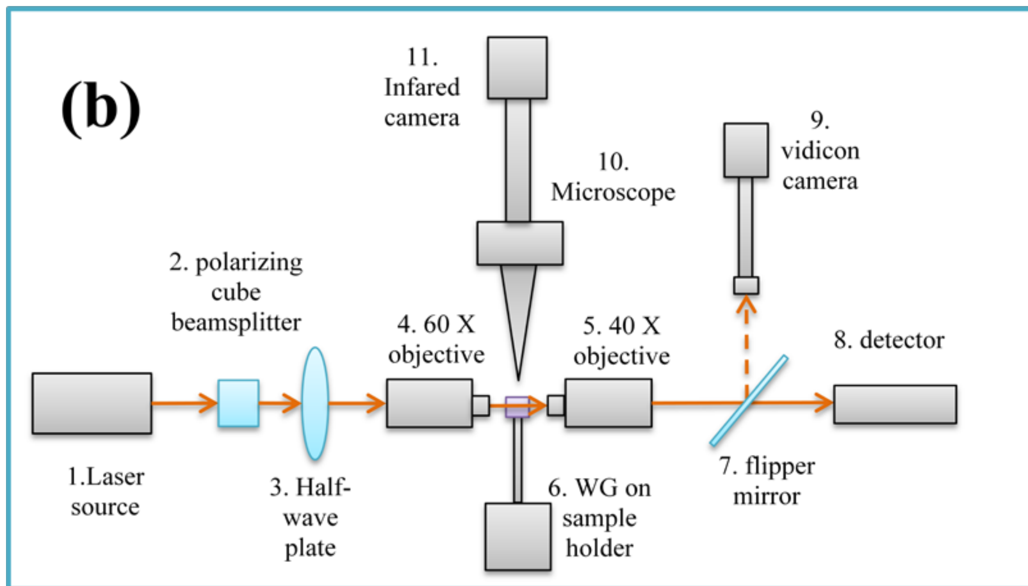

Figure 3.4. (a) Photograph for the setup (b) Schematic of the experimental set up used for optical characterization.

A 3-axis central stage **(6)** is used to hold the test device. A sample holder was machined out of aluminum to hold the test chip. The tip of the sample holder was designed so that it is smaller than the test chips. It is designed so that the sample holder does not interfere with the objective lens when it is close enough to the waveguide facets on the test sample.

The free-space beam is focused onto the input facet of a waveguide by a 60× objective that is chosen because its spot size is of the order of a micron. Light emerging from the waveguide is normally collected and collimated with a 40× objective. That lens is able to collect an image on the infrared imaging camera. Because the objective is used to focus the laser onto the waveguide entrance, the focusing of laser means it has a significant divergence. This means that the power will be launched into range of modes in the waveguide.

The cross-sections of waveguides fabricated in this thesis are about 20 μm^2, therefore a highly sensitive stage **(4)** (Thorlabs [50], MDT630A) is implemented to precisely couple the objective lens to the waveguide. It provides 20 μm of high resolution displacement by piezo actuators. Feedback is provided by these actuators, thus the position of the objective lens and the beam can be manipulated with a resolution of the order of several nanometers.

An aluminum mirror is held by a flipper mirror mount. The output beam from the test sample can be guided to a vidicon camera, or passes onto the power detector for measurement of the output power. Within such a design, the output mode from the waveguide can be detected, enabling confirmation of accurate beam coupling into the waveguide.

An InGaAs camera (Xeva-FPA-1.7-320) combined with a variable zoom tube is utilized above the waveguide for imaging light scattered from the sample. The magnification can be tuned from the variable zoom tube to observe waveguides with different lengths.

Two optical power supplies are used in this setup. One is a tunable laser source offering the exact power and wavelength used for cut-back characterization. The wavelength of the tunable laser we chose for our project is 1550 nm and the power is 10 mW. The second power supply is a broadband laser source (1525 to 1625 nm) for the scattered light technique. It has an output power of approximately 20mW. With this configuration most of the characterization work can be conducted, including

waveguides and resonators. Whilst this setup allows the greatest degree of experimental freedom, it does introduce additional difficulties in the initial alignment of the input/output objective lenses.

3.2.1.1 Calibration of the Polarization

Determination and control of the input polarization state is critical in many measurements made in this thesis. When a polarizing cube beam splitter is mounted in the light path, the polarization of the beam is fixed. Only the TE polarized light can pass to a half wave plate while TM components are reflected and absorbed by a beam block.

A half-wave plate is placed with a rotational mount. In order to define the polarization of incoming light, we use a calibrated polarizer in front of the optical detector which only allows TE-polarized light to pass to the detector. The output power varies when the half-wave plate is rotated. Maxima and minima of the output power alternately appear every 45°. The former corresponds to TE-polarized light and the latter to TM-polarized light. For experiments, a half-wave plate with 100° angle is used for launching the TE polarization; the same plate with 145° angle is used for the TM polarization.

3.2.2 Propagation loss and method for optical characterization

The propagation loss is important for evaluating the quality of waveguides. The main factors restricting the efficiency of energy transmission in waveguides are:

1) Scattering loss from the uneven distribution of refractive index or surface and interface roughness;
2) Absorption loss caused by lattice ions, impurity ions or electrons in waveguide materials;
3) Radiation loss induced by waveguide bending or optical tunnels.

The propagation loss consists of the above mentioned three losses, and is represented by the attenuation coefficient ξ (cm^{-1}) or loss α (dB/cm). When the guided wave is transmitted from L_1 to L_2, the power of wave decreases from P_1 to P_2, so

$$\xi = -\frac{1}{L_2 - L_1}\ln\left(\frac{p_2}{p_1}\right) \qquad (3.2.1)$$

$$\alpha = -\frac{10}{L_2 - L_1}\lg\left(\frac{p_2}{p_1}\right) \qquad (3.2.2)$$

It should be note that a decibel (dB) is a ratio of powers. In the following text dB is also used to specify absolute powers. It is customary to use a reference power of 1mW, so then the power is in units of dB.

Three experimental techniques are mainly used for waveguide measurements: (1) the cut-back method; (2) the Fabry-Perot resonance method; and (3) the scattered light measurement. The Fabry-Perot resonance method is specialized for very low loss waveguides measurements. Tittelbach *et. al.* pointed out that the error of the propagation loss increases with increasing attenuation when $\alpha \geq 1$ [51]. Therefore, the cut-back method and scattered light measurement are more practical for the waveguide samples discussed here.

3.2.2.1 The cut-back method

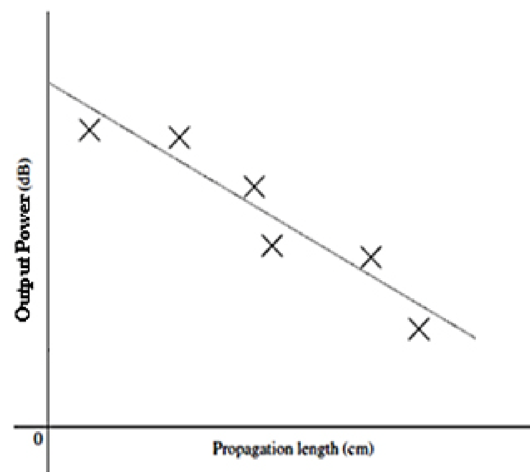

Figure.3.5. Typical results from the cut-back method.

The cut-back method is the simplest method of measuring transmission loss [1] and gives reliable results for the characterization of the transmission loss. The expression of the attenuation coefficient is associated with two different points and related powers along the waveguide. It can be improved by performing multiple measurements. We use the cut-back method that compares the output power (P1, P2, P3…) in dB of different lengths (L_1, L_2, L_3…). The output power in dB is a linear function of length, therefore the slope of P(L) is the propagation loss in the waveguide [5]. Figure 3.5 shows typical loss measurements using the cut-back method and the slope of the fitting straight line represents the attenuation coefficient (dB/cm).

Multi-point measurements are obtained by facet polishing of waveguides, discussed in detail in Chapter 4.5.

3.2.2.2 Scattered light measurements

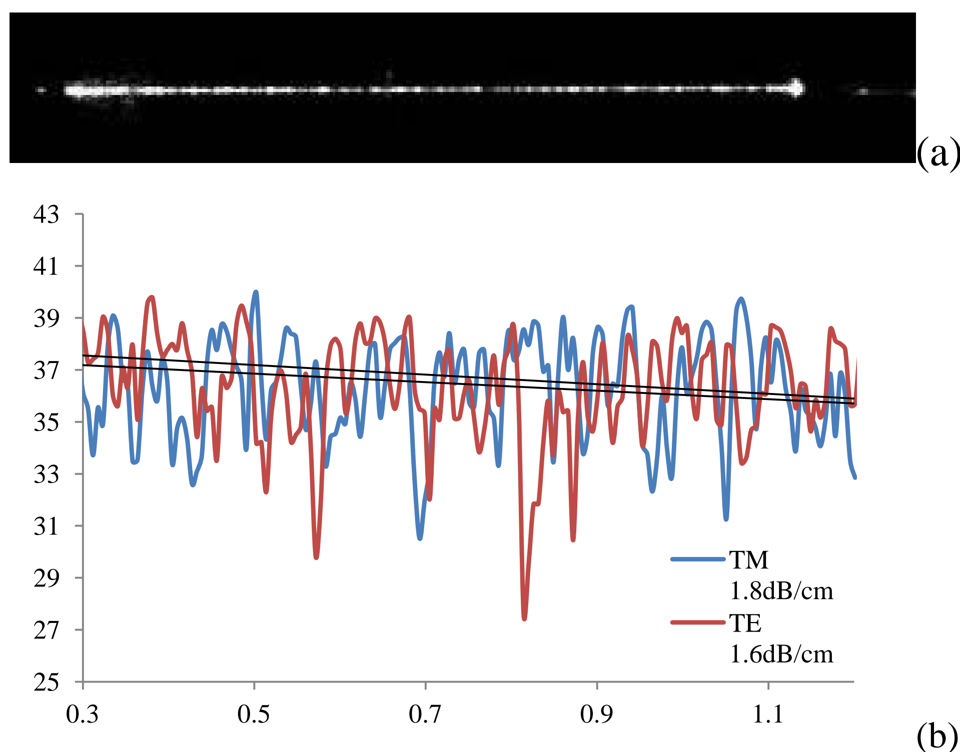

Figure 3.6. (a) Image for scattered light taken from an InGaAs camera of a silicon waveguide fabricated by large area irradiation. (b) Intensity of the scattered light. The slope of the fit is the propagation loss.

A scattered light measurement is another common and convenient technique used for optical characterization [5, 52]. This technique assumes that the intensity of the light propagating in the waveguide is proportional to the scattered light. Scattered power is a function of the propagation length for a waveguide. The ratio of the reduction of the scattered light is equal to the attenuation of power in the waveguide [53, 54]. In this thesis, we use a sensitive infrared camera to record scattered-light images instead of using an optical fiber to scan along the waveguide surface to collect data. The top view of the scattered light is shown in Fig. 3.6 (a). The image of scattered light is converted to a numerical matrix, which can be depicted as a graph. A straight line is

generated by applying the least-squares fit to a decreasing exponential, the slope of which yields the propagation loss (Fig.3.6 (b)). This method is suitable for waveguides that cannot be polished for the cut-back method, for instance, the Bragg cladding rib waveguides in Chapter 7. It is worth noticing that the scattered light method is not precise, especially when the propagation loss is low, since the resolution of the infrared camera is not high enough to distinguish the scattered-light image of low-loss waveguides. Consequently, the intensity along the waveguide almost remains stable.

Chapter 4

Fabrication for Silicon on oxidized-porous-silicon waveguides and sample preparation

In this thesis, silicon waveguides were all fabricated in bulk silicon. These structures include silicon on oxidized-porous-silicon waveguides, as well as Bragg cladding waveguides which will be described in Chapter 7. Generally speaking, the procedure of fabrication can be divided into 3 steps:

1. Ion beam irradiation. This includes focused ion beam irradiation or large area proton beam irradiation, coupled with UV lithography.
2. Anodization.
3. Oxidation.

This chapter will introduce the fabrication process in detail. When the samples are fabricated, some preparation is required before optical characterization, which is also discussed in this chapter.

4.1 PBW fabrication for silicon on oxidized-porous –silicon waveguides

Proton beam irradiation is a direct and precise approach to achieve three-dimensional control of waveguide fabrication. The schematic diagram of formation process is shown in Fig. 4.1.

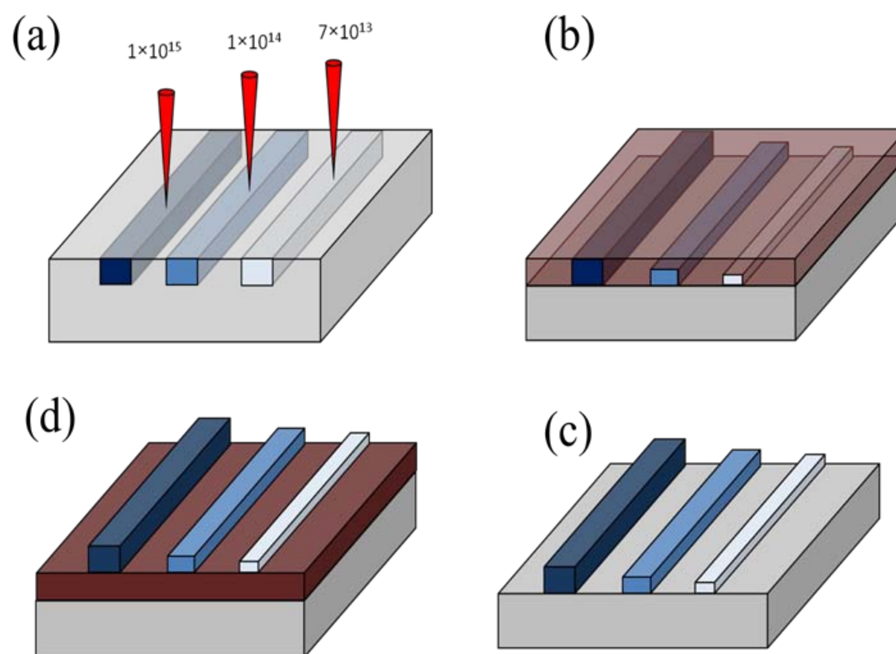

Figure 4.1. Schematic for (a) 3 different proton fluences (1×10^{15}, 1×10^{14}, 7×10^{13} ions/cm^2) irradiating a silicon substrate; (b) first anodization (c) removal of the porous silicon by KOH (d) second anodization.

1) We use H_2^+ ions generated from a High Voltage Singletron accelerator, focused by quadrupole lenses to a spot size of about 200 nm. The ion energy is chosen to be 500 keV, thus every single H^+ ions possesses 250 keV upon breaking up. The silicon sample is mounted on a Burleigh Inchworm 3D XYZ translation stage that allows an incremental movement of 20 nm. This stage is connected to the computer and

manipulated by the IONSCAN program which was introduced earlier. Waveguide patterns are irradiated in bulk p-type silicon with medium resistivity of 0.5 Ω.cm resistivity.

2) When protons penetrate the silicon substrate, lattice damage occurs in the form of vacancies, also called Frenkel defects. These defects are created along the ion path. The number of Frenkel defects is fairly constant along the first 2 μm of the ion track, however, the damage increases sharply at the end-of-range, which is about 2.5 μm (Fig.2.5). The resistivity of this region increases correspondingly, while the free-carrier density reduces. The function of such defects during a subsequent electrochemical etching process is to limit holes from migrating to the silicon/electrolyte surface. Therefore, the rate of porous silicon formation decreases.

3) The sample is etched in a two-step process shown in Fig. (b-d). The etching condition is:

- 12% HF with a current density of 100 mA/cm^2 for 74 s. The overlying porous silicon is removed using dilute potassium hydroxide (KOH).
- 24% HF with a current density of 40 mA/cm^2 for 100 s

The first anodization step creates porous silicon from the surface down to the end of ion range. A low HF concentration and a high-current density for the first anodization are chosen to provide smoother sidewalls, which is affected by the porosity of surrounding porous silicon. The factors which affect porosity are shown in Table 2.1. Subsequently, the cladding at the bottom is provided by the second anodization step.

In order to create a more stable porous silicon layer, a high HF concentration and low current is used. However, the porosity of the porous silicon layer increases, leading to a rougher bottom surface [55]. The setup for electrochemical etching is described in Chapter 4.3.

4.2 Large area irradiation for silicon on oxidized-porous –silicon waveguides

Based on direct proton beam writing, this approach was developed by using the large area proton beam facility to irradiate silicon samples coupled with a patterned photo-resist. This technique makes it possible to produce a series of waveguides with different shapes by altering different photo-masks.

A photomask is first designed with CAD software. A computer controls the laser position to write the mask patterns following the CAD file. Subsequently, the resist is developed to form a pattern. The resist acts as a mask to transfer the pattern into a chrome layer by an etching process. Lastly, the resist is removed leaving the patterned chrome layer. The resultant photo-mask is a quartz/glass substrate with patterned chrome which blocks the UV beam during UV lithography. The schematic for fabricating photo-masks is shown in Fig.4.2.

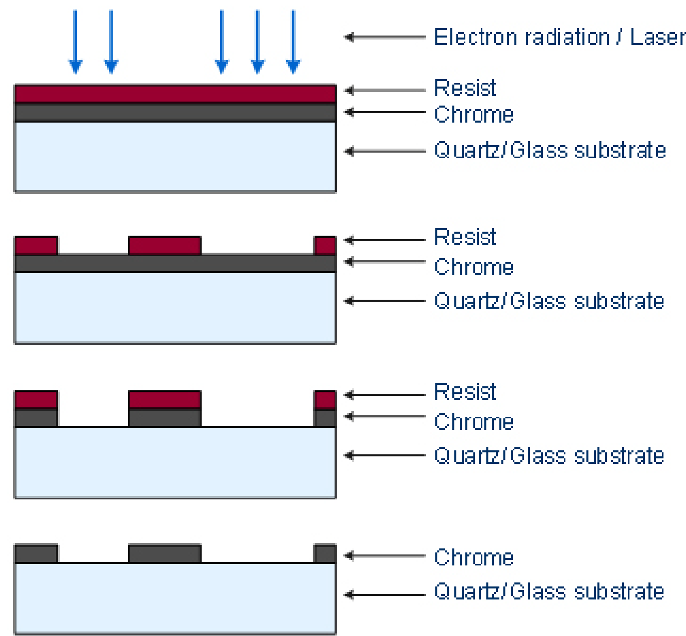

Figure 4.2. Schematic for mask printing

Silicon samples used for large area irradiation are prepared with patterned photo-resists (PR). Silicon wafer were treated with HMDS (hexamethyldisilazane) by vapor priming to improve adhesion between the sample and the PR. After that, a layer of photo-resist AZ4620 is spun onto the wafer. The thickness of the PR ranges from 1 μm to 7 μm, and is controlled by the spin rate. It is usually chosen to be 7 μm to offer enough blocking to the incoming ions. Pre-baking is conducted for stabilizing the PR at 95° c for 4 min. The UV lithography facility is at Institute of Materials Research and Engineering (IMRE). The positive photo-resist in the regions not covered by the mask is exposed to UV radiation, and chain scission occurs, reducing the average molecular weight. The shorter fragments are attached to neighboring chains by van der Waals bonds. These are more easily broken by a suitable weak solvent and hence the irradiated material is preferentially removed. After that, the samples are developed with AZ developer for one minute and fifty seconds and blow dried.

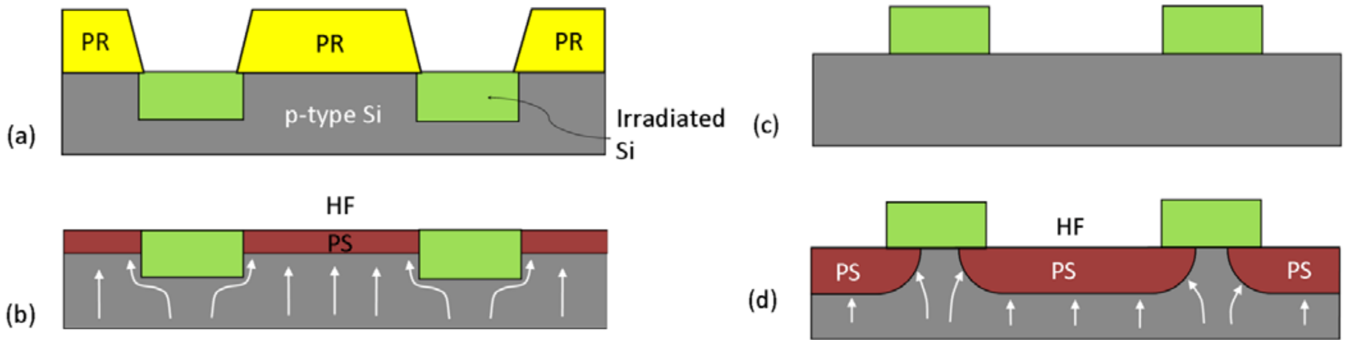

Figure 4.3 Schematics of the fabrication process showing (a) proton beam irradiation, (b) PS formation till the end of range of the ions and (c) PS removal (d) a second etching step to undercut the irradiated structures.

Figure 4.3 shows a schematic diagram of the waveguide fabrication process after samples are coated with patterned photo-resists. Irradiation is carried out on bulk p-type silicon (0.5 Ω.cm) using 250 keV protons produced from an ultra-stable single ended accelerator (HVEE Singletron^{TM}). Previously we have demonstrated the use of a highly focused beam of protons with a spatial resolution of about 200 nm to pattern waveguide structures. This direct-write technique is useful for rapid prototyping but is time consuming since only one waveguide can be patterned at one time. In this work, broad area proton irradiation is performed on a lithographically patterned silicon sample, enabling rapid prototyping of uniform patterns on substrates over a large area of 3×3 cm^2.

After irradiation and mask removal, the sample is electrochemically etched in HF. The electrochemical etching steps and conditions are similar to the steps described in Chapter 4.2.1.

4.3. Anodization setup and characterization

The anodization process was briefly described before. Here, the equipment and setup used in the anodization are presented. In addition, useful anodization parameters are given.

4.3.1 Anodization setup

Anodization, or electrochemical etching, is carried out in a hydrofluoric acid (HF) solution. A schematic of the setup is shown in Fig 2.3. HF is highly corrosive to glasses and metals, thus a Teflon beaker is used to contain the HF solution during anodization. A silicon sample is used as the anode, and a platinum grid is used as the cathode because platinum is not oxidized during anodization.

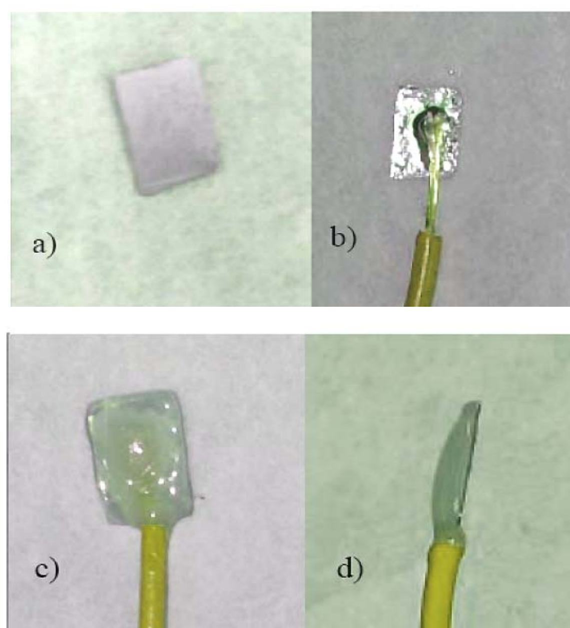

Figure 4.4. Photos showing the preparation of a silicon sample prior to anodization. (a) back of a silicon sample. (b) Gallium-Indium eutectic painted on the back surface for an Ohmic contact with a wire. (c) Epoxy covering the back surface to protect the wire from HF. (d) Side view of the prepared sample.

The silicon sample is connected to a current source by a copper wire. The plastic coating of the wire is removed at one end and the bare copper wire is dipped into 2% HF solution for better Ohmic contact. The silicon sample is also dipped into 2% HF for 10 minutes in order to remove silicon oxide and improve the contact with the copper wire.

Gallium-indium eutectic paint is utilized for attaching the back of silicon sample to one end of the wire. The toothpaste-like consistency of Ga-In eutectic mixtures depends strongly on the temperature and composition. It has a eutectic point at 14.2 wt. % and a single melting point of just 15.3 ºC. Ohmic contact between the silicon and the wire is achieved by uniformly applying the eutectic paint over the back of the sample (Fig.4.4 (b)). No contamination should appear on the surface. Araldite®, which is an epoxy adhesive, is applied to seal the Ohmic contact at the back of the sample and the copper wire (Fig.4.4(c-d)). The epoxy should be carefully removed after anodization, hence we need to adjust the ratio of the hardener and the resin during mixing to avoid the epoxy being too hard to remove. To ensure this, experience shows that the hardener proportion should be less than the resin. Anodization commences when the epoxy is totally dry.

The normal concentrations of the HF solution are 12% and 24%. For preparing 12% HF electrolyte, we mix 25 ml original HF (48%), 25 ml distilled water and 50 ml ethanol. For 24% HF, 50 ml HF (48%) and 50 ml ethanol are mixed. A direct-current power supply is required to provide a constant current. For multilayer porous silicon

fabrication, a programmable power supply (Model: Keithley 224 programmable current source) is used that can be controlled by Labview 7.1 software using GPIB (General Purpose Interface Bus) standards. The current and duration time of anodization can be tuned by programming.

The platinum and the silicon samples are placed into the Teflon beaker, facing each other for improving the electrolytic dissociation. Anodization occurs when the bias is applied and H_2 bubbles are produced at the surface of the sample. After anodization, the sample is taken out of the electrolyte because there is a little etching of silicon in HF even when no bias is applied.

4.3.2 Porous silicon formation rate

In order to determine the thickness of the porous silicon, the etching rate (porous silicon formation rate) is studied. Typically, two different resistivities of silicon wafers are used in this thesis, 0.02 Ω.cm and 0.5 Ω.cm respectively. The lower resistivity silicon wafers are mainly used for multilayer porous silicon (Chapter 7). This is because that the refractive indices vary over a large range for 0.02 Ω.cm silicon wafers[56].

The formation rate of porous silicon for 0.02 Ω.cm resistivity silicon wafer has been obtained by experiment [57]. The concentration of HF is 12%. The thickness of porous silicon is measured by scanning electron microscope (SEM) and the rate is

calculated by dividing the thickness by the etching time. The result is shown in the line chart (Fig.4.5). A red linear line is fitted by averaging three datasets.

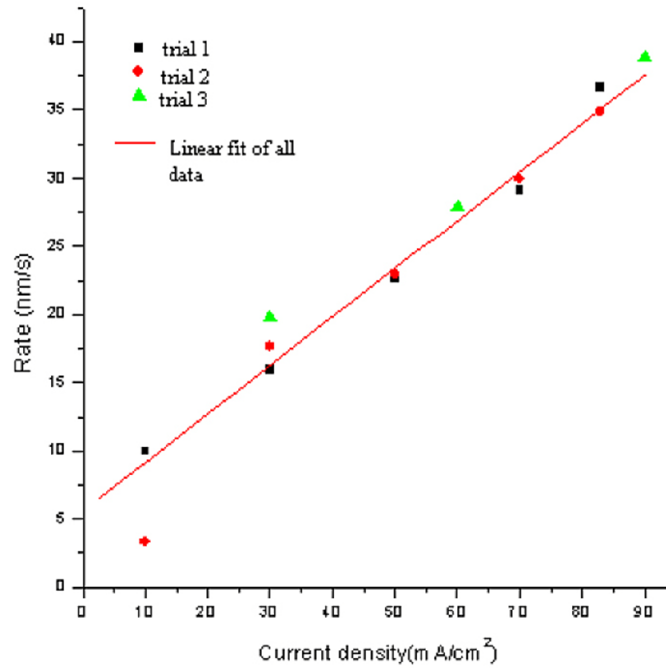

Figure 4.5. PSi formation rates versus the anodization current densities. Trial 1 (black): 10 mA/cm^2, 30mA/cm2, 50mA/cm^2, 70mA/cm^2 and 83 mA/cm^2. Trial 2 (red): 10 mA/cm^2, 30mA/cm^2, 50mA/cm^2, 70mA/cm^2 and 83 mA/cm^2. Trial 3 (green): 30mA/cm^2 , 60mA/cm2, 90mA/cm^2.All layers were etched for 30 seconds. In (b) a linear is fitted by averaging three trials. From [57]

On the other hand, 0.5 Ω.cm resistivity silicon wafers are mainly employed for fabrication of silicon waveguides. Only particular current densities are adopted. From our measurements, for 12% HF with a current density of 100 mA/cm^2, the formation rate recorded is 2.03 μm/min in 12% HF. For 24% HF with a current density of 40 mA/cm^2, the formation rate is 0.62 μm/min.

4.3.3 Refractive index of porous silicon

The refractive indices of porous silicon anodized in 0.02 Ω.cm resistivity silicon wafers were investigated by our collaborators in our laboratory [57]. The index (*n*) is resolved from the reflectance spectrum and according to the relationship

$$n = \frac{1}{2d}\left(\frac{1}{\lambda_r} - \frac{1}{\lambda_{r+1}}\right)^{-1} \quad (4.3.1)$$

where *d* is the thickness of porous silicon, and λ_r is the wavelength of the *r*-the maximum for the reflectance spectrum.

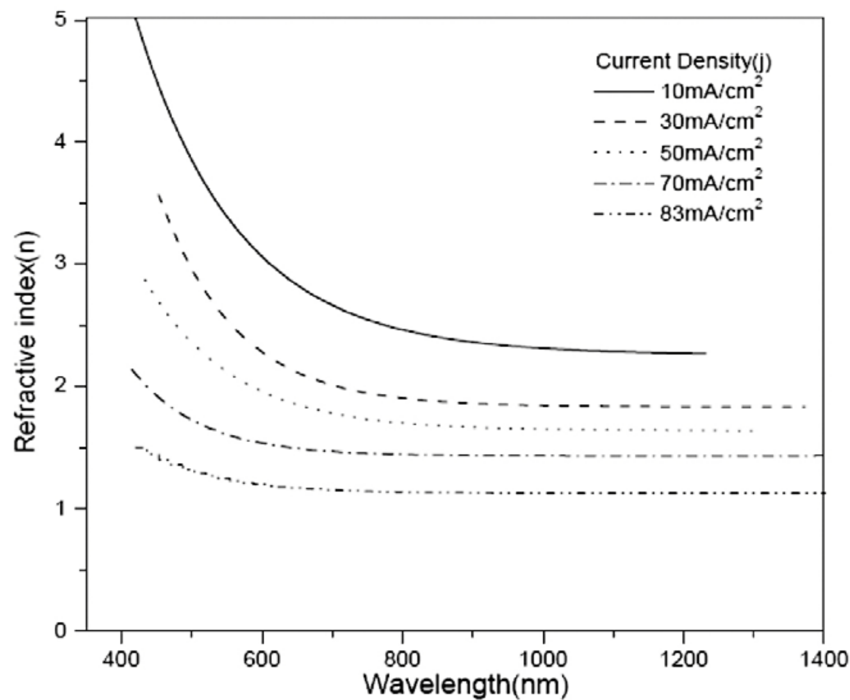

Figure 4.6. Refractive indices arising from different etch current densities plotted against wavelengths[57].

The results for refractive indices within a varied current density range are shown in Fig.4.6. When the wavelength is larger than 1400 nm, the indices remain constant. The current density we chose for producing Bragg cladding waveguides in Chapter 7 is 10 mA/cm^2 and 70 mA/cm^2, thus the indices *n* are 2.38 and 1.40, respectively.

4.4 Oxidation

Thermal oxidation is the last treatment for fabricating silicon waveguides. Oxidation at high temperature smoothens the roughness of silicon waveguides [58-60]. The benefits for the oxidation are listed below:

- 1. high temperature annealing out the proton induced damage
- 2. reducing the surface roughness.
- 3. stabilizing the PSi properties
- 4.decreasing the core size of silicon waveguides, if required

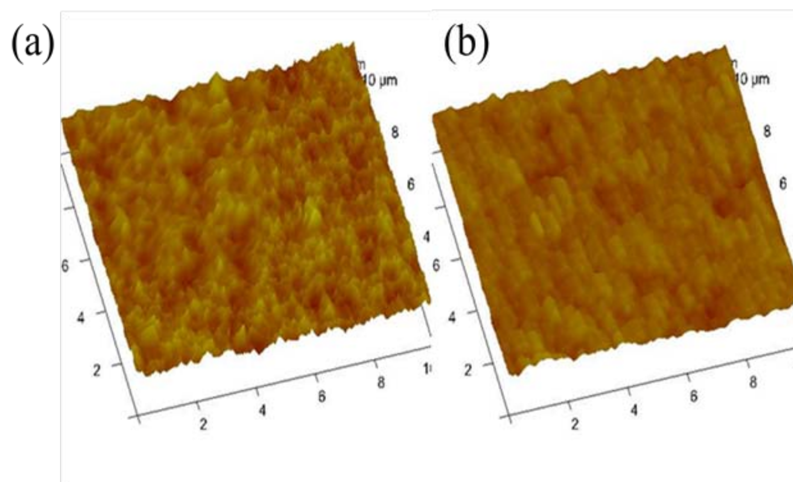

Figure.4.7. sidewall roughness of testing waveguide fabricated by PBW (a) before oxidation, roughness is 7.1 nm (b) after oxidation of 3 hours in 1100°, roughness is 3.0 nm.

In this thesis, oxidation is done in two steps: firstly, the sample is annealed under ambient conditions at 300 ºC for 3 hours to stabilize the PSi structure. Secondly, the sample is annealed at 1100 ºC to oxidize the porous layer. The typical oxidation time at a high temperature of 1100 ºC is 3 hours. Fig.4.7 shows an AFM image for a test silicon sample with a porous silicon layer before and after oxidation at 3 hours 1100 ºC. The root-mean-square roughness is decreased from 7.1 nm to 3.0 nm. More

discussions of roughness and oxidation are given in Chapter 5.2.3. We also conducted longer oxidation periods at 1100 ºC to shrink the size of the silicon waveguides.

4.5 Sample preparation

Before characterization, the fabricated samples require some preparation steps. A silicon substrate with waveguide structures is first cleaved by a diamond knife. The cleaved edge is close to the waveguide structures. The rough, exposed face is chipped and uneven, thus polishing of the end facets is required before the sample can be measured. The facility for polishing (Buehler [61] Metaserv® 2000) is shown in Figure 4.8(a). This Saw Cut Chipping Polisher is composed of a variable speed rotating plate and a water jet to lubricate the polishing pad and to take away the dust during polishing. A polishing pad is placed on the plate and held in place by a retaining ring. A sample holder designed for the polisher consists two parts (see Fig.4.8 (c)). One part is the sample holder itself with two holes in the top for easy handling by tweezers. The other part is a holder base for mounting the holder when the test chips are added or removed from the sample holder. This holder is placed in a retaining ring which is pressed by a cantilever arm in order to supply a pressure to enhance the contact between the samples and the abrasive paper (Fig.4.8 (b)). The silicon chips are mounted on the sample holder by attaching with Crystalbond 509 clear wax. The clear wax melts when the temperature is higher than 121 ºC. A hot plate is utilized to heat the wax until it melts, then the melted wax is coated on both

sides of the long edges of the sample holder. The silicon sample is stuck to a long edge of the holder by the wax. The chip surface with waveguide structures is stuck on another bare silicon chip to protect the structures during polishing. The other edge of the sample holder is mounted on two silicon chips as the same time for balance. With both test chips in place, the sample holder/mount is removed from the hot plate and allowed to cool.

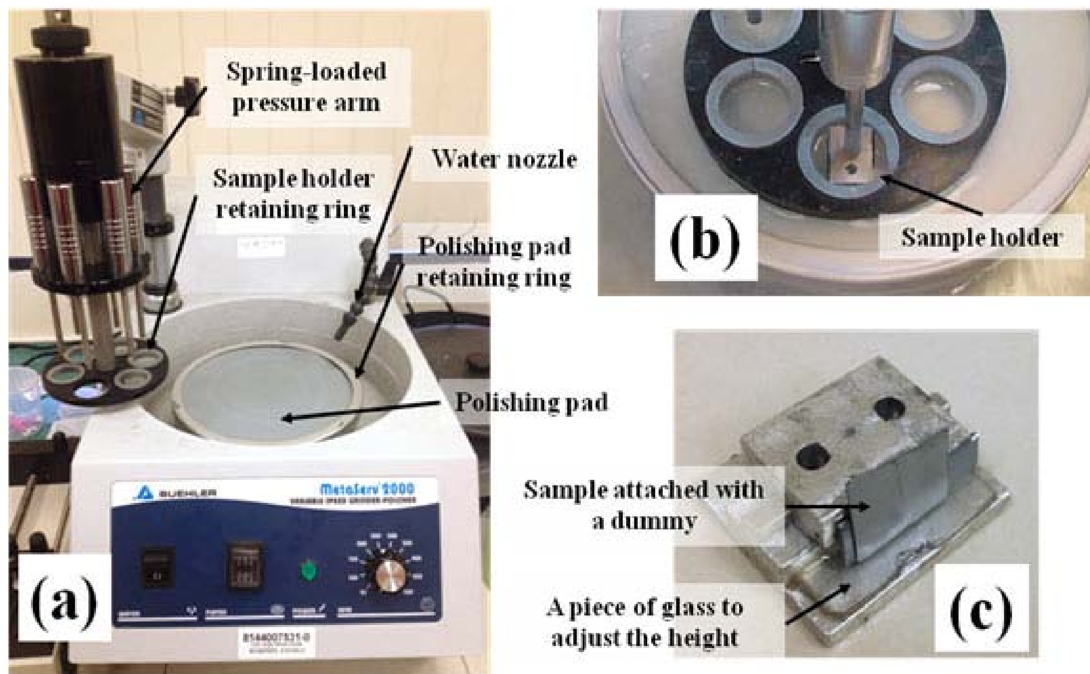

Figure 4.8. (a) Photograph of the polishing facility. (b) The pressure arm pushes down on the sample holder (c) The sample mounted on one side.

When the base and the holder are cool, the sample holder can be removed from the base. If the sample holder sticks to the base, a little acetone can be used to clean the joint part between the holder and the base. An abrasive paper is placed on the plate first and care should be taken to check the surface of the plate since any small debris on the paper can cause scratches on the facet surface. The plate is first cleaned by water rinsing and then the paper is moved from the edge of the plate and slid on, not

only to avoid any dust, but also to remove any air bubbles trapped between the plate and the paper.

From Fig. 4.8 (b), the sample holder is mounted in a retaining ring and the spring loaded pressure arm is then lowered onto the top of the sample holder. There are several scales in the arm for a qualitative measure of the applied pressure. In order to control the polishing rate, the second line from the top of the arm is used. The water nozzle is adjusted to rinse toward the center of the plate.

The polishing is affected by many factors thus it is not possible to provide exactly control. Nonetheless, the following recipe is chosen since it has provided good surface quality. A rough aluminum oxide film is used to grind the sample until the cross-sections of waveguides can be just observed by an optical microscope. The quality for the initial polishing is low and the polishing rate is fast. When the required length of the sample is achieved, further polishing can be carried out with no further changes in the sample length. Diamond Lapping Film (DLF) is used in order to give the best quality to the sample facet. The resolution (size of the diamond granules) of DLF ranges from 3 μm to 0.5 μm. After initial polishing, all dust on the facet should be removed by rinsing it with water. Then, further polishing by 3 μm DLF occurs. During 30-45 minutes polishing, almost all chips and scratches can be removed. It is necessary to change to a higher-resolution DLF when the quality of the facet cannot be improved any better for even longer polishing. A 1 μm DLF and a 0.5 μm DLF are subsequently used for improving the quality of the sample edge and similar steps are

conducted as before. When the polishing finishes, the facet of the sample should have a shiny metallic look and all scratches are tiny and in the same direction observed in a low magnification optical microscope.

The sample holder is placed back on the hot plate when polishing is finished in order to melt the wax between the silicon sample and the sample holder. After several minutes on the hot plate, the chips are easy to remove from sample holder. The polished facet of the sample is vulnerable and one needs to proceed with care. Acetone-soaked cotton swabs are used to remove any residual wax from the back of the sample. The polished edge can be cleaned by acetone soaked Kimwipes™ tissue paper.

Chapter 5

Silicon on oxidized-porous-silicon: linear waveguides

This chapter discusses the results of silicon oxidized-porous-silicon waveguides obtained from direct proton irradiation and large area irradiation. The first section shows the ability to fabricate a uniform silicon waveguide of millimeter lengths using a focused proton beam. After that, ultra-low-loss strip straight waveguides are fabricated by focused proton beam irradiation.

The large area irradiation technique was developed based on focused ion beam irradiation. Within this approach, varied shapes of waveguides including different widths can be manufactured simultaneously. The inter-relationship of surface roughness, dimensions, and propagation loss is discussed by theoretical derivation and experimental characterization.

5.1 A line focus of a quadrupole multiplet for irradiating millimeter length waveguides

This work describes a mode of irradiation which also gives very uniform fluence because the beam is not scanned. This is achieved by exciting the quadrupole lenses of a nuclear microprobe in a particular manner so that the beam is focused in one

plane but highly defocused in the orthogonal plane. Our work is based on a quadrupole triplet lens configuration [62, 63], but it is similarly applicable to other quadrupole lens configurations for focusing MeV ion beams in microprobes such as doublets [63, 64]. In the high excitation triplet, lenses 1 and 2 (L_1, L_2) are coupled together, with lens 1 assumed to be positive in excitation, lens 2 having the same magnitude but opposite sign of excitation, and lens 3 (L_3) separately excited in a positive sense.

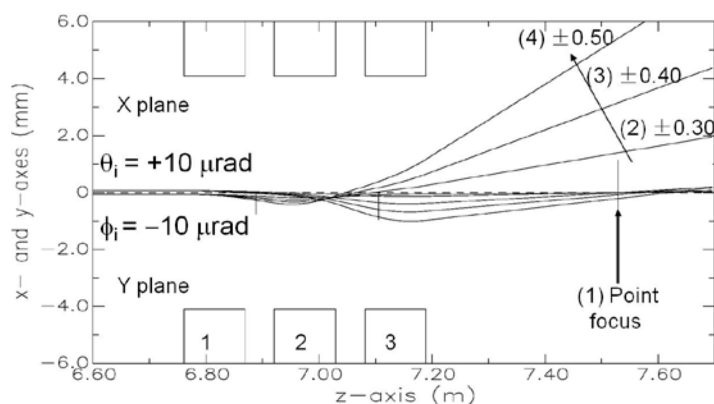

Figure. 5 1. PRAM simulations of a single trajectory of a 250 keV proton from the object aperture of the microprobe, passing through a quadrupole triplet with increasing excitation from (1) to (4). The beam remains almost focused in the vertical plane while becoming an ever-longer line in the horizontal plane. The excitations of the lenses are as follows: (1) Point focus with L1, L2 = ±0.17554, L3 = +0.16207 which remains constant. (2) L1, L2 = ±0.3. (3) L1, L2 = ±0.4. (4) L1, L2 = ±0.5.

Figure 5.1. shows examples of PRAM [65, 66] simulations of a single ion trajectory of divergence $\theta_i = +10$ μrad in the horizontal plane and $\phi_i = -10$ μrad in the vertical plane, which are limited by the size of lens pipe from the object aperture of the microprobe, passing through a quadrupole triplet. The lenses are excited more strongly from (1) to (4). Case (1) is a point focus within the chamber. For (2) to (4) the strength of L_1, L_2 is increased while L_3 remains constant. The beam remains

reasonably well-focused in the horizontal plane where the focusing effect is largely determined by L_3. While there is a small shift of the focus downstream, this is easily remedied by slightly altering L_3 to give a very micrometer-width line focus. In the vertical plane the line length extends in proportion to the increased lens strengths of L_1, L_2 for cases (2) to (4), giving a line which can be 8-10 mm in length. While one may achieve a line focus using a single quadrupole lens, as was done for grid shadow analysis of the parasitic harmonic fields of quadrupoles [65-67], this approach is limited to one fixed lens excitation, with a limited line length of hundreds of micrometers and minimum line width. It is also important to consider the maximum vertical beam length passing through the lens pipe to ensure the expanding beam does not hit it. The bore radius for the lenses of our high demagnification microprobe is 3.75 mm. Note in figure 1 the beam extent is less than 3.75 mm until the beam has exited the beam pipe.

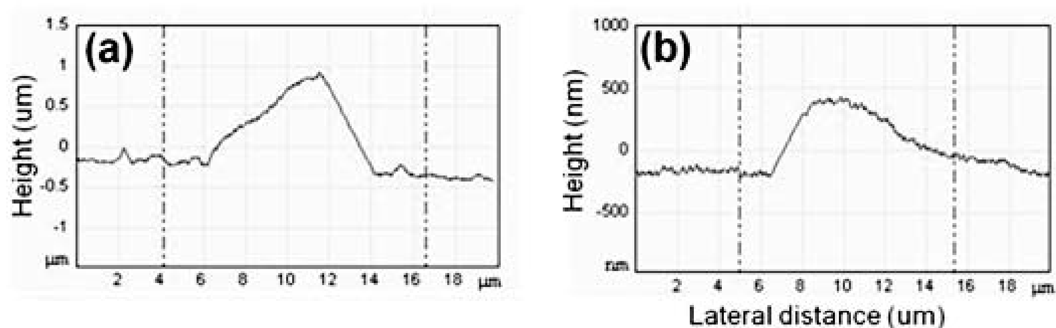

Figure 5.2. AFM line profiles across a long focused line which was irradiated in a silicon wafer. Aberrations in the line focus are manifested as an asymmetry in the final irradiated structure. These occur owing to difficulties in focusing to a line, resulting in the beam slightly (a) over- or (b) under-focused.

The process described in figure 1 is actually just an exaggerated, opposite version of the normal beam focusing procedure with the triplet, where it is typically first focused

on the horizontal plane, forming a vertical line, then collapsed to a point by changing L_1, L_2.

Equal divergence angles θ_i and ϕ_i into the lenses are actually not required, as they are used in figure 1 only to demonstrate the different trajectories in orthogonal planes. The beam length in the vertical plane is approximately proportional to ϕ_i, so one can vary the lens strength and beam angle to give the best combination of line focus and current.

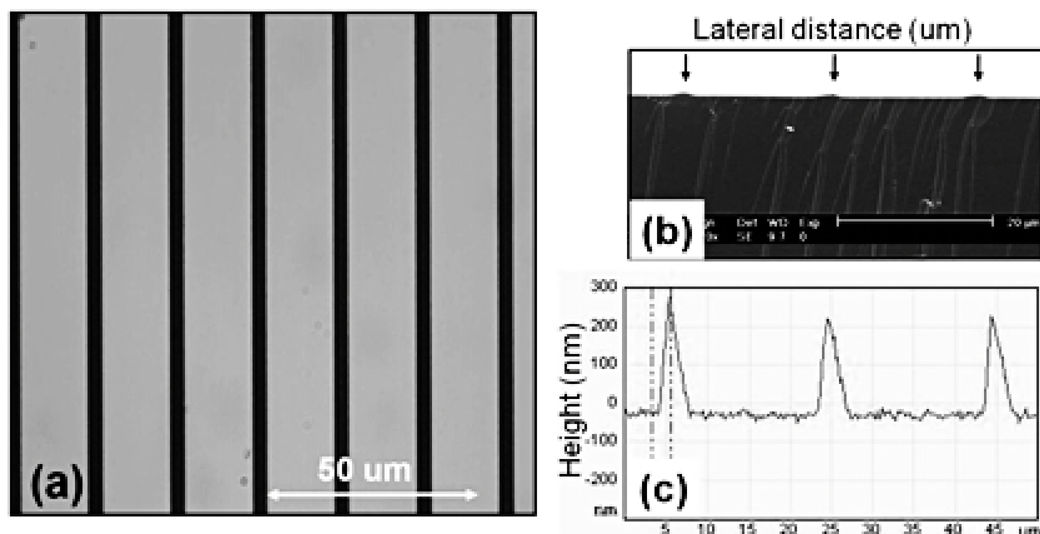

Figure 5.3. Array of lines produced with the beam focused to a long line and used to sequentially irradiate lines in a silicon wafer. (a) optical micrograph (b) AFM image (c) cross-section SEM.

The production of an optimized line focus suffers from the same concerns as producing a point focus. Care is required to produce an optimized line width during focusing. Figure 5.2 shows asymmetries across the line focus caused by incorrect focusing and alignment of the lenses and the beam through the accelerator. Sometimes the beam can be over-focused (Figure 5.2a) or under-focused (Figure 5.2b), resulting

in the non-symmetrical intensity distribution which is rather wide, more than 6 µm in this case.

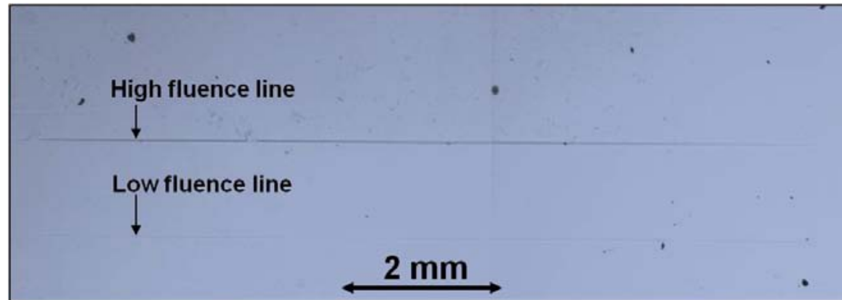

Figure 5.4. Low magnification optical micrograph of an array of 8 mm long lines produced in a silicon wafer.

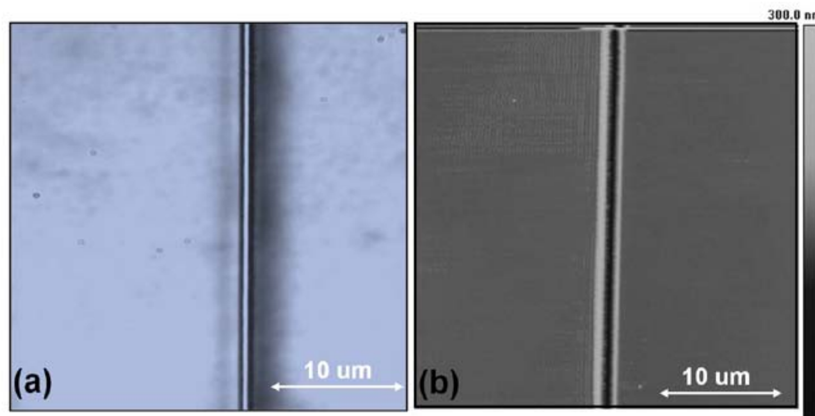

Figure 5.5. Long line produced in PMMA polymer resist, with a width of 1.5 µm. (a) optical micrograph, (b) AFM image.

Once the beam is properly focused, it can be used to create arrays of long waveguides simply by repeating the irradiation iteratively at different locations on the sample by moving the sample orthogonally to the line focus. Figure 5.3a) shows an array of lines produced in silicon with the beam of 250 keV protons correctly focused and a current of 10 nA giving a fluence of 5×10^{15} ions/cm^2 after subsequent anodization and removal of the porous silicon. Fig. 5.3(b) is a SEM image of a cross-section of such lines after removing porous silicon. Each line has a FWHM

(full-width-at-half-maximum) of about 3 μm in this case (see Fig. 5.3c)). Figure 5.4 shows similar lines created in silicon, but at a very low optical magnification so that the full line length of 8 mm can be viewed. The highest fluence line is clearly visible, whereas the lower fluence lines are difficult to pick out in such a low magnification image. It is emphasized that these lines were created over 8 mm using an irradiation time of approximate 20 seconds, with high uniformity and smoothness along their entire length.

Figure 5.5 shows a single line of 8 mm length produced with a proton beam current of about 2 nA and a fluence of approximately 5×10^{14} ions/cm^2 in PMMA, a positive polymer resist, with a FWHM width of line of about 1.5 μm. Similar images along its length show no significant changes to the width, demonstrating that the beam focus is not unduly perturbed by the lens aberrations.

5.2 Strip silicon-on-oxidized porous silicon waveguides

5.2.1 Propagation loss for strip waveguides by direct proton beam irradiation

As mentioned in Chapter 4, direct proton beam irradiation is used for fabricating silicon waveguides. A schematic of the fabrication procedure in chapter 4 shows irradiation with 250 keV protons with a 200 nm spatial resolution. By this technique, the three waveguides were fabricated with different fluences of 1×10^{15}, 1×10^{14}, 7×10^{13} protons/cm^2 in a p-type silicon wafer (0.5Ω.cm) with a lateral scan size of 2 μm. The eventual structures have a trapezoidal core shape, surrounded by a 180 nm thick oxide

layer by subsequent oxidation. Figure 5.6 shows a scanning electron microscopy (SEM) image of the cross-section of three waveguides. The rate of porous silicon formation slows down with increasing the fluence from $7x10^{13}/cm^2$ to $1x10^{15}/cm^2$, as the thickness of the porous layer is reduced from 0.7 μm to almost zero. This leads to the change in vertical size from 1.9 μm to 2.5 μm, with less etching occurring through the irradiated regions, depending on the proton range. The refractive index of the oxidized porous silicon is determined by the Bruggerman model [68]. A large refractive contrast of 2.19 between the silicon core and cladding can be achieved.

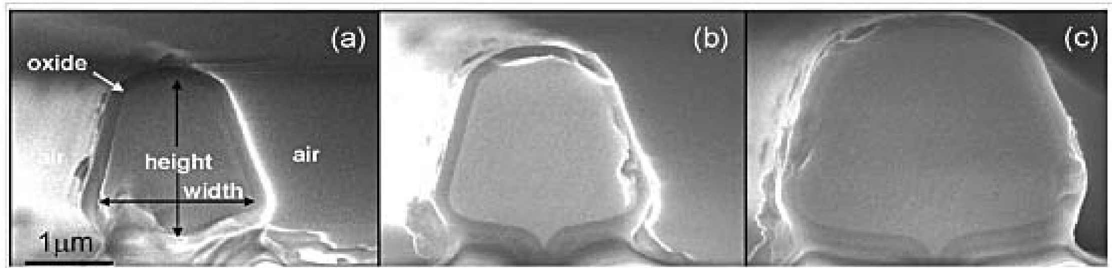

Figure 5.6. SEM of the waveguides irradiated with fluences of (a) 7×10^{13}, (b) 1×10^{14}, and (c) $1\times10^{15}/cm^2$.

From previous work [69], the scattering loss is mainly attributed to roughness. The side wall roughness is caused by the lithography in conventional SOI, whereas in silicon-on-oxidized-porous-silicon (SOPS) waveguide, the surface roughness is induced by the etching process. Thus, atomic force microscopy (AFM) was utilized to monitor the r.m.s. roughness σ for each fluence, before and after oxidation.

Fluence (protons/cm^2)	width (μm)	Height (μm)	σ (nm)	L_c(nm)
7×10^{13}	1.7	1.9	6.5	117
1×10^{14}	2.1	2.1	5.9	105
1×10^{15}	2.9	3.1	3.1	75

Table 5.1. Waveguide dimensions, σ, and *Lc* for each waveguide fluence after oxidation

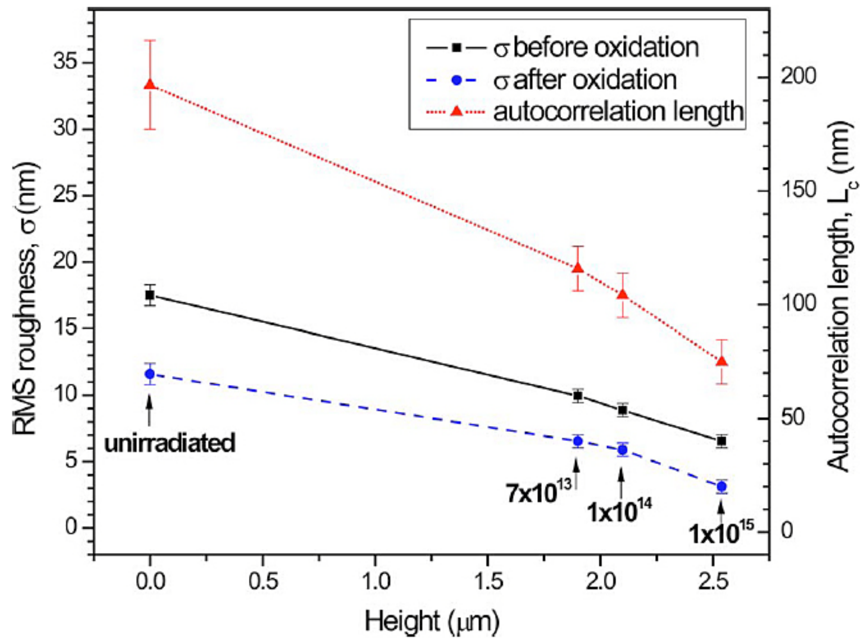

Figure 5.7. r.m.s. roughness (σ) and autocorrelation length L_c of the three waveguides as a function of height.

The r.m.s. roughness of the top and sidewall surfaces was measured by AFM separately, and then the average r.m.s. of both was calculated. The results are plotted as a function of height of the waveguide in Fig 5.7. The error bars represent the variation of σ measured covering five different sections of each waveguide. Before oxidation, the unirradiated surface at the porous/silicon interface shows a high σ of 17.5 nm. The r.m.s. σ decreases from 10.0 nm to 6.5 nm when the height of waveguide enlarges from 1.9 μm to 2.5 μm with increasing fluence. During the process, the formation of porous silicon has fluctuations, attributed to local variations of the current density of the initial silicon surface [55]. In the irradiated region, the surface roughness is determined by the uniformity of the fluence. The higher surface

roughness for low fluence is as a result of the increase in sensitivity to beam fluctuations, since the structure height varies rapidly in this fluence range. One possible method to minimize this detrimental aspect is to increase the number of scanning loops over the waveguide structure. Another method to reduce the fluctuations is to adjust accelerator settings to further stabilize the proton beam intensity. To measure the roughness at the porous silicon and silicon interface after oxidation, a dilute HF solution (2%) was used to remove the oxide on the waveguide. From the AFM image, an obvious reduction of roughness of 3 to 4 nm is obtained in the irradiated regions and 6 nm in the unirradiated region after oxidation. A minimum r.m.s. roughness of 3.1 nm can be achieved for the highest fluence on the waveguide height of 2.5 μm. The oxidation rate is faster at the convex parts of the rough silicon, leading to a smoother surface. This result is in agreement with the previous result of σ of about 10 nm and 2 nm obtained before and after oxidation for SOI strip waveguide fabricated using state-of-art lithography and etching techniques. Another factor affecting the scattering loss is the autocorrelation length L_c. Autocorrelation length is a parameter related to correlation functions which is involved in a numerical assumption of scattering loss and we will discuss it in Chapter 5.2.3.[70] We observe that the initial unirradiated PS/Si interface gives an L_c of 200 nm, then the value reduces from 117 nm to 75 nm with increasing height and fluence.

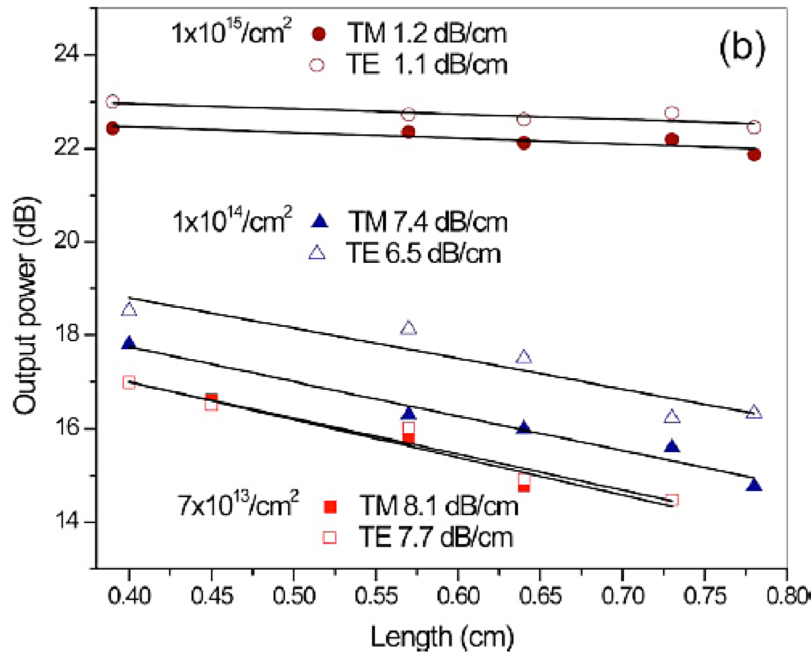

Figure 5.8. Propagation losses for 7×10¹³/cm2 (□, ■), 1×10¹⁴/cm² (△, ▲), and 1×10¹⁵/cm² (○, ●) after oxidation. The empty shapes represent the TE polarization, and the filled shapes represent TM polarization. The straight line shows a linear fit of the output power (dB) as a function of length.

Optical characterization was carried out in both TE and TM polarizations with a 1550 nm infra-red laser source. Propagation loss was measured by the cutback technique (see Fig. 5.8). Table 5.1 shows the data for roughness and *L*c, for each waveguide after oxidation. As the fluence increases from $7\times10^{13}/cm^2$ to $1\times10^{15}/cm^2$, a significant reduction is observed in loss, from 7.7 dB/cm to 1.1 dB/cm for the TE polarization and 8.1 dB/cm to 1.2 dB/cm for TM polarization. Each output power is from three independent measurements and the average is taken. The experimental error for propagation losses is approximately ±0.01. The same experimental errors are applied in the former chapter as well. In conventional SOI strip waveguides, the scattering loss is proportional to σ^2 [71]. A stronger surface-roughness effect is expected for SOPS waveguides, because the scattering loss contributed from the top and bottom surface cannot be neglected, in contrast to SOI waveguides. Here, it is obvious that a

decrease in surface roughness by a factor of two causes the propagation loss to significantly decrease. Currently, we reported a much better propagation loss than earlier studies of about 5-10 dB/cm. [72, 73]

5.2.2 Low loss strip waveguides by large area irradiation

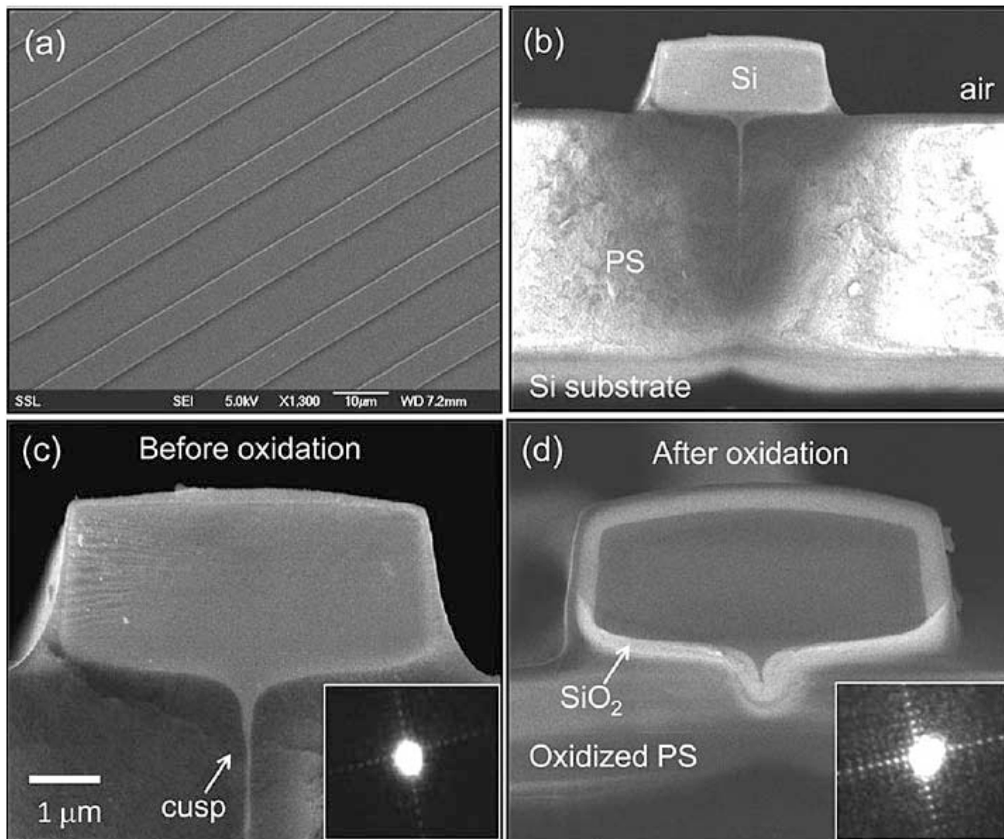

Figure 5.9. SEM image of the (a) top and (b) cross-sectional view of the waveguides. A close up of a waveguide (c) before and (d) after oxidation. The insets show the output modes imaged from the end facets of each respective waveguide.

The resultant structure consists of a silicon core that acts as a waveguide surrounded by the porous silicon. A high index contrast exists between silicon core and porous silicon (Fig. 5.9).

Optical characterization of the waveguides is conducted for both the TE and TM polarizations at 1550 nm wavelength using the cutback technique. The propagation loss of waveguides is shown in Fig. 5.10, which is expressed by the output power from the waveguides with respect to waveguide length. Before oxidation, the modes propagating in the waveguide suffer from a high loss of 10.3±0.6 dB/cm and 9.1±0.3dB/cm for the TE and TM polarization. After oxidation, this is significantly reduced to 1.6±0.1 dB/cm and 1.4±0.2 dB/cm, respectively.

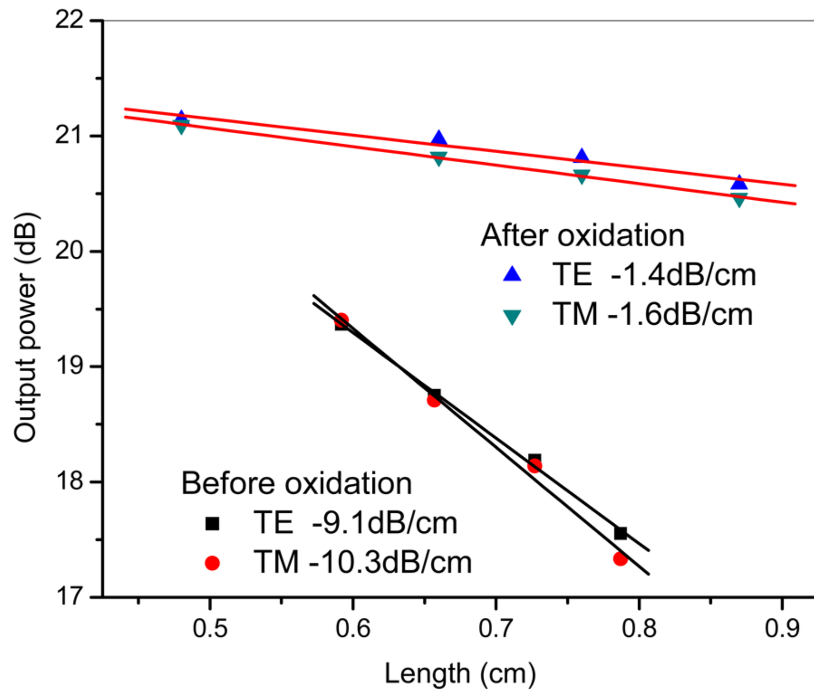

Figure 5.10. Cutback measurements of a waveguide before and after oxidation. The loss curves are determined from fitting based on slopes.

	Sidewalls		Bottom surface	
	σ (nm)	Lc(nm)	σ(nm)	Lc(nm)
Before oxidation	25	130	30	170
After oxidation	7	138	10	190

Table 5.2. Effect of oxidation on the bottom and sidewalls of the waveguides.

It is important to understand the mechanism that controls the propagation loss in order to improve the quality of the waveguides. The resistivity of the silicon used in this work is 0.5 Ω.cm. With such a high index contrast, the propagation loss is mainly induced by the surface roughness, since the scattering loss scales proportionally to $n^2 = n_{core}^2 - n_{clad}^2$ [74]. Conventional silicon waveguides may be fabricated using SIMOX wafers which provide smooth top and bottom surfaces after high-temperature annealing of the implanted oxide layer. Thus, the propagation loss is mainly affected by the lithographic process [71]. For the full isolation by oxidized porous silicon (FIOPS) process, interface roughness is formed at the PS/Si dissolution boundary during lithography and the anodization process [55]. The propagation loss is also affected by the bottom roughness as well as the sidewall roughness. Therefore, both bottom and sidewall roughness should be measured by AFM. We used 2% HF solution to remove the oxide layer around the waveguides. Consequently, by implementing such a process, the waveguides are almost detached from the substrate. After that, a piece of scotch tape is stuck on the top of the waveguide. With this adhesive tape, all waveguides can be completely separated from the substrate by mechanical exfoliation from the original silicon and stick to the tape. From direct measurement by AFM, the top surface roughness is 2-3 nm. As the top surface is only slightly affected by the etching process, the scattering loss associated with this surface can be ignored in this case.

Figure 5.11 (a) shows a SEM image of the bottom of the waveguide with the cusp running along its length. The AFM images in Fig. 5.11(b) are from across the sidewalls and bottom of the waveguide, which is indicated by the white box. The roughness results are shown in Table 5.2. It is obvious that oxidation reduces both the sidewall and the bottom roughness. After oxidation, the r.m.s. roughness value of the sidewalls is significantly reduced from 25 nm to 6 nm, while that of the bottom surface decreases from 30 nm to 10 nm. The bottom surface roughness exhibits a higher value compared to that of sidewalls because of the different formation processes involved To further smoothen the sidewalls, a high-current density of 100 mA/cm^2 and low HF concentration of 12 % was applied. Porous silicon formed under such a condition is fragile and can be removed by following steps. The bottom interface is produced by the second etching step, which uses a current density of 40 mA/cm^2 at 24% HF to separate the waveguide structure and the silicon substrate. Under this condition, the porous layer is more robust than that formed under the first etching step. However, the porosity of the former is higher than the latter. Hence, a rougher bottom surface is produced. An increase in the autocorrelation length L_c is observed after oxidation for both the bottom surfaces and sidewalls which is slightly lower than the L_c values reported on porous silicon and silicon interfaces (190-270 nm) [55]. Much lower L_c values of 50nm could be obtained with a similar r.m.s. roughness of about 10 nm, by conventional SOI waveguides fabricated by a UV lithography and

etching process [60]. A detailed discussion regarding the relationship between L_c and scattering loss is provided in Chapter 5.2.3.

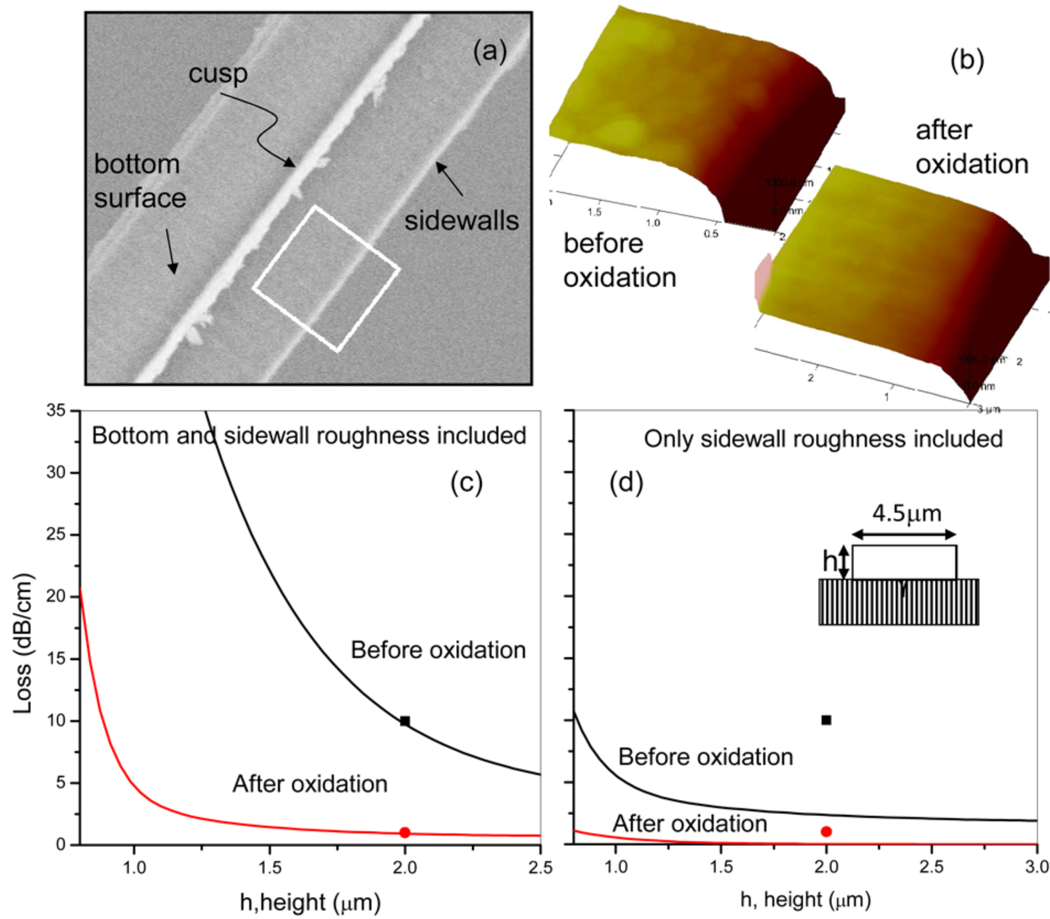

Figure 5.11. (a) SEM image of the underside of the waveguide. (b) AFM image across the bottom and sidewalls of the waveguides. Calculated scattering loss due to (c) both the bottom and the sidewalls and (d) solely due to the sidewall roughness. The measured losses for waveguides (■) before and (●) after oxidation are overlaid on both plots.

Numerical simulations of the scattering loss are performed using the 3D scalar software BeamProp^{TM} [75] with σ and L_c obtained from AFM measurements. BeamProp^{TM} simulates the sidewall roughness following methodologies based on physical mechanisms developed by Marcuse *et. al* [76]. The bottom roughness profile taken from AFM measurements is considered as a random perturbation to the height in the taper function. Simulations are conducted regarding the fundamental mode

propagation, since overlap integral analysis indicates that the fundamental mode carries most of the optical power in the regime where scattering loss is significant. A similar analysis has been performed previously by Lee *et. al*. [71].

The simulation results are shows in Figure 5.11(c-d). The simulated scattering loss from the bottom and sidewall roughness is as a function of height within a constant width of 4.5 μm with a cusp included. From Fig. 5.11 (d), when considering both bottom and side wall roughness, the experimental data matches the simulated data, which indicates that the surface roughness is the dominant contribution to propagation loss. When only the sidewall roughness is included in the simulation, the loss obtained from the experimental data is obviously higher than that from the simulated data, indicating that the bottom roughness critically affects the scattering loss and has to be taken into account for accurate theoretical analysis. For simulation, the surface roughness is obtained by calculating the root mean square value of the side wall and bottom roughness. Lee *et. al.* [71] showed that the loss increases sharply when the waveguide width reduced. This is due to the fact that the interaction of the mode with the sidewalls is enhanced within a smaller waveguide width. In our work, similar behavior exists as the increasing roughness of the bottom surface causes increasing loss when reducing the waveguide height. These cases can be adopted to predict the loss of such waveguides as the dimensions get smaller. By continued oxidation, it is possible to reduce the size of the waveguide, and at the same time reduce both the bottom and sidewall roughness and the loss of the waveguides.

5.2.3 Strip waveguide with various dimensions

In order to investigate the analytical model for scattering loss and its relation to experimental data, we used a large area irradiation fluence of 5×10^{13} protons/cm^2 to fabricate more strip waveguides with different widths. The mask designed for this work includes 3 μm, 4 μm, and 5 μm-width waveguides. After UV lithography on AZ photo-resist and large area irradiation, the actual width of the waveguides is not the same as the design. In addition, we can use oxidation to change the dimensions of the waveguides. Six types of samples were obtained for this study. SEM images show the waveguide with a designed width of 5 μm after 9 hours oxidation in 1100° C (in Fig. 5.12).

Design width (μm)	Oxidation condition	Actual height (μm) ± 0.01	actual width (μm) ±0.01	Propagation loss (dB/cm)	
				TE	TM
3	9h	1.98	3.91	7.1	7.7
	3h	2.01	4.00	6.46	6.55
4	9h	1.97	4.06	5.4	5.6
	3h	1.99	4.10	5.61	5.71
5	9h	1.98	4.15	4.19	4.25
	3h	2.02	4.60	1.4	1.6

Table 5.3. Summary of propagation losses with varied dimensions

Optical characterization was accomplished by the cut-back method. The actual height and width are precisely measured from SEM images. The data are summarized in Table 5.3.

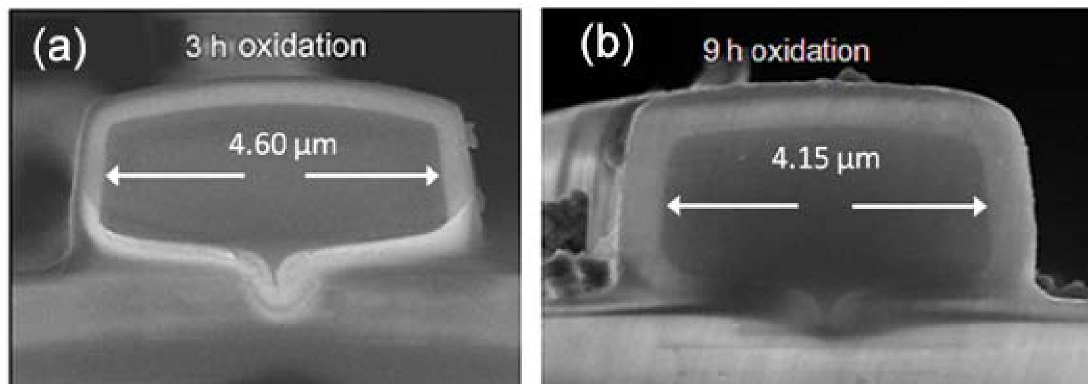

Figure 5.12. SEM images of a waveguide with a design width of 5 µm (a) taken 3 hours in 1100° oxidation (b) taken 9 hours in 1100° oxidation. The oxidation layer is enlarged with longer oxidation time.

5.2.3.1. Payne model for scattering loss

A numerical analysis of the propagation loss was performed based on the Marcuse model and developed by Lacey and Payne [70, 76, 77]. We use silicon on oxidized-porous-silicon where the index contrast Δn between Si and oxidized porous silicon is ~2. Hence, our silicon waveguide satisfies the condition of a high index difference system, in which the scattering loss is dominant over the propagation loss [69].

The analytical expressions for the scattering loss α with respect to the surface roughness were described by Payne *et.al.* [70] as follow:

$$\alpha = \frac{\sigma^2}{k_0 l^4 n_1} g(V) f_e(x,\gamma) \quad (5.1.1)$$

where $g(V)=\frac{U^2V^2}{1+W}$, and $f_e(x,\gamma)$ is defined by

$$f_e(x,\gamma)=\frac{x\left\{\left[(1+x^2)^2+2x^2\gamma^2\right]^{1/2}+1-x\right\}^{1/2}}{\left[(1+x^2)^2+2x^2\gamma^2\right]^{1/2}} \quad (5.1.2)$$

U, V, W are dimensionless waveguide parameters given as below:

$$\begin{aligned} U &= d\sqrt{n_1^2k_0-\beta^2} \\ V &= k_0 d\sqrt{n_1^2-n_2^2} \qquad (5.1.3) \\ W &= d\sqrt{\beta^2-n_2^2k_0^2} \end{aligned}$$

For convenience, other waveguide parameters are denoted as:

$$\begin{aligned} \Delta &= \frac{n_1^2-n_2^2}{2n_1^2} \\ x &= W\frac{L_c}{d} \qquad (5.1.4) \\ \gamma &= \frac{n_2V}{n_1W\sqrt{\Delta}} \end{aligned}$$

where σ is root-mean-square amplitude of the sidewall roughness and L_c is the autocorrelation length. The autocorrelation length characterizes the surface roughness $\tilde{R}(\Omega)$, which can be related to the autocorrelation function $R(u)$ through a Fourier transform according to Wiener's hypothesis[78],

$$\tilde{R}(\Omega)=\int_{-\infty}^{\infty}R(u)\exp(i\Omega u)du \quad (5.1.5)$$

and $\sigma^2=R(0)$

The autocorrelation function $R(u)$ can usually be expressed in two different forms:

$$R(u)=\sigma^2\exp\left(-\frac{|u|}{L_c}\right) \qquad \text{(exponential function)} \quad (5.1.6)$$

$$R(u) = \sigma^2 \exp\left(-\frac{u^2}{L_c^2}\right) \qquad \text{(Gaussian function)} \qquad (5.1.7)$$

It has been shown that an exponential autocorrelation function is a more realistic model for the surface roughness [79]. The autocorrelation length L_c in an exponential function is defined as a characteristic length of the autocorrelation function of the surface roughness.

5.2.3.2 The Effective Index method

Payne's method is employed for infinite planar waveguides. In order to obtain the expression of the attenuation coefficient for real rectangular-like waveguides as in our work (shown in Fig. 5.1.2), the propagation constant β should be determined using certain assumptions. Marcatili [80] proposed a methodology to resolve the three-dimensional waveguide problem in rectangular core waveguides. Unfortunately, the method is only valid when the contrast of refractive index between the core and cladding is small.

As an alternative, the effective index method is a simple approach to transform the three-dimensional waveguide problem to two dimensional waveguide problem. First, the effective index is defined as Eq.3.1.24:

$N_{eff}=\beta/k_{0},$ (3.1.25)

where β is the propagation constant.

As depicted in Fig. 5.13, a rectangular waveguide can be decomposed into two planar waveguides (Figure 5.13 (b) (c)). For this thesis, n_1 is the refractive index of the

silicon core (3.5) and n_2 is that of silicon dioxide surrounding the core (1.45). It is noteworthy that these two planar waveguides are not independent. Shown in Fig. 5.13 (b), such a slab waveguide has the same refractive index as a rectangular waveguide. However, the refractive index of the waveguide shown in Fig. 5.13 (c) is N_{eff} rather than n_1. The effective index can be resolved by the dispersion relationship.[48]

$$\begin{aligned} Kb &= m\pi + \Phi_s \Phi_c \\ m &= 1, 2, 3, \ldots \end{aligned} \qquad (5.1.8)$$

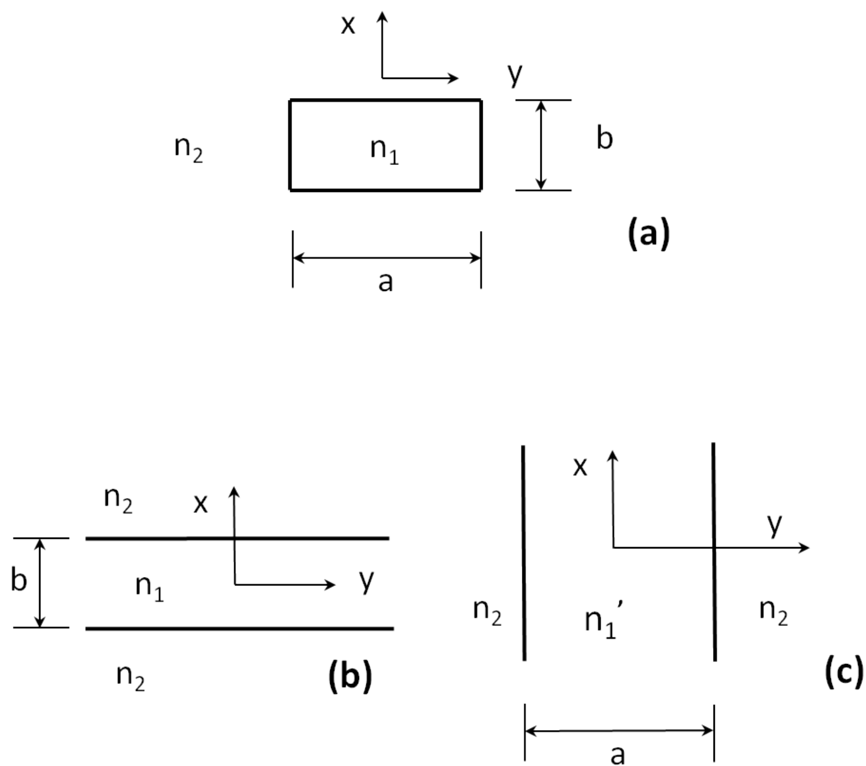

Figure 5.13.The mechanism of the Effective Index Method

Where m is the mode order and Φ_s and Φ_c are the phase shifts referred to the total internal reflection of wave from the film-substrate and film-cover interfaces respectively.

We consider the TE mode (E_y, H_x, and H_z) first. In the horizontal confined slab waveguide, the n_1' satisfies:

$$k_0 b\sqrt{n_1^2 - n_1'^2} = n\pi + 2\arctan\left(\sqrt{\frac{n_1'^2 - n_2^2}{n_1^2 - n_1'^2}}\right) \qquad (5.1.9)$$

$n = 1, 2, 3, ...$

n_1' is the effective index for Fig. 5.13 (b). The root-search technique can be applied to find n_1'. Correspondingly, the dispersion relationship for the TM mode (E_x, H_y, E_z) is

$$k_0 a\frac{n_0}{n_1}\sqrt{n_1^2 - n_1'^2} = m\pi + 2\arctan\sqrt{\frac{2n_2^4 n_1^2 - 2n_1^2 n_1'^2 n_0^2 - n_1'^2 n_1^4 + n_1^4 n_2^2}{n_2^4\left(n_1^2 - n_1'^2\right)}} \qquad (5.1.10)$$

$m = 1, 2, 3, ...$

When we calculate the TE mode for a laterally confined slab waveguide (Fig.5.13 (c)), the TM dispersion relationship should be used because in this case, the E_y component is aligned along the y direction and perpendicular to the waveguide boundaries. The effective index N_{eff} for Fig.5.13 (c) for the TE mode is calculated using the TM dispersion relationship and replacing n_1 instead of n_1'. Taking the 5 μm-width waveguide for example, N_{eff} for the TE mode is 3.48 on substituting the values into the equation. Analogously, N_{eff} for the TM mode is obtained from n_1' from the TM dispersion relationship and consequently substituting it into n_1 in the TE dispersion relationship. The result of N_{eff} for the TM mode is 3.37. The propagation constant β also can be calculated from equation 3.1.25.

The expression of the attenuation constant α can be rewritten by substituting the expression of β. For simplification of the attenuation function, some dimensionless parameters also can be used:

$$x = W\frac{L_c}{d} = L_c k_0 \sqrt{N_{eff}^2 - n_2^2} = 2\pi \frac{L_c}{\lambda}\sqrt{N_{eff}^2 - n_2^2}$$
$$\gamma = \frac{n_2 V}{n_1 W \sqrt{\Delta}} = \frac{\sqrt{2} n_2}{\sqrt{N_{eff}^2 - n_2^2}} \qquad (5.1.11)$$

Thus, the function $f_e(x, \gamma)$ is only related to L_c and $N_{eff.}$ The value of L_c ranges from the order of several nanometers to several tens of nanometers. Accordingly, $\frac{L_c}{\lambda}$ is small when λ is 1550 nm. Based on the data in Table 5.3, the minimum and maximum values of $2\pi L_c/\lambda$ are 0.56 and 0.77 respectively. The function f_e can be plotted with a fixed $L_{c.}$ On the other hand, the value of N_{eff} should be quite close to n_1 as the width of waveguides is larger than 3 µm.

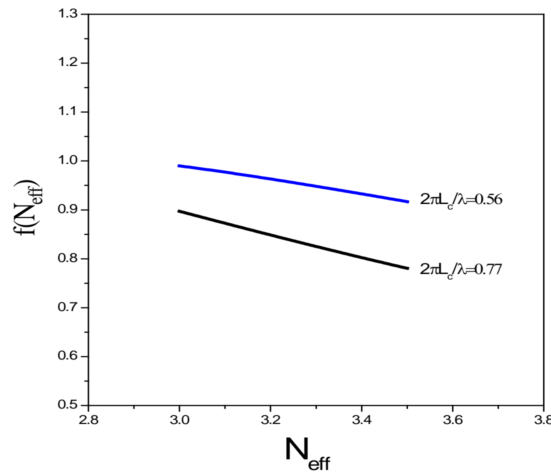

Figure 5.14. Function f with respect to N_{eff} within the range of 3 to 3.5. N_{eff} should be closed to n_1(3.5). The blue line and the black line are within the fixed value of 2πLc/λ. From the AFM results, the maximum and minimum values of Lc is 193 and 139, hence the range of 2πLc/λis from 0.56 to 0.77 with λ = 1550nm.

The loss coefficient α from equation 5.1.1 can be written as:

$$\alpha = \frac{\sqrt{2}k_0\left(n_1^2 - n_2^2\right)}{2n_1} \cdot \frac{\sigma^2\left(n_1^2 - N_{eff}^2\right)}{1 + dk_0\sqrt{N_{eff}^2 - n_2^2}} \cdot f(N_{eff}, L_c) \quad (5.1.12)$$

The first term of this equation is a constant. Here, the range of the function f (N_{eff}, L_{c}) varies within a narrow range between 0.74 and 1 (see Fig. 5.14). The second term is determined by the mean root deviation σ^2, the width of waveguide d and the effective index. With a rather smooth N_{eff} function, the loss is mainly determined more by the surface roughness σ and *d.*

Equation 5.1.12 is also applicable to any rectangular waveguide. For a fixed L_{c}, the scattering loss of a waveguide increases as σ increases. However, the relationship between L_{c} and the loss is complicated. For fixed σ, the loss increases when L_{c} increases until L_{c} roughly equals a quarter of the guided wavelength [81] of 1550 nm light in a waveguide with an effective index(L_{c} is ~110nm in our case). When L_{c} is comparable to the wavelength, the scattering reaches its maximum. In practice, L_{c} is determined by the fabrication process and increases slightly with the roughness decreasing after some smoothing treatments (e.g. oxidation). In this thesis, L_{c} are all larger than a quarter wavelength, thus the change of L_{c} is not a major effect on the loss [71]. In addition, note that when the correlation length tends to infinity, the surface roughness should be zero. Equivalently, when the correlation length tends to zero the surface roughness should be non-resolvable except at very short wavelengths. Thus, the scattering loss should be zero.

	Sidewalls		Bottom surface	
	σ (nm)	Lc(nm)	σ(nm)	Lc(nm)
After 3h oxidation	6	139	10	190
After 9h oxidation	5.9	141	10	193

Table 5.4. Waveguide surface roughness, and L_c measured by AFM

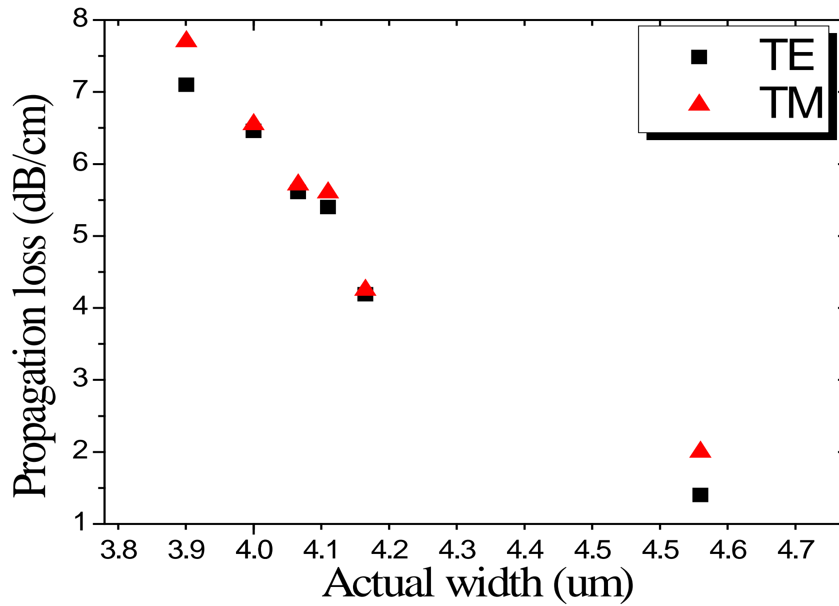

Figure 5.15. the propagation loss is plotted versus actual width measured by SEM.

AFM results reveal that the r.m.s. roughness is reduced slightly after 9-hours of oxidation as shown in Table 5.4. The autocorrelation length also changes slightly. The strip waveguides discussed in this thesis have different surface roughness on their four sides. The top surface and side wall roughness have a similar roughness, which differs significantly from the bottom surface. It is found that the roughness of the top surface and side wall can be reduced slightly by oxidation, whereas the bottom surface

roughness remains stable. This is because further oxidation of the bottom surface, which is in close contact with the silicon substrate, is very hard.

The propagation loss versus actual width of the waveguide is plotted in Fig. 5.15. Considering the roughness is almost constant, the graph indicates that the propagation loss of the waveguides is inversely proportional to the width *d.* The effect for L_c and N_{eff} is minor as the expected from the theoretical analysis.

5.2.4 Strip straight waveguide fabricated with varied proton fluence

According to previous work, we noticed that waveguides fabricated by different fluences of protons exhibit different propagation losses. The propagation loss is derived by Eq. 5.1.2. Two factors included in the equation are affected by the proton fluence: the dimension (*d*) and the r.m.s. roughness σ. For the waveguide shape, the effect of proton fluence is indicated in Chapter 2. Higher fluence produces more defects within the bulk silicon, and the remaining core enlarges after anodization. Moreover, an increased fluence for large area irradiation leads to a decrease of the roughness. This is logical because the fluctuation of the irradiated beam distribution is reduced using a higher fluence.

Fluence (protons/cm^2)	sidewall roughness (nm)	Bottom roughness (nm)	Average roughness (nm)
1×10^{13}	26	30	28
2.5×10^{13}	19	24	22
5×10^{13}	6	10	8

Table 5.5. Sidewall and bottom roughness for different proton fluences. The average roughness is calculated as root mean square of the sidewall and bottom roughness.

Fluence (protons/ cm²)	design width (μm)	Actual width (μm) ±0.01	Actual height (μm) ±0.01	Propagation loss (dB/cm)	
				TE	TM
1×10^{13}	3	3.98	2.00	18.2	19.1
	4	4.10	1.97	13.2	14.6
	5	4.60	1.98	10.7	11.0
2.5×10^{13}	3	3.98	2.00	12.4	13.8
	4	4.10	1.99	9.0	10.1
	5	4.58	1.99	5.8	6.2
5×10^{13}	3	4.00	1.99	6.5	6.6
	4	4.12	1.97	5.6	5.7
	5	4.60	1.98	1.4	1.6

Table 5.6. Summary of propagation loss and dimensions for waveguides fabricated by 3 different fluences

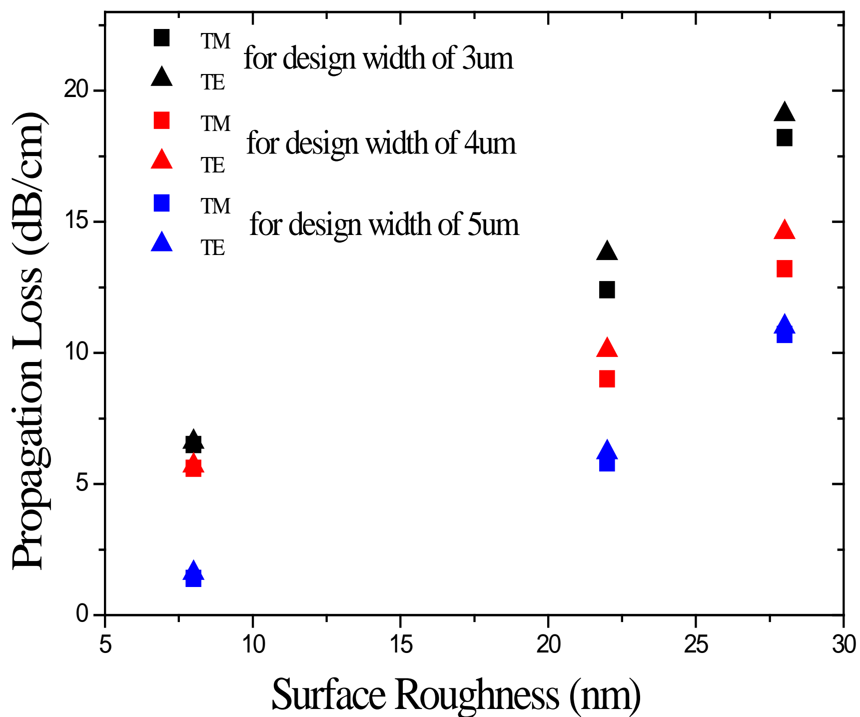

Figure 5.16 Propagation loss versus surface roughness. Propagation losses for design width of 3 μm (black symbols), design width of 4 μm (red symbols), and design width of 5 μm (blue symbols). The ▲ presents the TE polarization and ■ presents the TM polarization.

To reveal the relationship between loss and r.m.s. roughness, three different fluences

of protons were used to fabricate three sets of straight silicon waveguides. In each set, there are three different waveguide widths of 3 μm, 4 μm, and 5 μm respectively.

In this section, we produced three sets of silicon waveguides using fluences of 1×10^{13}, 2.5×10^{13} and 5×10^{13} protons/cm^2. Anodization and oxidation were performed in all cases. We chose these values of fluence because the resulting dimensions of the waveguide cores are similar. Measurements of the dimensions from SEM images support this conclusion. From Table 5.6, with each waveguide width design, the difference of the actual fabricated waveguide dimensions using different fluences are almost at the same level of the experimental errors. AFM results for sidewall and bottom roughness are shown in Table 5.5. The surface roughness is obtained by taking the root mean square average of sidewall and bottom roughness.

The propagation losses of 9 waveguides were characterized by the cut-back method. A scatter chart is drawn as Fig. 5.16 to indicate the relationship between the loss and roughness. The propagation loss of all three groups with the same width has a similar trend. For the purpose of relating the function of roughness to the loss, a curve fitting is performed using the function $y=a+b\cdot x^c$. When c is equal to 2 all fitting lines show good agreement with the experimental data. Therefore, the propagation loss is proportional to σ^2 , which agrees well with equation 5.1.12.

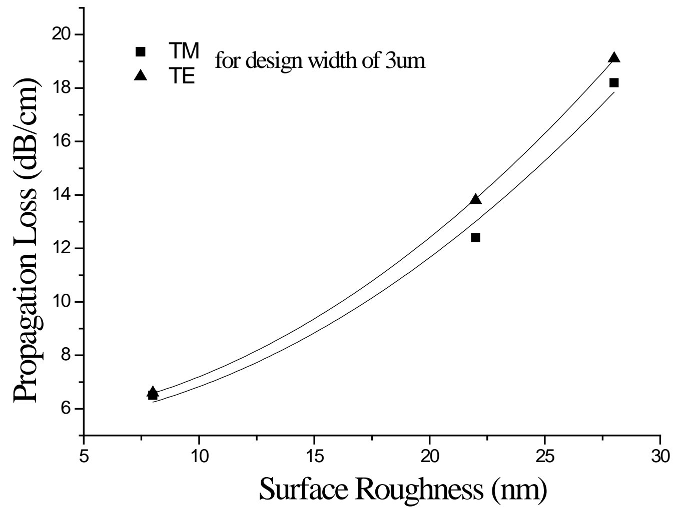

(a)

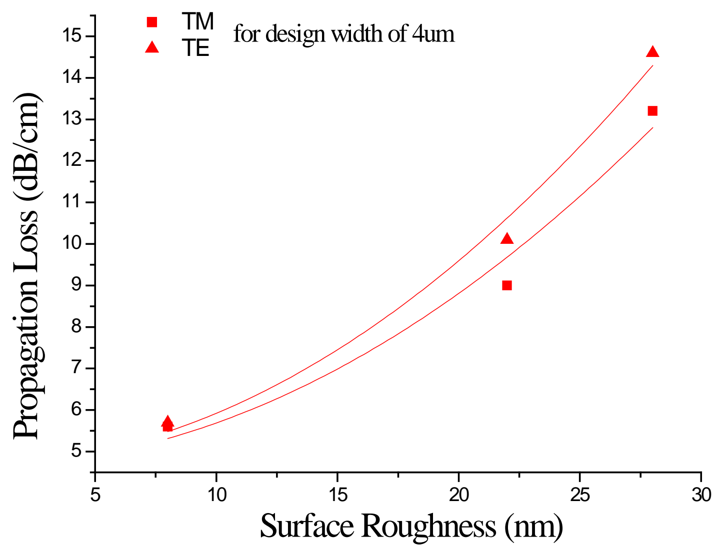

(b)

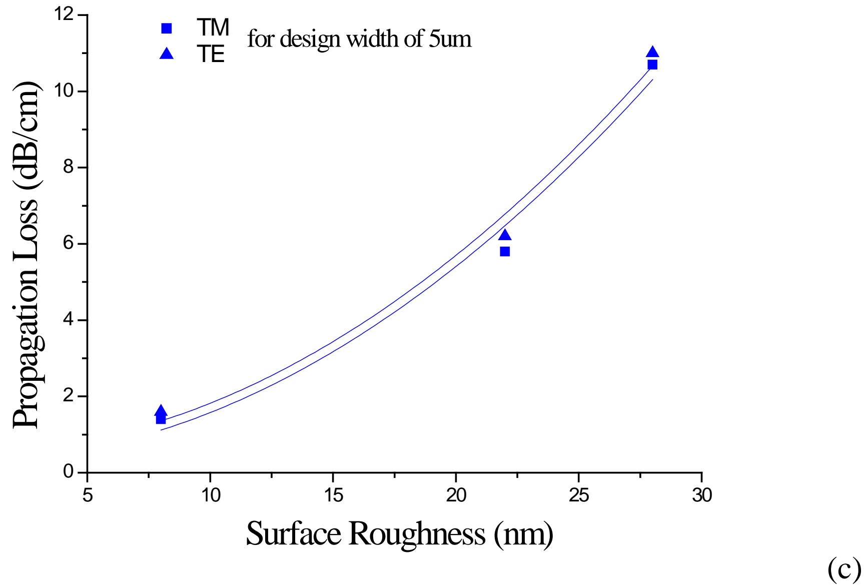

(c)

Figure 5.17. Power lines utilized for fitting the scatter charts. The function used is $y=a+b \cdot x^c$. (a) for design width of 3 μm (b) for design width of 4 μm (c) for design width of 5 μm

5.3 Summary

First, we have demonstrated the ability to directly produce linear features up to 8 mm in length and 1.5 to 3 μm in width using focused proton beam irradiation. With this promising technique, we managed to create long, single-mode silicon waveguide. Secondly, low-loss SOPS waveguides were successfully fabricated by proton beam irradiation. A propagation loss approximately 1 dB/cm can be obtained for both TE and TM polarizations, which is the lowest reported loss for SOPS waveguides.

Other SOPS waveguides were introduced by large area irradiation technique. Such a method enabled mass production. Losses of 1.4 dB/cm and 1.6 dB/cm for the TE and TM polarizations were observed for lowest loss of SOPS waveguides of width 4.6 μm.

In order to reveal the relationship between loss, surface roughness, and the dimensions of the waveguides, the equation for scattering loss of rectangular waveguides was also derived in this chapter. This equation is proved by our experimental data from SOPS waveguides with varying widths and roughness.

Chapter 6

Silicon on oxidized-porous-silicon: three-dimensional and curved waveguides

The large area irradiation technique was further developed for use with different ion fluences, which enables three-dimensional (3-D) integration of waveguides, as shown in chapter 6.1. We also successfully created waveguide bends using large area irradiation. The results for bend losses are presented and discussed in Chapter 6.2.

6.1 Three dimensional integration of waveguides in bulk silicon

Masked proton beam irradiation can be used for three dimensional vertical stacking of waveguides. Ion irradiation can prevent the HF chemical etching of irradiated regions, which remain as silicon islands surrounded by porous silicon. The thickness of the overlying silicon layer can be controlled by the well-defined ion range. The rate of chemical etching slows down along the path of the ion beam and is totally stopped at the end of range. Therefore, etching still proceeds in the near surface area of the irradiated region. In simple terms, this method of fabricating 3D stacked waveguides

employs different ion energies for irradiation through the designed mask. For further calculation and modeling, the ion damage profile and the schematic of holes current transport are used as the same way in the previous chapters. The stopping and range of ions in materials was found using SRIM for 250 keV protons. During proton irradiation the ions penetrate into the bulk p-type silicon substrate, the energy of the ion beam decreases gradually until the end of range, and Frenkel defects are generated along the ion track. For the first 2.5 μm, the damage is low and constant, but it increases promptly by a factor of 10 times at the end of range. Such defects induce trap levels within the energy band gap in the doped silicon, which reduce the charge carrier concentration and so increase the resistivity. MEDICI simulations show a distribution of a net positive charge at the irradiated area with a lateral electrical field (Fig. 2.7). Here, hole current is deflected from the irradiated path and this effect becomes stronger with higher fluence. When the sample undergoes electrochemical etching in a HF solution, a positive electrical voltage is also applied on the sample to create an external electrical field. This forces the holes to flow perpendicularly to the surface in the unirradiated regions, but they are deflected away from the irradiated regions. Thus, current flow is much lower in the irradiated regions. When the damage is high enough, etching results in high and low defects regions respectively. By appropriately reducing the fluence, the low defect regions can be totally etched away and only high defect regions remain as a silicon core. This is the mechanism of the formation of a buried silicon waveguide at the end of range.

6.1.1 The first test for a fluence of protons

Before the fabrication of actual devices, the relationship between the fluence of protons and the resulting defect density in the silicon sample was investigated. Direct proton beam irradiation was conducted within a fluence range of $1\times10^{15}/cm^2$ and $5\times10^{13}/cm^2$. The energy of the focused proton beam is 250 keV.

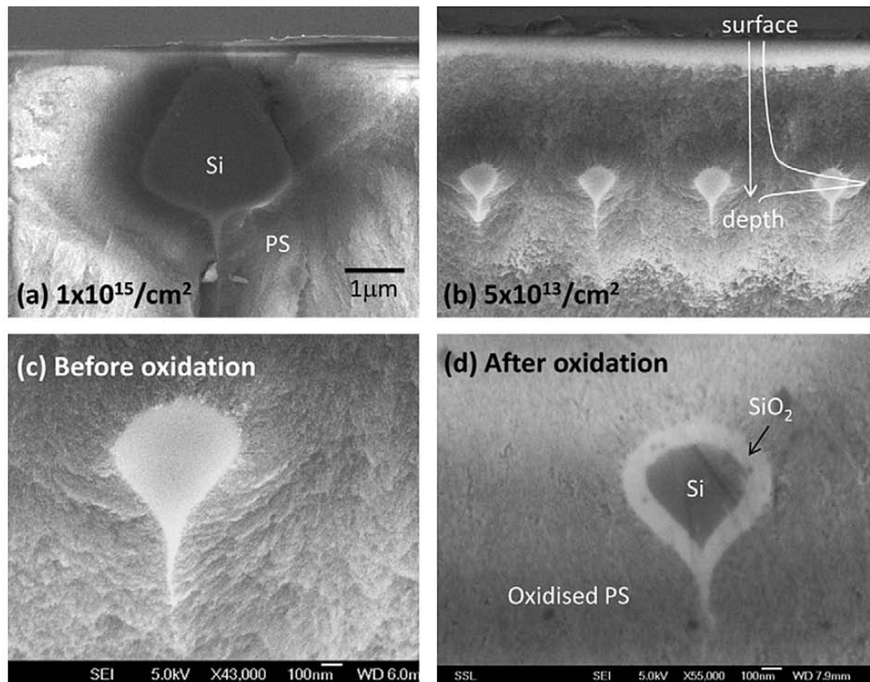

Figure 6.1. (a and b) Shows cross sectional view of a silicon core irradiated with (a) $1\times10^{15}/cm^2$ and (b) $5\times10^{13}/cm^2$. (c) Close-up of a single core before oxidation (d) and after oxidation.

Cross-sectional SEM images of lines irradiated in *p*-type silicon of 0.5 Ω.cm are shown in Fig. 6.1. Comparing high and low fluence irradiation, it is obvious that the silicon core embedded in porous silicon is larger with higher fluence. The fact that the Si core reaches the surface confirms that the etching process is terminated at the low defect region. Nevertheless, in Fig. 6.1 (b) a sub-micron spherical waveguide at the

end of range of 2.5 μm is observed at a lower fluence. A magnified image in Fig. 6.1 (c) indicates that the diameter of the core is about 500 nm, with a cusp spread from one point beneath the surface. After oxidation in ambient air for about 3 hours at 1000 °C, the 9 μm thick porous silicon surrounding layer becomes completely oxidized. It is noteworthy that only a thin (40 nm) thermal oxide is formed around the silicon core from Fig. 6.1 (d).

The reason for this is the much higher rate of oxidation for porous silicon compared to silicon, caused by its high surface area/volume ratio. The size of the silicon core is reduced symmetrically. Furthermore, this process can also reduce the surface roughness on all sides of the waveguide, which consequently improves the propagation loss as discussed in previous chapters.

6.1.2 Two layers of waveguide in a single silicon chip

Using the end-of-range damage, we can use this technique to build up a pattern of three-dimensional nanostructures in bulk silicon. Fig.6.2 (a) shows a schematic diagram of the irradiation procedure. Firstly, the silicon substrate is coated with a patterned photo-resist. Then, a large area proton beam with an energy 650 keV is used for irradiation through this patterned photo-resist. Thus the energy is reduced to the required level by using a proper thickness of the photo-resist in the area underneath the mask. After that, electrochemical etching is conducted to produce porous silicon cladding. After these steps, two different layers of waveguides are created as the SEM

images show in Fig.6.2 (b) and (c). The stopping range of unmasked regions for 650 keV protons is 9 μm. As calculated, protons with such an energy can penetrate the 7 μm thick photo-resist, while the end of range is decreased to 3.5 μm below the silicon surface. For the final waveguide, the size of the silicon core is determined by the irradiated fluence of the ion beam, while the depth is determined by the resist sidewall slope and width.

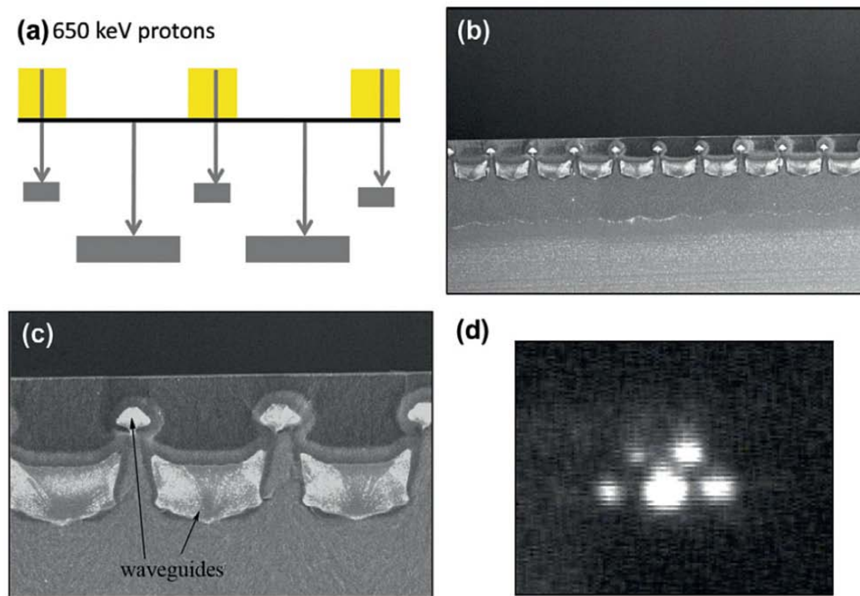

Figure 6.2. 2-level system formed by single energy irradiation through a mask (d). Corresponding output image by simultaneously coupling light into all the waveguides.

A further application based on the above fabrication consisting of three layers of waveguides has been built up, shown in Fig.6.3. In this case, we conducted another irradiation after 650 keV protons by using a 300 keV helium beam. Within this lower energy, the ions are not able to pass through the 7 μm photo-resist, and are stopped by the mask. The end of ion range at the unmasked regions is 1.3 μm below the surface. The SEM image shows a cross-section of three different layers. Therefore, we can produce one bottom and middle level of waveguides by high energy ion beams, with

one top level waveguide by low energy ion beams, in a single silicon chip. Fig.6.2 (d) and 6.3(d) show the corresponding output image for laser coupling of the two and three level system. During the optical test, the input laser beam is defocused so that the vertically stacked waveguides can be coupled at the same time. Although a small core Si under photo-resist is very clear to see in the three level system, there is no obvious light signal observed from the middle region in this system. The probable reason is that the size of the core is too small and the propagation loss is high.

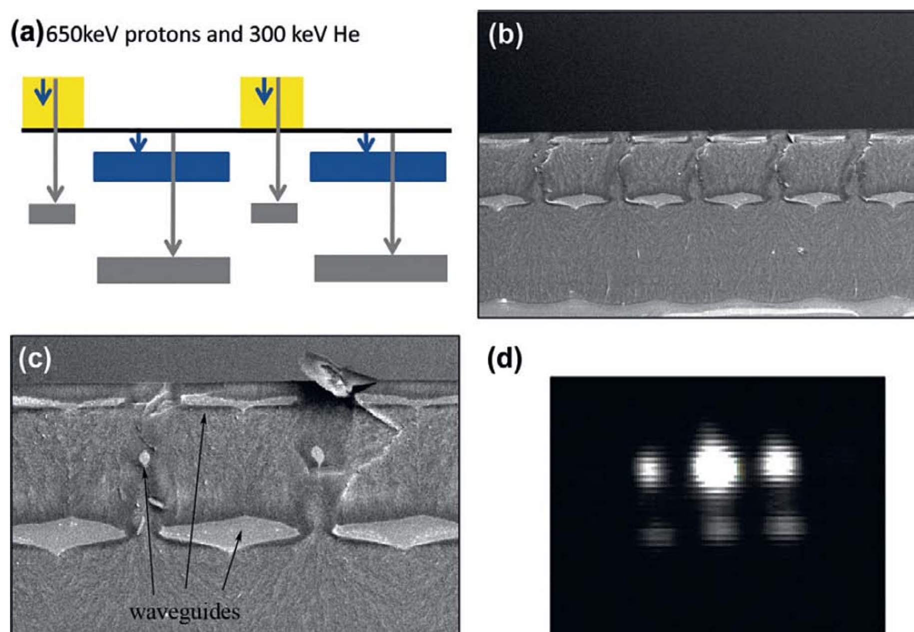

Figure 6.3. 3-Level system formed by double energy irradiation through a mask (d). Shows the corresponding output image by simultaneously coupling light into all the waveguides

We believe that by using this technique more levels of waveguides can be also achieved in the future. Further optimization of the core profile can be achieved by improving the quality of the photo-resist mask. During the entire fabrication, there is only one step of photolithography and etching, which shows great potential for the fabrication of photonic crystals in the same manner. Our 3D waveguide circuit may

function as a via structure which can guide waves between different levels.

6.2 Waveguide bends

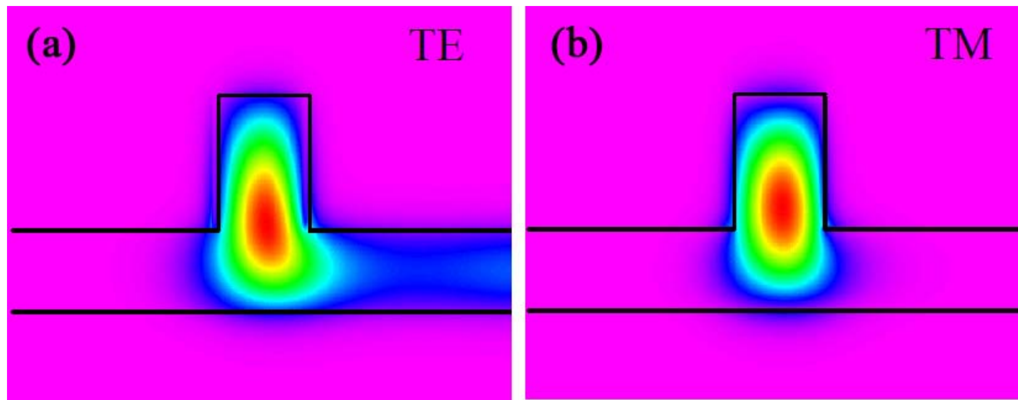

Figure 6.4 Cross-sectional image of a modeled waveguide bend demonstrating the polarization dependence on slab leakage due to the bend radius (R=50□ μm). The (a) TM mode demonstrates little slab leakage whilst the (b) TE mode demonstrates a large amount of leakage. From [82]

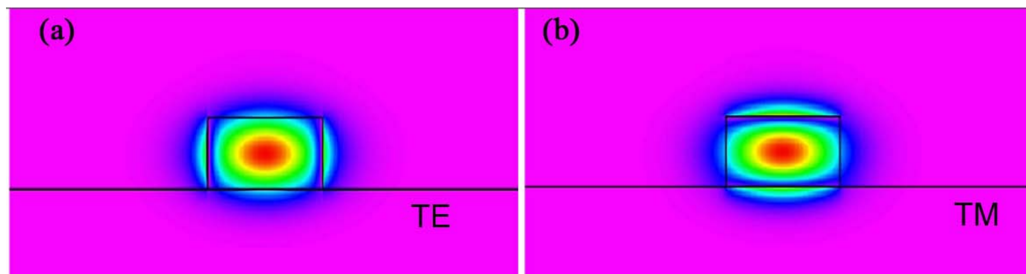

Figure 6.5 Simulation is done by Beam Prop^{TM} for waveguide with the TE polarization (a) and the TM polarization (b) in a waveguide bend (R=50 μm). Waveguides have the same cross-sectional dimensions as 4.5 μm width and 2 μm height.

In real optical circuits, the path of the light is usually curved or bent rather than travelling in a straight line. Such a task relies on the design of waveguide bends. In such a case, when light travel through the bend, the energy tends to radiate into the air. The radiation loss of the curved waveguides depends on its geometric parameters, especially the radius. The smaller the curvature radius, the greater the radiation loss.

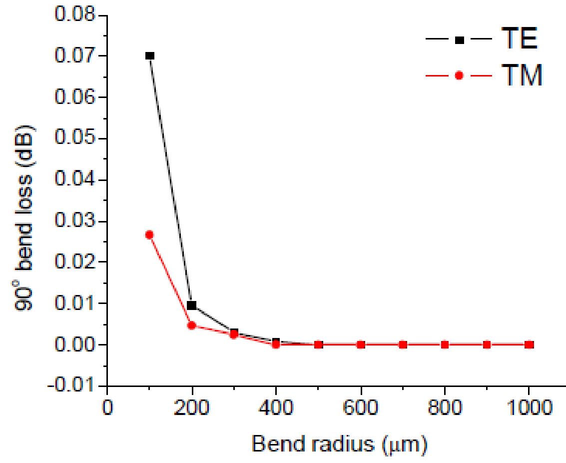

Figure 6.6. Modeled Loss of a 90º waveguide bend as a function of bend radius (modeled by A. Liu of the Intel Corporation). From [82]

The loss coefficient from the bend is satisfied [83]:

$$\alpha_{bend} = C_1 \exp(-C_2 R) \qquad (6.2.1),$$

where R is the bend radius, C_1 and C_2 are related to the waveguide structures and mode properties. Here we take rib waveguides as a benchmark, which is a traditional type of bends with mature techniques of fabrication. SIMOX wafers were used to construct the rib waveguides, formed by implanting oxygen ions at 200 keV into *p*-type (100) silicon wafers. The single mode bending waveguide can be formed with this technique to achieve a lowest bend loss of 1.54 dB/cm for the TE mode and 1.8 dB/cm for the TM mode at a radius of 7.67 μm for a wavelength of 1550 nm [11]. Simulation for the rib waveguide bend is modeled by the BeamProp™ Software. The distribution of single mode is demonstrated in two polarization. The energy leakage of the waveguide bend under the TE polarization is higher than that of the TM polarization (R = 50 μm), indicating that the loss is polarization dependent (Fig. 6.4)[82]. A similar simulation was also conducted for a strip-based waveguide bend

under the same conditions (Fig. 6.5), which is multi-mode. Figure 6.5 shows the mode distribution for both polarizations, which appears to be similar. Optical confinement is obviously enhanced in the strip waveguide bend compared to the rib one. BeamProp^{TM} can also be used to model the bend loss of the 90 degree rib waveguide bends using the effective bend method. This study was done by Intel and the results are shown in Fig. 6.6. It is shown that the bend loss is below 0.1 dB for a radius ranging from 200 μm to 1000 μm. However, the bend loss increases rapidly when the bend radius is smaller than 100 μm. The purpose of our work is to develop sharp bending waveguides with low energy leakage, which fills a gap in silicon photonic circuits research.

6.2.1 C-bend waveguides

We first have investigated C-bend waveguides connecting 5 μm-width straight waveguides. This is because the experimental result for propagation loss of 5μm-width straight waveguides is good and can be readily used in our test set-up. Six bends with identical radii were used to connect these sections into one waveguide structure. The purpose of the aforementioned design is to formulate a precise characterization, which will be elaborated upon later. Here, tight C-bend structures are applied, with the smallest radius down to 44 μm. Large area irradiation methods are used for manufacturing. Therefore the cross-section of the C-bend waveguides is rectangular-like, which is polarization independent. To study the effect of different

bend radii on the loss, the radii of C-bend waveguides are chosen in a series from 80,70,60,50,49,48,47,46,45,44 μm.

6.2.1.1 Cut-back method modified for C-bend waveguides

This characterization method is based on the cut-back technique. The proposed C-bend waveguide structure is equivalent to the combination of one straight waveguide and 6 bends. For the straight part, the propagation loss α_1 can be measured from a straight waveguide with an equivalent cross-section, which can be deduced from the total loss in order to calculate the loss in the bending area. To obtain the loss data, the entire C-bend waveguide structure was polished six times at the point of the cross marks in Fig. 6.7, from right to left consecutively. After each polish, the remainder of the waveguide structure was coupled under the same condition and the output power (P_1, P_2, P_3, P_4, P_5, P_6) in each case was recorded. The length l_1, l_2, l_3 shown as Fig.6.7 was also measured after each polish.

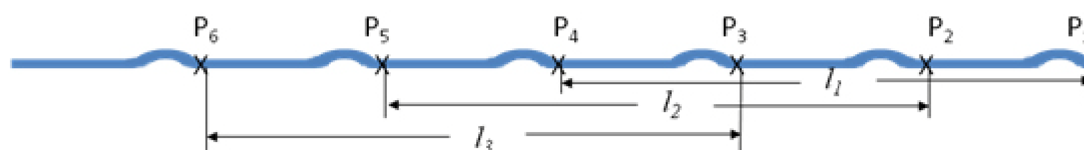

Figure 6.7. Schematic for modeled cut-back method for measuring the bend loss for C-bend waveguides.

According to the definition of attenuation (Eq. 3.2.2), these three equations can be easily derived. Bend loss Δ presents the loss associated with each bend. The unit of Δ is dB/bend.

$$10\log\frac{p_1}{p_4} = l_1\alpha_1 + 3\Delta,$$
$$10\log\frac{p_2}{p_5} = l_2\alpha_1 + 3\Delta, \qquad (6.2.1)$$
$$10\log\frac{p_3}{p_6} = l_2\alpha_1 + 3\Delta$$

where α_1 is the propagation loss of the straight waveguide with the same cross-section, which is 1.4 and 1.6 dB/cm in the TE and TM polarization.

Thus, Δ is the bend loss, which is calculated by a combination of the above equations.

$$\Delta = \frac{1}{9}\left(10\log\frac{p_1 p_2 p_3}{p_4 p_5 p_6} - \alpha_1\left(l_1 + l_2 + l_3\right)\right) \qquad (6.2.2)$$

6.2.1.2 Scattered light method modified for C-bend waveguides

From Chapter 3.2.2.2, a propagation loss α can be characterized for a C-bend waveguide by the scattered light method. An expression of Δ can be written as:

$$\alpha \cdot l = 6\Delta + \alpha_1 \cdot l' \qquad (6.2.3)$$

where l' is the length of the straight part. Consequently, the bend loss Δ is computed from Eq. 6.2.3.

6.2.1.3 Experimental results

The resultant structures are shown in Fig. 6.8. The C-bend losses, which are computed by both above mentioned methods, with various radii are listed in Table 6.1. When the bending radius increases, the bend losses decrease, as expected. The bend loss increases sharply when the radii are smaller than or equal to 49 μm. However, when

the radii are even smaller than 48 μm, no output power can be detected. Hence no bend loss can be measured for bends with radii of 44 to 47 μm. The difference of the bend loss between TE and TM polarizations is not significant, which proves that such waveguides are polarization independent.

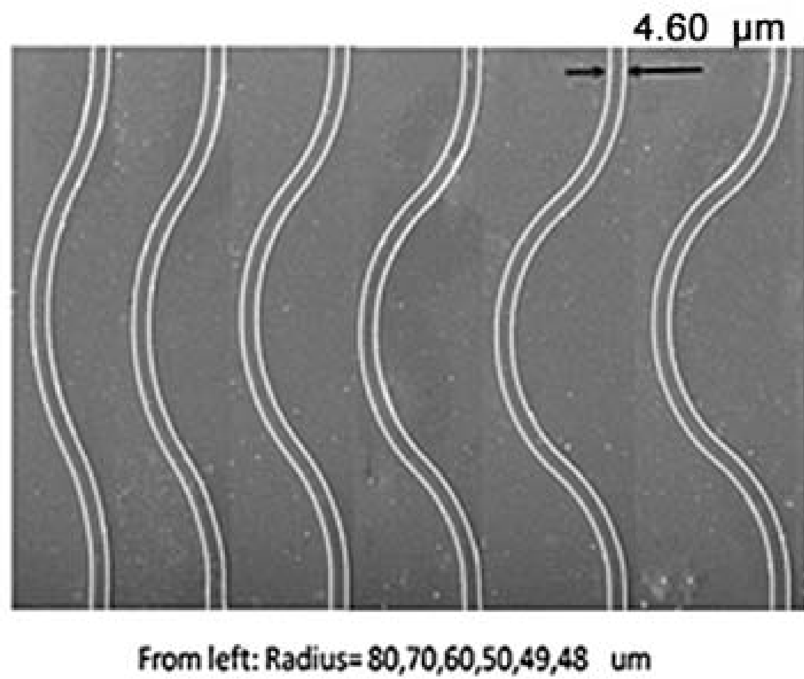

Figure 6.8. Top view of varied C-bend waveguide by SEM.

Radius (μm)	bend loss (dB/bend) from the cut-back method		bend loss (dB/bend) from the scattered loss method	
	TE	TM	TE	TM
80	1.64	1.28	0.67	0.70
60	2.02	2.36	1.63	1.58
70	2.26	2.19	1.49	1.49
50	3.07	2.78	2.20	2.43
49	3.32	3.48	2.74	2.72
48	3.50	3.7	3.01	3.16

Table 6.1. Summary of bend loss for varied-radius C-bend waveguides.

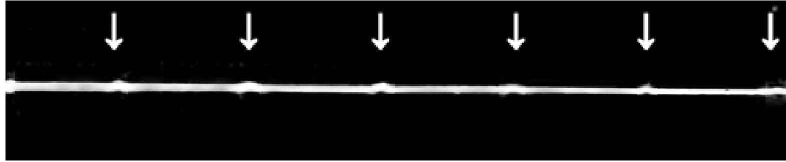

Figure 6.9. Scattered image of a C-bend waveguide with radius of 60 um. The white arrows indicate the C-bends.

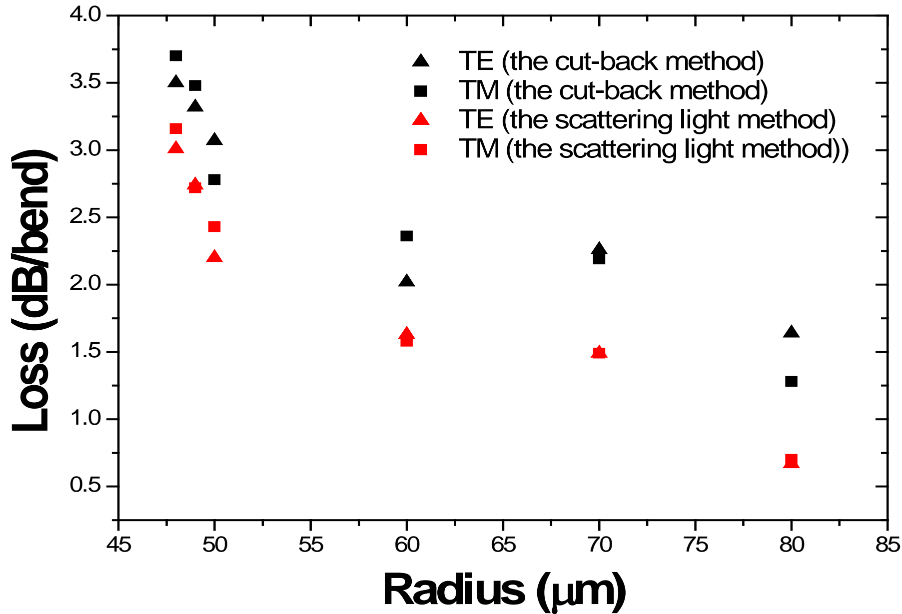

Figure 6.10. Bend loss versus radius of bend

We also used the scattered method to characterize the bend loss. A broad band laser source (1530~1569 nm) is used to achieve higher intensity for the scattered light. For each C-bend waveguide, the measured loss is lower when we used the scattered light method. It makes sense since a wave with a single wavelength component suffers from more propagation loss than with multiple wavelength components. The accuracy of the scattered method is lower than the cut-back method [5], however, in Fig. 6.10 it is obvious that the trend of the curve is similar. For the 80 μm-radius-bend waveguide,

the bend loss shows a lowest loss of 1.28 and 1.64 dB/bend for TE and TM polarizations, respectively.

It is worth noting that every C-bend joins the straight part by a tiny gentle curvature rather than connecting directly. The length of the joining part is between 15 μm and 30 μm, which is negligible compared to the circumference of the C-bend. From scattered-light images, the energy intensity within the joining part between C-bends and straight waveguides grows rapidly, for instance, in Fig.6.9. Therefore, the cut-back method gives more reliable results than the scattered loss method.

6.2.2 90 degree bending waveguides

The most appropriate method for fabricating bending waveguides is large area irradiation, which can be implemented to simultaneously produce a group of bending waveguides. Usually, an array of bending waveguides with varying radius and number of bends is produced in the layout using large area irradiation. In the case discussed subsequently, we focus on investigating the loss of waveguides with 90º bends. (The width of these bends is 5 μm and the reason has been mentioned in Chapter 6.2.1.) For this purpose, five waveguides are fabricated on one chip, with different number of bends but the same bend radius. Starting with the right waveguide with only one 90º bend, each subsequent waveguide has one more 90º bend than the previous one (see Fig. 6.11). Thus, the waveguide on the left of the group has a total of five 90º bends. The output power in each waveguide can be measured and plotted as a function of the

number of bends. The slope of the plotted curve, therefore, determines the amount of power loss per bend. Extra insertion losses can be removed by using the loss data of straight waveguides with same width, height, and length presented in the example. The assumption to use this method, however, is that the propagation loss caused at the joint of the straight and the bending waveguide is negligible. Such an assumption is reasonable in this study, since we only focus on low-radius bending waveguide fabrication via masked proton beam irradiation. The range of radii under investigation is from 45 μm to 200 μm.

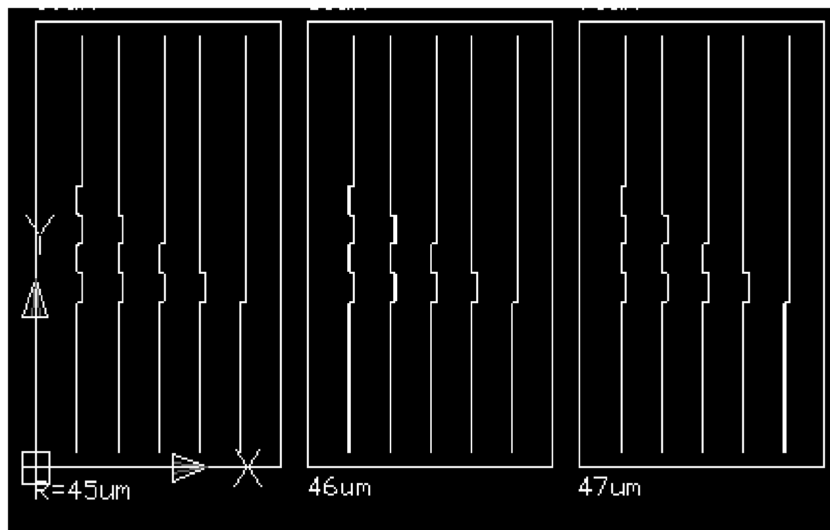

Figure 6.11 The CAD layout for designing the 90 degree bends. The same radius bending waveguides are organized in one block. After fabrication process, one block is produced in one silicon sample.

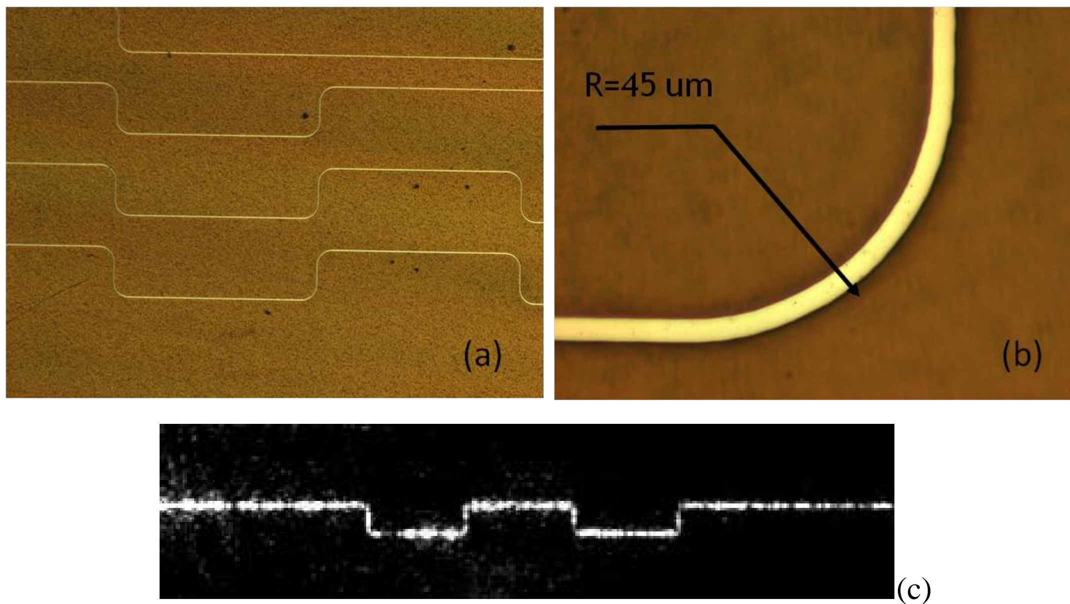

Figure 6.12. (a) Low magnification optical micrograph of an array of 45 μm-radius 90 degree bends (b) High magnification optical micrograph for 45 μm-radius 90 degree bends (c) Scattered light of 45 μm-radius 90 degree bends taken by the infrared camera.

The fabricated chip is shown in Fig. 6.11. Every five waveguides with the same bend radius is grouped together. Pre-treatment including cleaving and polishing was performed before the measurement, so that within each group of waveguides, the length of the waveguides is equal and the facets are similar. The details of the waveguide structures are shown in Fig. 6.12(a-b). The laser transmitted in the waveguide with 45 μm radius bends are imaged by an infrared camera, shown in Fig. 6.12(c).

Coupling should be optimized for each waveguide. After optimizing the coupling, the output power (dB) is recorded for 5 waveguides. The bend loss for the 150 μm radius bends is plotted as a chart in Fig. 6.11 and the slope for the fitting line presents the bend loss (dB/bend). Other groups of waveguides also are characterized using this

method and results are summarized in Table 6.2. While the bend radius reduces from 100 μm to 45 μm, the bend loss increases as expected. When the radius is above 100 μm, the bend loss remains stable (Fig. 6.14). Intriguingly, the bend loss for a 200 μm bend radius is a little larger than those with 150 μm radius. The reason is that with large radius bends, the propagation loss over the length is 1.6 dB/cm and 1.4 dB/cm for TE and TM polarizations, respectively. Such a loss effect is obviously more significant in a 200 μm-bend waveguide and dominates over the radiation loss caused by bending. The optimal solution emerges when the bend radius is around 150 μm radius, which is approximately 1.3 dB/bend.

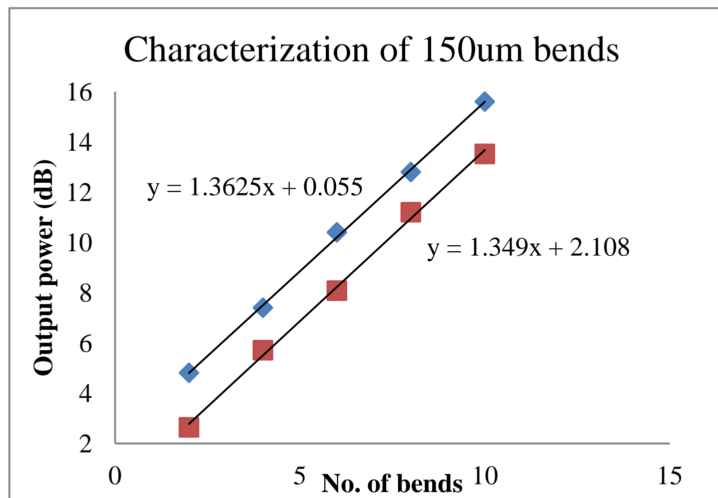

Figure 6.13. The measured bend loss. The slop of the linear lines is the loss per bend, which are 1.35dB/bend and 1.36 dB/bend for the TE and TM polarizations.

Bend Radius (μm)		45	50	60	70	80	90	100	125	150	200
Bend Loss (dB/bend)	TE	4.81	4.22	3.69	2.93	2.71	2.14	1.64	1.41	1.35	1.37
	TM	5.23	4.32	3.34	2.85	2.63	2.33	1.58	1.32	1.36	1.41

Table 6.2. Summarization of bend loss for varied-radius 90° bend waveguides.

The phase shift of the optical wave transmitted in bending waveguides is larger along the outer edge than the inner edge. Consequently, a radiation mode will be generated when the bend radius is small. When the radius becomes smaller, the interaction of the mismatched modes between the straight part and the bending part is enhanced, and so is the effect of the sidewall surface roughness. This leads to an increase of the reflection and loss. Marcatili *et. al*. employed a complex eigenvalue equation to solve the bend loss [84]. The radiation loss, showing an exponential dependence on the bend radius *R*, can be described as

$\alpha = K \cdot \exp(-cR)$, (6.2.4)

where $c = \beta(2\Delta N_{eff} / N_{eff})^{3/2}$, and *K* depends on the refractive indices of the cladding and waveguide core as well as the waveguide height, and β is the modal propagation constant. ΔN_{eff} is the difference between the modal effective index N_{eff} and the cladding index. Here, this effective index is not just the material property, but depends on the whole waveguide design. The value can be obtained by numerical mode calculation which has been discussed in Chapter 5.2.3.2. The tendency of the 90 degree bend loss is in accordance with the theoretical formula. The surface roughness is a factor affecting bend loss was discussed by Vlasov *et. al.* and Lim Chin Song [85, 86]. The sidewall and bottom root-mean-square roughness σ measured in previous chapters are 7 and 10 nm. The difference between the two values is not substantial so that we cannot observe apparent polarization dependence from our results.

An exponential function can be used in the curve fitting of the bend loss results (see Fig. 6.15). Simulations were performed in Origin® [87] and the coefficient *c* was calculated, which is 1/34.16 for the TE polarization, 1/28.253 for the TM polarization. Consequently, the value of the effective index was calculated as 3.422 and 3.349 for the TE and TM polarization. These simulation results are quite close to the theoretical calculation for the equal cross-section straight waveguide, which is 3.48 and 3.37 for the TE and TM polarization calculated in chapter 5.2.1.

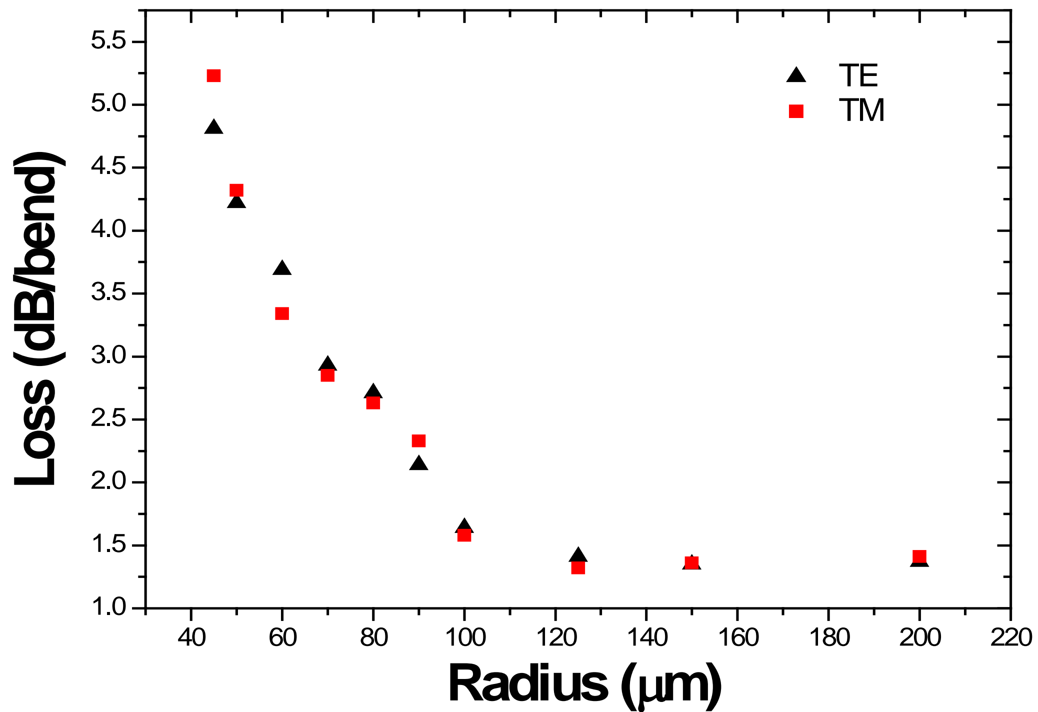

Figure 6.14. Bend loss versus radius of 90° bends.

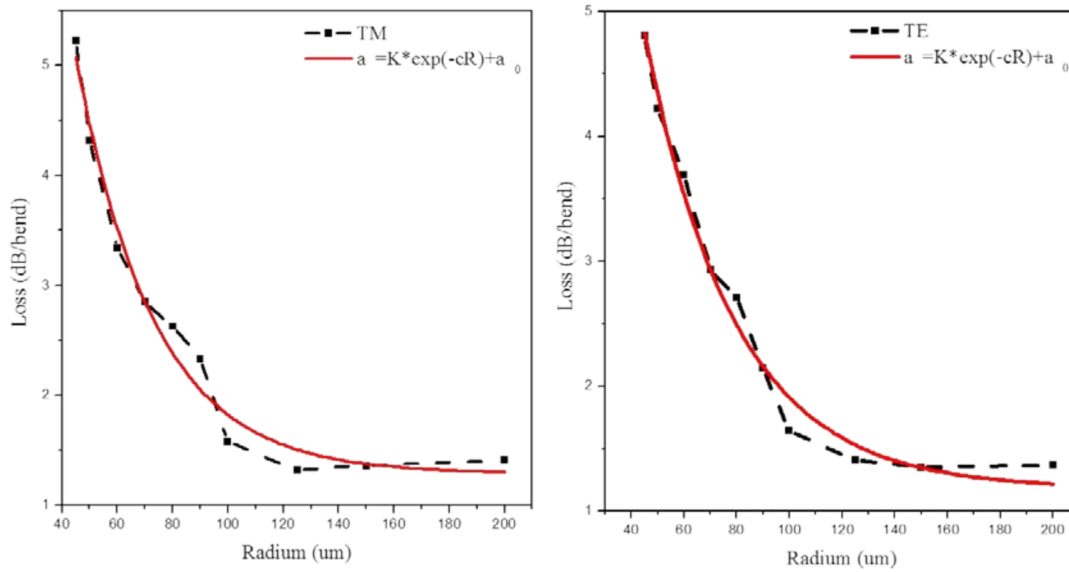

Figure 6.15. simulation for the bend loss versus radius. The function used was $\alpha = K \cdot \exp(-cR) + a$ **[84].**

5.3 Summary

In this chapter, we have demonstrated that the large area ion beam irradiation method can be used to fabricate complex waveguide structures. The first application of the large area irradiation is to create vertically stacked 2 and 3 level waveguides systems using one or two proton energies for irradiation through a mask. The separation of different levels can be independently controlled by the thickness of the mask or the energy of the incident beam. Furthermore, the waveguide bends including C-bend waveguides and 90° bending waveguides were successfully fabricated by large area irradiation coupled with patterned photo-resist masks. The bend loss of our waveguide bends was studied theoretically and experimentally. For C-bend waveguides, the lowest loss occurs when the bend radius is 80 μm, which is 1.28 and 1.64 dB/bend for

the TE and TM polarization. For 90° bending waveguides, the lowest loss is approximately 1.3 dB/bend to1.4 dB/bend when the bend radius is around 125 μm.

Chapter 7

Bragg cladding waveguides

This chapter presents a scheme to fabricate single mode Bragg cladding rib waveguides. The fundamentals of distributed Bragg reflectors and Bragg cladding waveguides are first introduced. The fabrication procedure is then described and the experimental and simulation results are discussed in chapter 7.3.

7.1 Background of Bragg reflectors

A Bragg reflector or Bragg mirror is a structure formed from multiple layers of alternating materials with varying refractive index, resulting in periodic variation in the effective refractive index in the structure. A Bragg reflection waveguide enables light to be transmitted in a lower refractive index core which is confined by a photonic band gap rather than total reflection. For incident waves whose wavelength are close to four times the optical thickness of the layers, many reflections will be combined with constructive interference, and the layers act as a high-quality reflector. The first Bragg cladding planar waveguide was proposed in 1976 by Yeh and Yariv [88]. They used a Bloch wave formulation of propagation in layered media to obtain the dispersion relation of a Bragg waveguide. These results presented the possibility of using Bragg reflection to obtain lossless confined transmission in slabs with a lower

dielectric constant than that of the surrounding media. After this milestone, light propagation in the Bragg waveguides was first observed in 1977 by Cho *et. al.* [89]. Another specific structure is optic fibers that confine light to a low index core by virtue of a periodic glass cladding. This was firstly analyzed in 1978 [90] and then improved by Fink *et. al.* and Winn *et. al.*[91, 92]. Unlike ordinary Bragg mirrors, omnidirectional reflectors are a kind of photonic crystal that can be a perfect mirror for light from any angle of incidence, with any polarization, within a specified frequency range known as a stop band. The omniguide is composed of a low index core surrounded by an omnidirectional mirror that improves the confinement of electromagnetic modes. Fink *et. al.* extended their previous work and created a realizable structure for omnidirectional reflection, which was simply constructed by a group of nine alternating dielectric layers of polystyrene and tellurium. The derivation of the stop band of frequency is based on the Bloch wave function. For any given incidence angle θ_0, the approximate width in frequency is

$$\Delta\omega(\theta_0) = \frac{2c}{h_1\sqrt{n_1^2 - n_0^2\sin^2\theta_0} + h_2\sqrt{n_2^2 - n_0^2\sin^2\theta_0}} \times \left[\cos^{-1}\left(-\sqrt{\frac{\Lambda-1}{\Lambda+1}}\right) - \cos^{-1}\left(\sqrt{\frac{\Lambda-1}{\Lambda+1}}\right)\right]$$

(7.1.1)

The range to midrange can be expressed as

$$\omega_h = \frac{2c}{h_2 n_2 + h_1 n_1}\cos^{-1}\left(-\left|\frac{n_1 - n_2}{n_1 + n_2}\right|\right) \quad (7.1.2)$$

$$\omega_l = \frac{2c}{h_2\sqrt{n_2^2 - n_0^2} + h_1\sqrt{n_1^2 - n_0^2}} \quad (7.1.3)$$

$$\frac{1+\Lambda}{2}\cos\left(k_x^{(1)}h_1+k_x^{(2)}h_2\right)+\frac{1-\Lambda}{2}\cos\left(k_x^{(1)}h_1-k_x^{(2)}h_2\right)+1=0, \quad (7.1.4))$$

$$where, k_x^{(\alpha)} \equiv \sqrt{(\omega n_\alpha / c)^2-k_y^2} \ (\alpha=1,2)$$

$$\Lambda \equiv \frac{1}{2}\left(\frac{k_x^{(2)}}{k_x^{(1)}}+\frac{k_x^{(1)}}{k_x^{(2)}}\right)TE, \frac{1}{2}\left(\frac{n_1^2 k_x^{(2)}}{n_2^2 k_x^{(1)}}+\frac{n_2^2 k_x^{(1)}}{n_2^2 k_x^{(2)}}\right)TM \quad (7.1.5)$$

The calculations from the above equations are in good agreement with experimental data [91]. In parallel, it is reported in Winn's work [92] that a necessary condition of a specific range of frequencies for such omnidirectional reflection is the assumption that the crystal exhibits a complete three-dimensional photonic bandgap, and that no propagating solutions of Maxwell's equations can be found. A general criterion for this behavior is derived that it does not require materials with very large indices. The index ratio should be reasonably high (>1.5) and the indices themselves somewhat higher (>1.5) than those of the ambient medium. The results of the above numerical analysis pave the way for further research and make it possible to produce a stack of multi-layers within appropriate indices experimentally, that is, omnidirectional reflectors. Another example of omniguides is an all-dielectric coaxial waveguide, which has a radially symmetric electric field distribution so that the polarization is stable during transmission [93]. In addition, the mode has a point of zero dispersion which can be placed in the single-mode frequency window. This kind of coaxial omniguide can also be used to confine light around sharp bends since the light is guided by Bragg reflection rather than by total internal reflection. This structure is difficult to create on a silicon-based chip. However, when the same principle of using

one-dimensional omnidirectional reflectors was applied, Bragg waveguides in silicon were successfully fabricated by depositing multilayers of alternating Si and Si_3N_4 layers using current microelectronics technology processes (CMOS compatible processes) [94]. It was the first report on the fabrication of the Bragg waveguides in silicon photonics although it employed multiple processes of depositing alternating materials. Therefore other groups tried to explore other schemes to produce multiple layers within different refractive indices more efficiently in recent years. Porous silicon is a suitable choice for fabricating an omnidirectional mirror combined with multi-layers of porous silicon since it is easy to control the refractive index and easy to create on a silicon wafer. [44]. Xifré-Pérez *et. al.* proposed and analyzed the structure which is an all-porous silicon multilayer consisting of a core layer inserted between two symmetric omnidirectional mirrors [95]. In their work, the influence of the parameters including the layer thickness, number of periods of the omnidirectional mirror, the refractive index and thickness of the core layer on the guided modes was analyzed using the transfer matrix method [96]. This work also made a comparison between omnidirectional mirrors and distributed Bragg reflectors, and the result showed the former cladding offered a higher confinement for a certain number of modes even with a small core thickness. In this chapter, we aim to apply this theoretical analysis as a basis for developing a fabrication method for the experimental experimental realization of such a structure.

7.3 Fabrication of Bragg waveguides

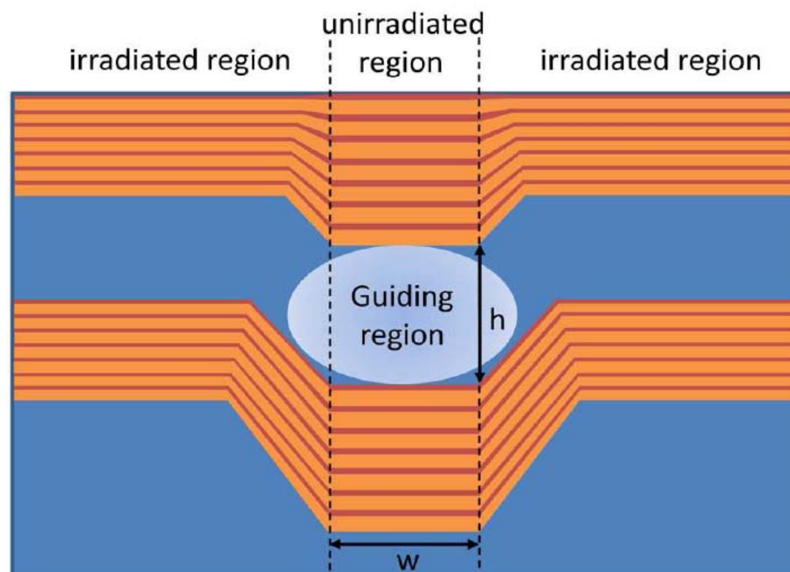

Figure 7.1. Schematic diagram of the fabrication process

The fabrication of an omnidirectional waveguide on a silicon substrate is based on manufacturing porous silicon multilayers [56, 97]. The two irradiated regions are written with a focused proton beam of 2 MeV protons to irradiate a silicon sample with a resistivity of 0.02 Ω.cm. Two lines are written by proton beams which form an optical barrier for lateral confinement. The reason is that the ion irradiation acts to increase the density of Frenkel defects in silicon. Owing to this effect, the resistivity of the damage regions becomes higher, thus the rate of porous silicon formation is reduced in that irradiated regions during subsequent anodization. Anodization with a periodic high/low current density creates a multilayer of porous silicon. The current density is related to the refractive index and the thickness of porous silicon is determined by the etching time shown in the schematic of Bragg cladding waveguides

(Fig.7.1)**.** The results are presented in chapter 4.3.3 for the etching rate and the refractive index respectively.

Simulation by the transfer matrix method was carried out for the reflectivity from Bragg reflectors at a wavelength of 1550 nm for the sake of optimizing the waveguide structure. The quarter-wave condition is modified for glancing angle incidence since the wave transmits in the waveguide core approaching the layers at glancing angle. The optimum values occurs as

$d_h/(d_h + d_l) = 0.44$, (7.2.1)

where d_h and d_l are the thickness of the high and low refractive index layer [95].

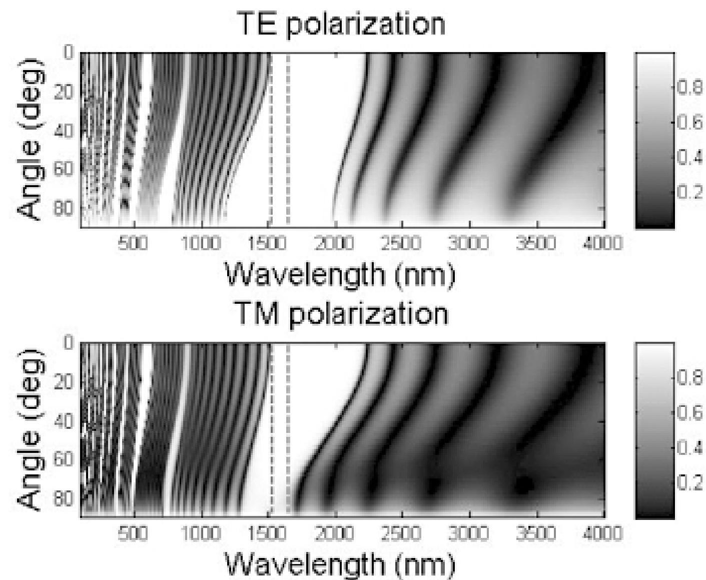

Figure 7.2. Surface plots of the simulated reflectance of the Bragg reflectors as a function of wavelength and angles, in the TE and TM polarizations.

The results are represented in Fig. 7.2 for eight bilayers with thickness of 300 nm and 200 nm, and refractive indices of 1.40 and 2.38 respectively. The broken lines indicate the range of wavelength where omnidirectional reflectivity takes place. Here, this range is about 100 nm from 1480 nm to 1680 nm including the C and L

communications band. Though it is not necessary for guiding from zero degree to 90 degree, it further enhances confinement and is correlated to the polarization independent large band gap[95].

7.3 Characterization of Bragg waveguides

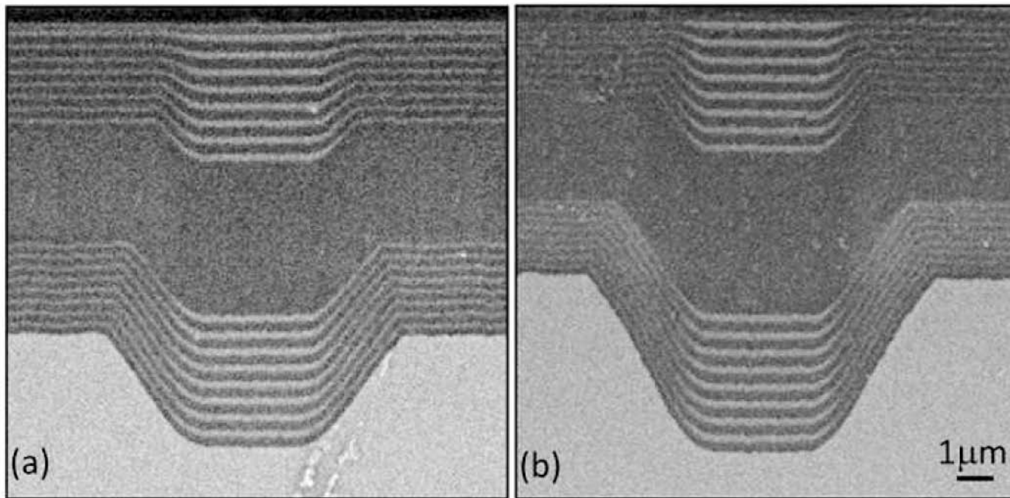

Figure 7.3. (a) and (b) shows the resultant cross sectional SEM image of Bragg cladding waveguide irradiated with a fluence of 2×10^{15}/cm2 and $4 \times 10^{15}/cm^2$.

The resultant waveguide structures include a central core layer of refractive index of 1.40 which is sandwiched by eight bilayers of alternating high and low index of 2.38 and 1.40. Cross-section SEM images of the waveguides are shown in Figure 7.3. The fabricated structures with a core width and height of 3×4 µm were irradiated with fluences of 2×10^{15} protons /cm^2 and 4×10^{15} protons/cm^2 respectively. In the SEM image (Figure 7.3), the contrasting light-color and deep-color regions show the distinct refractive index of the bilayers. The higher ion fluence produces a broader sidewall angle and a larger displacement between the two bilayers. At the intermediate layer, the centre part shrinks towards the thinner irradiated region, where

a chirping effect is produced. Owing to chirping the reflectance, band gap becomes even broader. It is essential for the light being confined in the low index core. From the damage profile of 2MeV protons, about the first 40 μm is uniform, which is important for this work to maintain a stable lower growth rate of porous silicon.

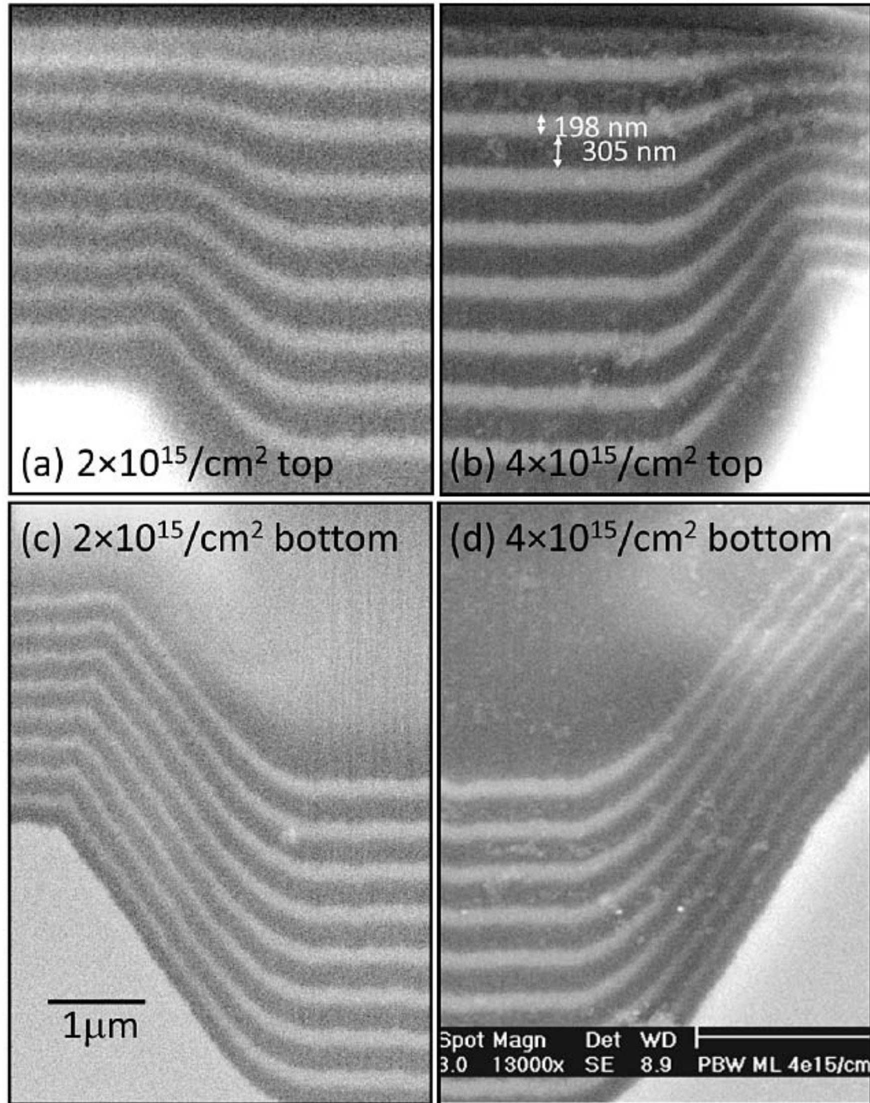

Figure 7.4. close-up SEM images of the top and bottom claddings of the waveguide sidewalls for a fluence of $2 \times 10^{15}/cm^2$ and $4 \times 10^{15}/cm^2$ respectively

Simulation was conducted for the fundamental mode field diameter and single-mode condition by the software Beamprop^{TM} in Fig. 7.6. The Finite Element Method (FEM)

was introduced to find approximate solutions for the Maxwell equations at a free space wavelength of 1550 nm based on the geometry of the waveguide structure. This software is capable of simulating the number of guided modes for an arbitrary structure with high index contrast [75]. Each grid can be subdivided into triangular segments using the non-uniform meshing feature in order to better define the index profile at the tilted edges of the sidewalls. Hence, the waveguide structure can be precisely modeled for each fluence by incorporating a compression factor and a rate of change of sidewall angle with depth as presented in Fig. 7.3 and 7.4. The cross-sectional profile of the simulated geometry of the waveguide shown in Fig. 7.6 was designed for fluences of 2×10^{15} protons/cm^2 and 4×10^{15} protons/cm^2. It can be observed from the SEM image that most of the optical power is confined in the low index core for both structures, and the fundamental TE and TM modes can be seen respectively from the distribution of the electric field components in the horizontal and vertical direction. Moreover, the cross-section area in the TE mode exhibits a larger size than the TM mode from the image, because confinement is weaker in the lateral direction. Based on the simulation of 1/e electric field width for the fundamental mode profile shown on Fig. 7.5, the area of the TE mode is slightly larger (about 0.1 μm) than the TM mode for both fluences. This means that the mode size is determined by the width when the intensity drops to 1/e of its maximum value. The sidewalls of the top and bottom layer become sharper which can close the gap from where power can leak, while increasing light confinement within the Bragg

reflectors. From figure 7.6, a significant decrease in mode size in both TE and TM polarizations can be seen while the sidewalls become sharper. Also, it is found from simulations that the mode field diameter for the higher fluence irradiation is about 1 μm smaller than the lower fluence irradiated one for a certain core width. Hence, greater confinement is expected for high fluence irradiation, which provides a practical structure for fabricating waveguides with a smaller radius of curvature.

The simulation results for varying both the width and height of the waveguide core are shown in Fig. 7.5 (b). The lines in the figure represent the boundary of the single-mode and multi-mode for the waveguide designs of 2×10^{12} protons/cm^2 and 4×10^{15} protons/cm^2 respectively. The dimension of the waveguide determines whether the waveguide is either single-mode or multi-mode. The area below the lines shows single-mode size in both polarizations. At the area beyond the lines, the waveguide is multi-mode. We can find that single-mode guiding can be supported by a large core of several microns in width and height. The boundary is found to vary further upwards for lower fluence. The reason is that higher fluence irradiation induces sharper sidewalls which provide better light confinement for higher order modes, and a smaller core size demanded for single-mode waveguide designs. As the height is larger than 7 μm, the TE polarization cannot guide in such waveguide structure for the waveguides fabricated by 2×10^{15} protons/cm^2 based on our experiments. Thus, this waveguide behaves like a planar waveguide and there is no lateral light confinement in such situation.

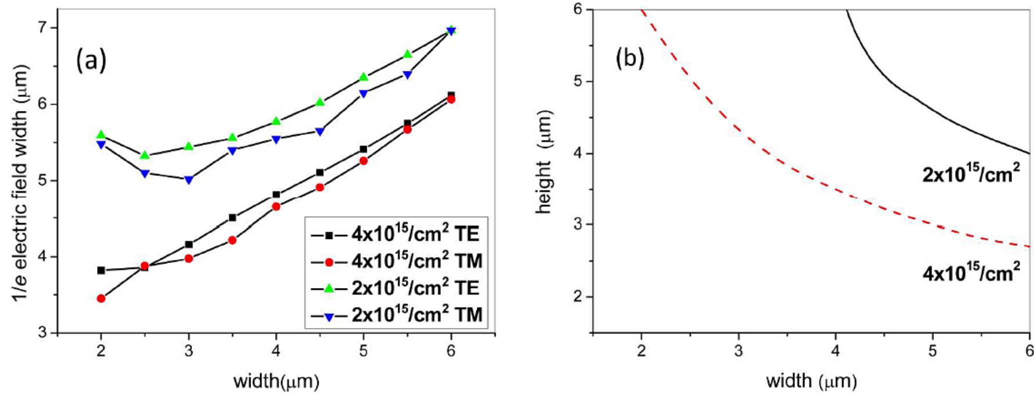

Figure 7.5. (a) Plot of 1/*e* electric field width as a function of width in TE and TM polarizations. (b) Theoretical single-mode boundary as the width and height of the core is varied.

Propagation losses were characterized by the scattered light technique [98]. A broadband laser source of 30 mW C+L and 1525-1625 nm was coupled into the waveguide using a 60× objective. The TE and TM polarization can be shifted by a cube polarizing beamsplitter and half waveplate. The scattered light was recorded by a microscope coupled a highly sensitive Peltier-cooled InGaAs camera (Xeva-FPA-1.7-320), located on the top of the waveguide. Uncertainty in the propagation loss is determined from statistical fluctuations of five independent waveguide measurements. Two different waveguides satisfied the single-mode regimes as discussed before, since there is a core width and height of 3 × 4 μm for both waveguides. For a fluence of 2×10^{15} protons/cm^2, the loss is 0.9 ±0.1 dB/cm and 0.7 ±0.1 dB/cm for the TE and TM polarizations, respectively. The scattered light for TE polarization shows a higher brightness and broader width compared to the TM polarization. The propagation loss increases to 2.8 ± 0.1 dB/cm and 2.5 ± 0.1 dB/cm for the TE and TM polarizations as the fluence increases to 4×10^{15} protons/cm^2. The higher loss is in good agreement with simulations shown in Fig. 7.6. Although the

higher fluence irradiation sample exhibits sharper sidewalls to provide better lateral confinement, the modes suffer from more interaction with the side walls and light leakage through the thinner bilayers.

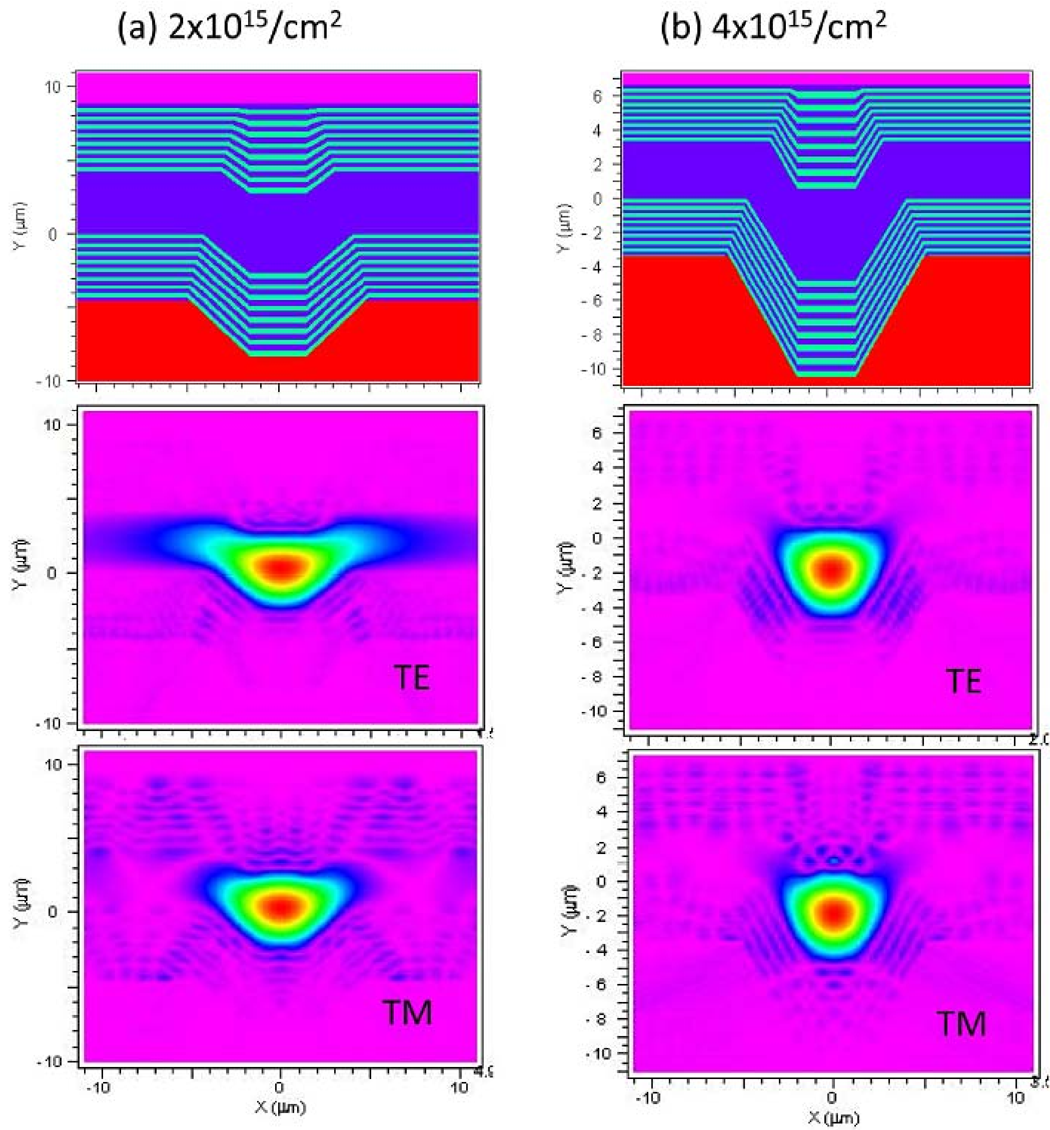

Figure .7.6. (a) and (b) simulated structure and their corresponding fundamental TE and TM modes for 2×10^{15} and $4 \times 10^{15}/cm^2$.

Generally, the propagation loss is an important measure of the quality of waveguides. Thus, reduction of the propagation loss is critical for further study. The origin of the loss consists of absorption, surface scattering, and volume scattering. For instance,

free carrier absorption mainly contributes to propagation loss for p+ anodized waveguides. However, the absorption in p+ microporous silicon is much less than mesoporous silicon owing to surface trapping [99]. Hence increasing the porosity can diminish the number of free carriers and reduces the absorption of the nanocrystallites in the core layer. Sidewall roughness is induced by proton beam fluctuations during the direct irradiation process and mechanical vibration of the stage also contribute to propagation loss. This fluctuation from proton beam writing can be reduced by scanning the sample for more loops. Moreover, the waveguide design can be improved by increasing the core size and number of bilayers, which can enhance the light confinement and eventually reduce the loss.

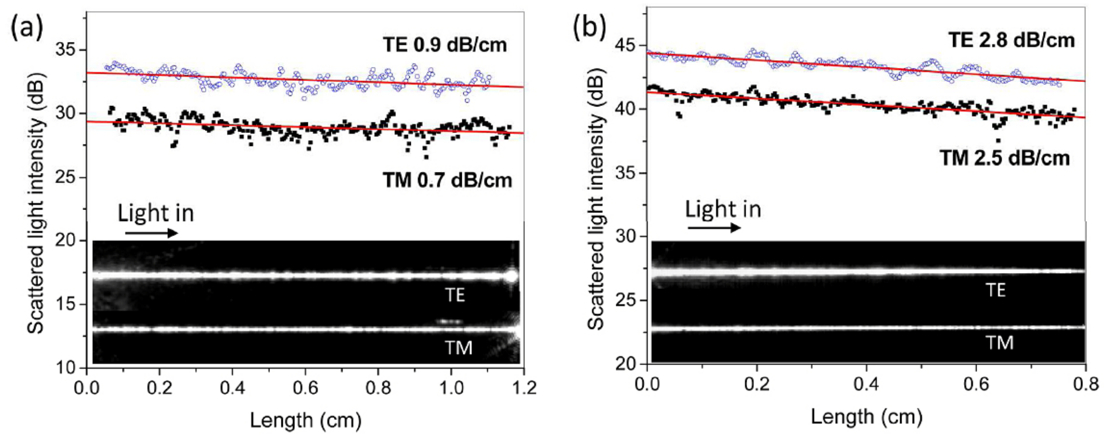

Figure 7.7. shows the scattered light intensity as a function of length for (a) $2 \times 10^{15}/cm^2$ and (b) $4 \times 10^{15}/cm^2$ determined from the scattered light images in the inset.

7.4 Summary

In this chapter, single-mode Bragg cladding rib waveguides have been successfully fabricated using proton beam irradiation. Avoiding the traditional multiple deposition process steps, we proposed a monolithic integration of Bragg waveguides in silicon.

As a result, our waveguides showed low loss of 1-3 dB/cm in both the TE and TM polarizations over a broad wavelength range of 1525-1625 nm. Based on this type of Bragg waveguides with porous silicon layers, the properties of porous silicon allows them to use for sensing applications

Chapter 8

Conclusion

8.1 Summary of Results

This thesis work has developed novel schemes to fabricate different silicon based waveguides with superior optical properties. This project has been beneficial academically both to the author and to the field of silicon photonics. The results obtained from the study of waveguides in silicon and porous silicon platform have produced several publications. It has also been an interesting project from the evolution of the fundamental concepts necessary to design the device, to the experimental considerations for properly investigating the characteristics of the fabricated devices. The aim of this chapter is to discuss the key findings of this research and the conclusions that may be drawn from them.

To achieve two and three dimensional control of silicon waveguide fabrication, the technique and capability of micro machining silicon/PSi using ion irradiation together with PSi formation is presented in this thesis. The main benefit of this machining technique is the ability to selectively form PSi in the lateral and vertical sense by locally introducing defects with irradiation. The steps involved are simple and direct:

1. Irradiation of the silicon wafers

2. Electrochemical anodization of the irradiated wafers

3. Removal of PSi (or not) by KOH or electro polishing

High-index-contrast silicon-on-oxidized-porous silicon (SOPS) strip waveguides were fabricated with direct proton beam writing. Three lines were irradiated with fluences of 7×10^{13}, 1×10^{14}, and $1 \times 10^{15}/cm^2$ on a 0.5 Ω.cm *p*-type silicon wafer with a focused beam of protons to prevent porous silicon formation during the subsequent anodization process. The final waveguide structure consists of a silicon core that is optically isolated by the oxidized porous silicon cladding and the refractive index contrast and structure profile of the SOPS waveguide is similar to a conventional silicon-on-insulator (SOI) waveguide. Advantages of this SOPS waveguide over conventional SOI ones include their direct fabrication in silicon rather than in SOI wafers, fewer complex processing steps and the compatibility of this fabrication process with full isolation by oxidized porous silicon. In particular, the propagation loss for the waveguide irradiated with a fluence of $1 \times 10^{15}/cm^2$ was measured to be approximately 1 dB/cm for both the TE and TM polarizations. This is to our knowledge the lowest reported loss for SOPS waveguides so far.

In addition, the large area irradiation facility was successfully constructed based on direct proton beam writing and was applied to many of the studies presented here. To demonstrate the possibility to upscale the production of the above described SOPS waveguides, uniform large ion beams were used to irradiate silicon wafers coated with pre-patterned photo-resist masks. The advantages of using the large area beam

irradiation compared with using direct proton beam irradiation include the rapid mass production of these SOPS waveguides and at the same time the elimination of any surface roughness caused by the direct writing approach. In this way, many waveguides may be simultaneously irradiated. After the two-step anodization and oxidation process, arrays of SOPS waveguides are simultaneously formed. The effect of oxidation on the propagation loss and surface roughness of SOPS waveguides fabricated by such method has been demonstrated. Significant loss reduction from about 10 dB/cm to 1 dB/cm has been obtained in the TE and TM polarizations after oxidation smoothening of both the bottom and the sidewalls about 20 nm. This corresponds well to simulations using the beam propagation method that show significant contributions from both surfaces and bottoms. Based on large irradiation, we have fabricated strip waveguides with varied dimensions and further study has provided results to show the relationship of the propagation loss and the dimension of the waveguide. In addition, further study has revealed the relationship between the surface roughness and propagation loss. From the results, it is found that the validity of the theoretical analysis of scattering loss is proved by experiments. In this thesis, the function of scattering loss α is illustrated for rectangular waveguides derived from planar waveguides, which is important for evaluation of the loss of waveguide fabrication and helpful to improve the transmitting property of waveguides in future work. Another type of SOPS waveguides which have been created in this method is waveguide bends. This is the first study of C-bend waveguide to reveal the bend loss

over a wide range of bending radii. The loss decreased when the bending radius increase as expected and the lowest loss yielded values of 1.28 and 1.64 dB/bend in the TE and TM mode for 80 μm bend radius. 90 degree bending waveguides with a great variety of practical application are produced. The minimum bend loss occurs as the bending radius is equal or greater than 125 μm which is about 1.3 dB/bend. Here, our waveguide bends possess a rectangular-like cross-section, thus they are polarization independent.

Another scheme to fabricate silicon waveguide has been explored in this thesis, using porous silicon to fabricate omnidirectional waveguides on to a silicon chip. Unlike the SOPS waveguides described above, light is confined in omnidirectional waveguides by a photonic band gap instead of total internal reflection. This allows for light to be guided in a core region that has a lower refractive index than the surrounding cladding material. The resultant structure of omnidirectional waveguide consists of porous silicon layers with a low index core of 1.4 that is bounded by eight bilayers of alternating high and low refractive index of 1.4 and 2.4. Here, ion irradiation acts to reduce the thickness of porous silicon formed, creating an optical barrier needed for lateral confinement. Single mode guiding with losses as low as approximately 1 dB/cm were obtained for both the TE and TM polarization over a broad range of wavelengths from 1525 nm to 1625 nm. Such an approach offers a method for monolithic integration of Bragg waveguides in silicon, without the need for sophisticated processes of depositing alternating materials.

8.2 Recommendations for further work

Notwithstanding the positive results obtained in this work, there are many aspects of the research that should still be investigated.

- We have demonstrated an ability of irradiating millimeter length waveguide, which can be used to irradiate perpendicular line by simply focusing the beam in horizontal direction. Grids can be produced by this technique.
- Based on the experimental results indicated in chapter 5, the propagation loss of SOPS waveguide is not as low as conventional SOI bending waveguides since the interface scattering is stronger in SOPS bending waveguides; therefore, further study should attempt to reduce the roughness of waveguide to lower the scattering loss.
- A direct extension of the work for Bragg cladding waveguides is to couple the large area irradiation with porous silicon formation to produce a complex structure of an omnidirectional waveguide such as 90 degree bending waveguides.
- In order to fabricate a true practical 3D waveguide, 90 degree waveguides can be produced in our further work which can cross perpendicularly at different height.

Bibliography

1. Soref, R.A. and J.P. Lorenzo, *All-silicon active and passive guided-wave components for =1.3 and 1.6 m.* IEEE Journal of Quantum Electronics, 1986. **QE-22**(6): p. 873-9.
2. Soref, R.A., D.L. McDaniel, Jr., and B.R. Bennett, *Guided-wave intensity modulators using amplitude-and-phase perturbations.* Journal of Lightwave Technology, 1988. **6**(3): p. 437-44.
3. Soref, R.A., J. Schmidtchen, and K. Petermann, *Large single-mode rib waveguides in GeSi-Si and Si-on-SiO2.* IEEE Journal of Quantum Electronics, 1991. **27**(8): p. 1971-4.
4. Reed, G.T., W.R. Headley, and C.E.J. Png. *Silicon photonics - The early years*. in *Optoelectronic Integration on Silicon II, January 25, 2005 - January 26, 2005*. 2005. San Jose, CA, United states: SPIE.
5. Reed, G.T. and A.P. Knights, *Silicon Photonics: An Introduction.* John Willey & Sons, Inc. , 2004.
6. Kurdi, B.N. and D.G. Hall, *Optical waveguides in oxygen-implanted buried-oxide silicon-on-insulator structures.* Optics Letters, 1988. **13**(2): p. 175-7.
7. Cortesi, E., F. Namavar, and R.A. Soref. *Novel silicon-on-insulator structures for silicon waveguides*. in *IEEE SOS/SOI Technology Conference 1989, October 3, 1989 - October 5, 1989*. 1989. Stateline, NV, USA: Publ by IEEE.
8. Davies, D.E., et al. *Optical waveguides and SIMOX characterisation*. in *1989 IEEE SOS/SOI Technology Conference (Cat. No.89CH2796-1), 3-5 Oct. 1989*. 1989. New York, NY, USA: IEEE.
9. Schmidtchen, J., et al. *Low loss integrated-optical rib-waveguides in SOI*. in *1991 IEEE International SOI Conference Proceedings (Cat. No.91CH3053-6), 1-3 Oct. 1991*. 1991. New York, NY, USA: IEEE.
10. Rickman, A., et al., *Low-loss planar optical waveguides fabricated in SIMOX material.* IEEE Photonics Technology Letters, 1992. **4**(6): p. 633-5.
11. Rickman, A.G., G.T. Reed, and F. Namavar, *Silicon-on-insulator optical rib waveguide loss and mode characteristics.* Journal of Lightwave Technology, 1994. **12**(10): p. 1771-6.
12. Weiss, B.L., et al., *Optical waveguides in SIMOX structures.* IEEE Photonics Technology Letters, 1991. **3**(1): p. 19-21.
13. Petermann, K., *Properties of optical rib-guides with large cross-section.* Archiv fur Elektronik und Uebertragungstechnik, 1976. **30**(3): p. 139-40.

14. Paniccia, M., V. Krutul, and S. Koehl, *Intel's Research in Silicon Photonics Could Bring High-Speed Optical Communication to Silicon.* Advanced Silicon Photonics White Paper, 2004 February: p. 1-5.
15. Uhlir, A., Jr., *Electrolytic shaping of germanium and silicon.* Bell System Technical Journal, 1956. **35**(2): p. 333-347.
16. Canham, L.T., *ROOM TEMPERATURE PHOTOLUMINESCENCE FROM ETCHED SILICON SURFACES: THE EFFECTS OF CHEMICAL PRETREATMENTS AND GASEOUS AMBIENTS.* Journal of Physics and Chemistry of Solids, 1986. **47**(4): p. 363-373.
17. Partridge, S.L., *Silicon-on-insulator technology.* Solid-State and Electron Devices, IEE Proceedings I, 1986. **133**(3): p. 66-76.
18. Canham, L.T., *Silicon quantum wire array fabrication by electrochemical and chemical dissolution of wafers.* Applied Physics Letters, 1990. **57**(10): p. 1046-1048.
19. Cullis, A.G. and L.T. Canham, *Visible light emission due to quantum size effects in highly porous crystalline silicon.* Nature, 1991. **353**(6342): p. 335-8.
20. Calcott, P.D.J., et al., *Identification of radiative transitions in highly porous silicon.* Journal of Physics: Condensed Matter, 1993. **5**(7): p. 91-8.
21. Halimaoui, A., et al., *Electroluminescence in the visible range during anodic oxidation of porous silicon films.* Applied Physics Letters, 1991. **59**(3): p. 304-6.
22. Pavesi, L., *Porous silicon: a route towards a Si based photonics?* Microelectronics Journal, 1996. **27**(4-5): p. 437-48.
23. Bell, T.E., et al., *Porous silicon as a sacrificial material.* Journal of Micromechanics and Microengineering, 1996. **6**(4): p. 361-9.
24. Navarro, N., et al. *Electrochemical etching of porous silicon sacrificial layers for micromachining applications*. in *Seventh Workshop on Micromachining, Micromechanics and Microsystems in Europe, MME '96, 21-22 Oct. 1996*. 1997. UK: IOP Publishing.
25. Stewart, M.P. and J.M. Buriak, *Chemical and biological applications of porous silicon technology.* Advanced Materials, 2000. **12**(12): p. 859-69.
26. Benilov, A., et al., *Porous silicon localization for implementation in matrix biosensors.* Materials Science & Engineering B (Solid-State Materials for Advanced Technology), 2007. **139**(2-3): p. 221-5.
27. Rendina, I., et al., *Porous silicon-based optical biosensors and biochips.* Physica E, 2007. **38**(1-2): p. 188-92.
28. Arrand, H.F., et al., *The application of porous silicon to optical waveguiding technology.* IEEE Journal of Selected Topics in Quantum Electronics, 1998. **4**(6): p. 975-82.
29. Stefano Ossicini, L.P., Francesco Priolo, *Light Emitting Silicon for Microphotonics.* Springer, 2003. **Chapter 3**.

30. Lehmann, V. and U. Gosele, *Porous silicon formation: A quantum wire effect.* Applied Physics Letters, 1991. **58**(8): p. 856-8.
31. Lehmann, V., *The electrochemistry of silicon : instrumentation, science, materials and applications / Volker Lehmann.* Willey-VCH, 2002.
32. Watt, F., et al., *Proton beam writing.* Materials Today, 2007. **10**(6): p. 20-29.
33. van Kan, J.A., et al., *New resists for proton beam writing.* Nuclear Inst. and Methods in Physics Research, B, 2007. **260**(1): p. 460-3.
34. Van Kan, J.A., et al., *Proton beam writing: A tool for high-aspect ratio mask production.* Microsystem Technologies, 2007. **13**(5-6): p. 431-434.
35. van Kan, J.A., et al., *High aspect ratio PDMS replication through proton beam fabricated Ni masters.* Nuclear Inst. and Methods in Physics Research, B, 2007. **260**(1): p. 353-6.
36. Shao, P.G., et al., *Poly (dimethyl siloxane) micro/nanostructure replication using proton beam written masters.* Nuclear Instruments and Methods in Physics Research Section B: Beam Interactions with Materials and Atoms, 2007. **260**(1): p. 479-82.
37. Shao, P.G., et al., *Rapid prototyping of micro/nano poly (methyl methacrylate) fluidic systems using proton beam writing.* Nuclear Inst. and Methods in Physics Research, B, 2007. **260**(1): p. 362-5.
38. Sum, T.C., et al. *Proton beam writing of passive waveguides in PMMA*. in *8th International Conference on Nuclear Microprobe Technology, September 8, 2002 - September 13, 2002*. 2003. Takasaki, Japan: Elsevier.
39. Yue, W., et al., *The fabrication of x-ray masks using proton beam writing.* Journal of Micromechanics and Microengineering, 2008. **18**(8).
40. Hovington, P., D. Drouin, and R. Gauvin, *CASINO: a new Monte Carlo code in C language for electron beam interaction. I. Description of the program.* Scanning, 1997. **19**(1): p. 1-14.
41. Ziegler, J.F. *SRIM-2003*. in *Proceedings of the Sixteenth International Conference on Ion, June 29, 2003 - July 4, 2003*. 2004. Albuquerque, NM., United states: Elsevier.
42. Bettiol, A.A., et al. *A LabVIEWTM-based scanning and control system for proton beam micromachining*. in *7th International Conference on Nuclear Microprobe Technology and Applications, 10-15 Sept. 2000*. 2001. Netherlands: Elsevier.
43. Bettiol, A.A., et al. *Ionscan: Scanning and control software for proton beam writing*. in *Nuclear Microprobe Technology and Applications Proceedings of the 9th International Conference on Nuclear Microprobe Technology and ICNMTA 2004, September 13, 2004 - September 17, 2004*. 2005: Elsevier.
44. Mangaiyarkarasi, D., M.B.H. Breese, and Y.S. Ow, *Fabrication of three dimensional porous silicon distributed Bragg reflectors.* Applied Physics Letters, 2008. **93**(Copyright 2009, The Institution of Engineering and Technology): p. 221905 (3 pp.).

45. Smith, F.G., T.A. King, and D. Wilkins, *Optics and photonics: an introduction.* Wiley, 2007.
46. Jalali, B. and S. Fathpour, *Silicon photonics.* Journal of Lightwave Technology, 2006. **24**(12): p. 4600-4615.
47. Marcuse, D., *Theory of dielectric optical waveguides.* ACADEMIC PRESS, INC 1991.
48. Mool C. Gupta, J.B., *The Handbook of Photonics.* CRC Press, 2007. **14**: p. 2-4.
49. *Agilent Technologies, Inc., 395 Page Mill Rd. Palo Alto, CA 94306, USA.* www.agilent.com.
50. *Thorlabs, Inc., 435 Route 206 North, Newton, NJ 07860, USA.* www.thorlabs.com.
51. Tittelbach, G., B. Richter, and W. Karthe, *Comparison of three transmission methods for integrated optical waveguide propagation loss measurement.* Pure and Applied Optics, 1993. **2**(6): p. 683-700.
52. Rao, S.V., et al., *Measurements of optical loss in GaAs/Al2O3 nonlinear waveguides in the infrared using femtosecond scattering technique.* Optics Communications, 2002. **213**(4-6): p. 223-8.
53. Okamura, Y., S. Yoshinaka, and S. Yamamoto, *Measuring mode propagation losses of integrated optical waveguides: a simple method.* Applied Optics, 1983. **22**(23): p. 3892-4.
54. Okamura, Y., S. Sato, and S. Yamamoto, *Simple method of measuring propagation properties of integrated optical waveguides: an improvement.* Applied Optics, 1985. **24**(1): p. 57-60.
55. Lerondel, G., R. Romestain, and S. Barret, *Roughness of the porous silicon dissolution interface.* Journal of Applied Physics, 1997. **81**(9): p. 6171-6171.
56. Mazzoleni, C. and L. Pavesi, *Application to optical components of dielectric porous silicon multilayers.* Applied Physics Letters, 1995. **67**(20): p. 2983-5.
57. Ow, Y.S., *MICROMACHINING OF SILICON VIA ION IRRADIATION WITH POROUS SILICON FORMATION.* Thesis, 2010.
58. Unagami, T. and M. Seki, *Structure of porous silicon layer and heat-treatment effect.* Journal of the Electrochemical Society, 1978. **125**(8): p. 1339-44.
59. Lai, L. and E.A. Irene, *Limiting Si/SiO2 interface roughness resulting from thermal oxidation.* Journal of Applied Physics, 1999. **86**(3): p. 1729-35.
60. Lee, K.K., et al., *Fabrication of ultralow-loss Si/SiO2 waveguides by roughness reduction.* Optics Letters, 2001. **26**(23): p. 1888-90.
61. Buehler, *Saturn Building, 101 Lockhurst Lane, Coventry, CV6 5SF, UK.* www.buehler.co.uk.
62. Grime, G.W. and F. Watt, *BEAM OPTICS OF QUADRUPOLE PROBE-FORMING SYSTEMS*. 1984.
63. Watt, F., et al. *The National University of Singapore high energy ion nano-probe facility: Performance tests*. in *8th International Conference on*

Nuclear Microprobe Technology, September 8, 2002 - September 13, 2002. 2003. Takasaki, Japan: Elsevier.

64. M.B.H. Breese, D.N.J., P.J.C. King,, *Materials Analysis Using a Nuclear Microprobe,*. Wiley, New York, 1996.
65. Jamieson, D.N. and G.J.F. Legge, *Aberrations of single magnetic quadrupole lenses.* Nuclear Instruments and Methods in Physics Research Section B: Beam Interactions with Materials and Atoms, 1987. **29**(3): p. 544-556.
66. Jamieson, D.N. and G.J.F. Legge, *The measurement and correction of spherical aberration in a magnetic quadrupole quadruplet lens system.* Nuclear Instruments and Methods in Physics Research Section B: Beam Interactions with Materials and Atoms, 1988. **34**(3): p. 411-422.
67. Breese, M.B.H., D.N. Jamieson, and J.A. Cookson, *Measurement and correction of parasitic sextupole components in magnetic quadrupole lenses.* Nuclear Instruments and Methods in Physics Research Section B: Beam Interactions with Materials and Atoms, 1990. **47**(4): p. 443-452.
68. Astrova, E.V. and V.A. Tolmachev, *Effective refractive index and composition of oxidized porous silicon films.* Materials Science and Engineering B: Solid-State Materials for Advanced Technology, 2000. **69**: p. 142-148.
69. Suzuki, S., et al., *High-density integrated planar lightwave circuits using SiO2-GeO2 waveguides with a high refractive index difference.* Journal of Lightwave Technology, 1994. **12**(5): p. 790-6.
70. Payne, F.P. and J.P.R. Lacey, *A theoretical analysis of scattering loss from planar optical waveguides.* Optical and Quantum Electronics, 1994. **26**(10): p. 977-86.
71. Lee, K.K., et al., *Effect of size and roughness on light transmission in a Si/SiO2 waveguide: Experiments and model.* Applied Physics Letters, 2000. **77**(11): p. 1617-19.
72. Loni, A., et al., *Porous silicon multilayer optical waveguides.* Thin Solid Films, 1996. **276**(1-2): p. 143-146.
73. Takahashi, M. and N. Koshida, *Fabrication and characteristics of three-dimensionally buried porous silicon optical waveguides.* Journal of Applied Physics, 1999. **86**(9): p. 5274-8.
74. Tien, P.K., *Light Waves in Thin Films and Integrated Optics.* Appl. Opt., 1971. **10**(11): p. 2395-2413.
75. *BeamPROP by RSoft.* www.rsoftdesign.com.
76. Marcuse, D., *Mode conversion caused by surface imperfections of a dielectric slab waveguide.* Bell System Technical Journal, 1969. **48**(10): p. 3187-215.
77. Lacey, J.P.R. and F.P. Payne, *Radiation loss from planar waveguides with random wall imperfections.* IEE Proceedings J (Optoelectronics), 1990. **137**(4): p. 282-8.
78. Wiener, N., *Generalized harmonic analysis.* Acta Mathematica, 1930. **55**(1): p. 117-258.

79. Ladouceur, F., J.D. Love, and T.J. Senden, *Measurement of surface roughness in buried channel waveguides.* Electronics Letters, 1992. **28**(14): p. 1321-2.
80. Marcatili, E.A.J., *Dielectric rectangular waveguide and directional coupler for integrated optics.* Bell System Technical Journal, 1969. **48**(7): p. 2071-102.
81. Haus., H.A., *Waves and fields in optoelectronics* Englewood Cliffs, 1984.
82. Headley, W.R., *Optical Ring Resonators in Silicon-On-Insulator.* Thesis, 2005.
83. Marcatili, E.A.J. and S.E. Miller, *Improved Relations Describing Directional Control in Electromagnetic Wave Guidance.* Bell System Technical Journal, 1969. **48**(7): p. 2161-2188.
84. Marcatili, E.A.J., *Bends in optical dielectric guides.* Bell System Technical Journal, 1969. **48**(7): p. 2103-32.
85. Vlasov, Y.A. and S.J. McNab, *Losses in single-mode silicon-on-insulator strip waveguides and bends.* Optics Express, 2004. **12**(8).
86. Siong, D.R.L.C., *Device integration for silicon microphotonics platforms.* PhD Thesis, MIT, 2000.
87. Origin, http://www.originlab.com/.
88. Yeh, P. and A. Yariv, *Bragg reflection waveguides.* Optics Communications, 1976. **19**(3): p. 427-430.
89. Cho, A.Y., A. Yariv, and P. Yeh, *Observation of confined propagation in Bragg waveguides.* Applied Physics Letters, 1977. **30**(Copyright 1977, IEE): p. 471-2.
90. Yeh, P., A. Yariv, and E. Marom, *Theory of Bragg fiber.* J. Opt. Soc. Am., 1978. **68**(9): p. 1196-1201.
91. Fink, Y., et al., *A Dielectric Omnidirectional Reflector.* Science, 1998. **282**(5394): p. 1679-1682.
92. Winn, J.N., et al., *Omnidirectional reflection from a one-dimensional photonic crystal.* Opt. Lett., 1998. **23**(20): p. 1573-1575.
93. Ibanescu, M., et al., *An All-Dielectric Coaxial Waveguide.* Science, 2000. **289**(5478): p. 415-419.
94. Yi, Y., et al., *On-chip Si-based Bragg cladding waveguide with high index contrast bilayers.* Opt. Express, 2004. **12**(20): p. 4775-4780.
95. Xifr-Prez, E., et al., *Porous silicon omnidirectional mirrors and distributed Bragg reflectors for planar waveguide applications.* Journal of Applied Physics, 2007. **102**(Compendex).
96. Hecht, E., *Optics.* Reading, Mass. : Addison-Wesley Pub. Co., 2nd ed, 2002: p. 426-430.
97. Pavesi, L. and P. Dubos, *Random porous silicon multilayers: application to distributed Bragg reflectors and interferential Fabry-Perot filters.* Semiconductor Science and Technology, 1997. **12**(5): p. 570-575.

98. Pirasteh, P., et al., *Optical loss study of porous silicon and oxidized porous silicon planar waveguides.* Journal of Applied Physics, 2007. **101**(8): p. 83110-1.
99. Lehmann, V., et al. *Resistivity of porous silicon: a surface effect*. in *Porous Silicon and Related Materials. Symposium F at the E-MRS Spring Conference 1994, 24-27 May 1994*. 1995. Switzerland.